MICROPILLARS FOR FRICTION MODULATION AT TISSUE-DEVICE INTERFACES

by

LEAH K. BOWEN

B.S., Northwestern University, 2013

M.S., Northwestern University, 2015

A thesis submitted to the

Faculty of the Graduate School of the

University of Colorado in partial fulfillment

of the requirement for the degree of

Doctor of Philosophy

Department of Mechanical Engineering

2021

Committee Members:

Mark Rentschler, Chair

Rong Long

Stephen Edmundowicz

Maureen Lynch

Kurt Maute

Bowen, Leah K. (Ph.D., Mechanical Engineering)

Micropillars for Friction Modulation at Tissue-Device Interfaces

Thesis directed by Professor Mark E. Rentschler

Micropillars, microscale surface textures, can substantially influence friction properties of material interfaces. Soft micropillars have utility in compliant applications like medical devices, wearables, or robotic locomotion. However, little is known about the friction properties of or mechanisms behind soft micropillars contacting soft tissue or tissue-like substrates. In this thesis, I focus on this type of soft-on-soft micropillar friction. Chapter 1 reviews micropillars morphologies that modify the contact properties of adhesion and friction, mechanistic studies of contact, and micropillar applications. In Chapters 2-4, I outline three aims, beginning each with a more in-depth introduction. In Chapter 2, I add micropillars to enteroscopy balloons, determining that balloons textured with micropillars have superior anchoring performance on tissue compared to smooth balloons. In Chapter 3, I investigate the underlying friction mechanics behind the balloon's soft, stretchable micropillars. I experimentally determine coefficients of friction between strained soft micropillars and a soft substrate using a custom traction measurement platform in wet and dry environments. I develop finite element models to describe this behavior, finding that micropillar spacing, shape, and contact area contribute to friction. In Chapter 4, I investigate friction of asymmetric textures. I fabricate slanted micropillars. I experimentally determine texture stiffness and lubrication affects magnitude and direction of differential friction. I develop finite element models that indicate the feature-substrate interface changes as features change stiffness. Overall, in this work I expand the field of micropillar mechanics and translational research on related medical devices. This will provide a framework for

additional research into understanding how micropillars achieve their remarkable properties and how to tune interfaces for optimized contact.

DEDICATION

First and foremost, I dedicate this thesis to the micropillars and their innumerable, small sacrifices.

This thesis is also dedicated to my little sister, Anna Bowen. I appreciate her consistent rant availability and when we get to spend time together. She has become a role model for three things: how to treat everyone like a person, how to be a repository for fine cooking tips, and how to thrash around in the forest for hours, get nowhere in particular, and come out with a good attitude.

ACKNOWLEDGEMENTS

I acknowledge Dr. Rentschler for being a supportive mentor for the past few years. Dr. Rentschler has created a positive lab environment with many learning and sharing opportunities. Through Dr. Rentschler's mentoring I have become a better scientist and engineer. It also bears mentioning that Dr. Rentschler has recently advised me on top sharks, and he grills very good pizza.

I would also like to thank my coadvisor, Dr. Long for being enthusiastic about my work and providing insightful feedback. Every time I have met with Dr. Long, I feel better about the state of my research. With Dr. Long's guidance I have been able to tackle many research problems I would not be able to otherwise.

I would like to thank Dr. Edmundowicz for both the time he has been on my committee and as a preceptor. I have enjoyed and appreciate his scientific and clinical mentorship. As I see more patients in the coming months, I will especially use what I have learned from Dr. Edmundowicz in my bedside manner and connecting with patients.

I also acknowledge Dr. Lynch and Dr. Maute for asking me insightful questions and giving helpful feedback on both my comprehensive exam and defense committees.

This thesis is built on the work done by former doctoral students in the Advanced Medical Technologies Laboratory, Dr. Madie Kern and Dr. Levin Sliker. Dr. Kern has previously studied micropillar adhesion mechanics experimentally and with finite element simulations. Dr. Sliker made the first version of the Automated Traction Measurement Platform and has also done work on micropillars for robotic wheels.

I would also like to thank the Pillar Pals for looking at my analysis, critiquing my figures, reading my paper drafts, listening to my presentations. Specifically, Kristin for her

extremely detailed feedback. Kristin is always available to bounce ideas off of, to review material with, and she makes very good coffee. Karl, for his collaboration and coauthorship. Brodie, for answering my finite element questions. Brodie also makes very good coffee. Emily 1 (Zuetell) for her help in the thankless task of making strained micropillar samples. Other AMTL members, particularly Vani, Brian, Mitch, Khoi, Max, Emily 2 (DiTomasso), Micah, and Greg deserve acknowledgement as well for all their help, friendship, and support.

From the MSTP, I want to thank Liz Bowen for checking in on my progress and general well-being for the time we have been in the MSTP together. I would like to acknowledge Dr. Gutierrez-Hartmann for supporting me doing what I want to. To my knowledge, I am the first (and potentially only) CU MSTP student to get their Ph.D. in mechanical engineering. Arthur was totally fine with that and it seems to have worked out, so I appreciate his confidence in me. I would also like to thank Dr. Wilson. As the new MSTP director, she personally met with every student. This year, we have met many times and she has put in considerable work to figure out how to get me back to medical school.

The continuous support from my family has been an immense privilege and I would not be here without it. I will begrudgingly admit that my parents were right about some things this whole time. My dad the Elder Dr. Bowen first mentioned MD-PhD programs to me when I was eight, suggesting I do it in some sort of quantitative field, like statistics. I said no, obviously, and the idea of an MD-PhD did not resurface again until after I graduated from college. My dad also deserves some credit for the idea of Pillarwear™, clothing with directional micropillars. He also insisted on proofreading the entire text of this thesis in one sitting.

Finally, I would like to thank my mom, Dr. Wenie Din. When I was 17, she suggested I might like engineering. I said no, that engineering was boring, and that engineers are

boring people who only crunch numbers. As I complete my third engineering degree, I can only hope that she is satisfied by the plots I've regularly sent her over the past several years and that the figures I present here meet her high standards.

CONTENTS

LIST OF TABLES

LIST OF FIGURES

CHAPTER 1

INTRODUCTION

1.1 Bioinspiration

The gecko was one of the first animals to be formally studied from a contact mechanics perspective. The Tokay gecko is famously known for its window and ceiling-climbing abilities. In fact, many animals use microscopic foot structures to more easily maneuver through their environments. These microscopic textures, micropillars, alter contact properties between the animals' feet and surfaces in their environment. The ability of micropillars to enhance animal's ability to walk on challenging surfaces is so useful that micropillars have convergently evolved several times (Figure 1). Unlike chemical adhesives, micropillars rely on mechanics and Van der Waals forces to determine contact behavior. These textures can withstand many load cycles and self-clean (Hansen and Autumn 2005), making them superior to adhesives made by humans.

The Tokay gecko's footpads have been studied most. They have a hierarchal structure. First, textures on each toe are separated into scansors, adhesive lamellae covered in setae. Setae form 2x2 grid structures. The setae themselves branch into long, thin hairlike structures with spatula-shaped tips.

Autumn and Gravish detailed the attachment and detachment mechanisms of gecko setal arrays, noting loading direction-dependent friction (shear adhesion) properties. They used these findings to explain how the gecko adheres to surfaces. For the front feet, the setae curve caudally when unloaded but then straighten out rostrally when the gecko steps down onto a surface. The gecko then pushes down into the surface and pulls back on its setae to "set" the adhesion. The gecko detaches by increasing the angle of the setae with the surface so that the setae elastically recoil. The adhesion of individual setae is suggested to occur due

to Van der Waals forces (Autumn and Gravish 2008). These mechanisms have inspired a number of synthetic micropillar mimics (Raut et al. 2018; Glick et al. 2018; Northen et al. 2008; Tamelier, Chary, and Turner 2012; Mahdavi et al. 2008; Murphy, Aksak, and Sitti 2009; Stark et al. 2016; Murphy, Kim, and Sitti 2009; Liu et al. 2021; Y. Tian et al. 2015; Y. Kim et al. 2014; Tan et al. 2019; D. J. Guo et al. 2015; J. H. J. Lee et al. 2014; Jin et al. 2014).

Spiders also have adhesive hierarchal setae on their feet, mostly around their claws. Like geckos, the flexible setae have a high aspect ratio (are long and thin). Their tips widen and flatten into spatulas. Spider micropillars exhibit similar mechanisms to other micropillars by increasing the number of contacts with a surface (Kesel, Martin, and Seidl 2004; Roscoe and Walker 1991). This contributes to contact splitting, a phenomenon where having many discrete contacts increases overall adhesion between materials because adhesion defects do not propagate (Arzt, Gorb, and Spolenak 2003).

Tree frogs utilize wet adhesion to enhance their climbing abilities. They have tightly packed hexagonal micropillar-like structures on their footpads. Each hexagonal micropillar has additional nanoscale peglike projections. Frogs secrete a mucus that coats their foot structures. This mucus creates capillary bridges between footpad and substrate, increasing adhesion (Federle et al. 2006).

Interestingly, the density of foot microstructures that small animals use for adhesion increases with body mass, up to the gecko (Arzt, Gorb, and Spolenak 2003). However, larger animals also utilize microscopic textures, though not for climbing vertical or overhanging surfaces. The animal with the most relevant foot textures is the polar bear (micropillar bear?). The footpads of the polar bear are covered in papillae. These papillae are rounded bumps. They are low aspect ratio – short and wide, compared to the high aspect ratio setae of geckos and spiders. The papillae are thought to increase the bears' friction on the icy

surfaces they travel on (Manning et al. 1985). Much of the research discussed in this thesis, particularly Chapter 3, utilizes low aspect ratio micropillars and their friction properties. These micropillars demonstrated low adhesion (Kern et al. 2017), and increased traction on soft materials ((Sliker et al. 2012)). Sharks are another larger animal that uses microtextures. Shark denticles create more efficient interactions with water (Lloyd et al. 2021). Shark skin has also demonstrated directional friction properties (Manoonpong et al. 2016). I use somewhat similar micropillars in Chapter 4.

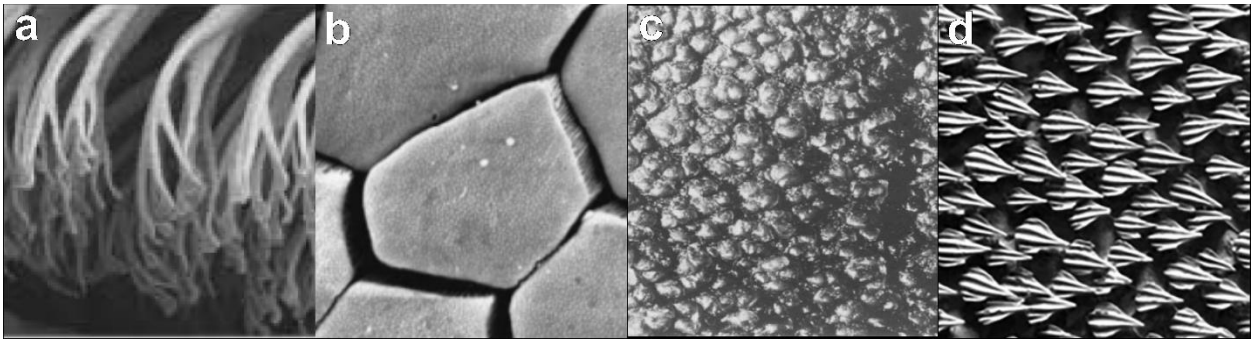

Figure 1: A wide array of naturally-occurring micropillars exist. (a) Tokay gecko (Autumn and Gravish 2008) (b) Tree frog (Federle et al. 2006) (c) Polar bear (Manning et al. 1985) (d) Shark (Ankhelyi, Wainwright, and Lauder 2018)

These naturally occurring micropillars have inspired a wide variety of synthetic micropillars as shown in Figure 2. The field of synthetic micropillars explores fabrication, applications, and mechanics of their tunable contact properties with a variety of substrates. The work in this thesis specifically focuses on friction of soft micropillars contacting soft tissue or tissue-like substrates.

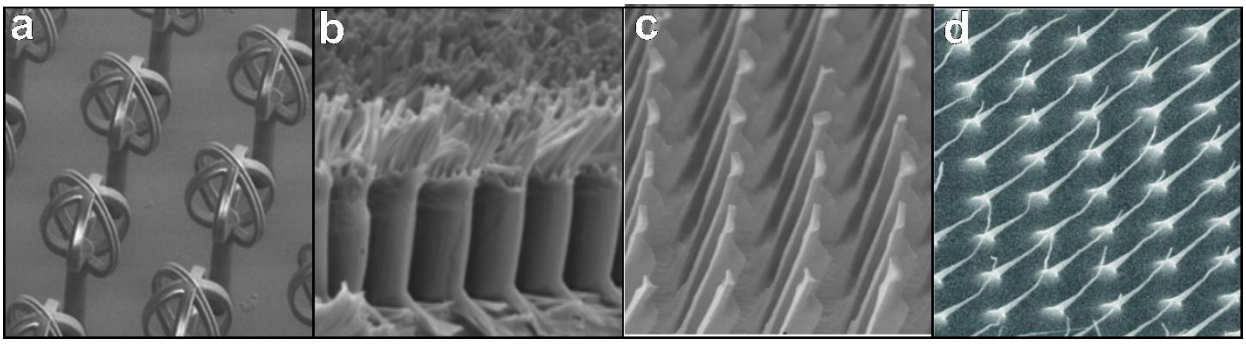

Figure 2: Many types of synthetic micropillars have been fabricated (a) Micropillars fabricated by 3D laser-lithography. These structures are similar to plant *Salvinia molesta* to promote condensation on the structures but retain a layer of air at the surface (Tricinci et al. 2015)(b) Hierarchal micropillars for enhanced adhesion on glass (Raut et al. 2018) (c) Micropillars with directional adhesion against a rigid substrate (W. Jiang et al. 2017) (d) dome-shaped micropillars used to enhance anchoring of experimental enteroscopy balloons (Bowen et al. 2020)

1.2 Micropillar Adhesion

The vast majority of micropillar contact mechanics research has focused on adhesion of small, "perfect" (i.e. good-looking), high aspect ratio polydimethylsiloxane (PDMS) arrays contacting rigid substrates. Though this work focuses on microscale, occasionally imperfect (i.e. less aesthetically pleasing), low aspect ratio micropillars contacting soft substrates, these other micropillars still merit discussion.

Many high aspect ratio, soft micropillars have high adhesion to rigid substrates. Cylindrical PDMS micropillars have shown high adhesion relative to smooth PDMS against smooth stiff silicone (Schubert et al. 2007) and glass. In contrast, low aspect ratio PDMS micropillars have lower adhesion against soft substrates compared to smooth PDMS (Kern et al. 2017). A related parametric modeling study demonstrates a few mechanisms that contribute to adhesive force against a soft substrate. At small micropillar spacings, pull-off force is minimized because only the micropillar tops contact the substrate. At large micropillar spacings and when micropillars are shorter, the indenting substrate experiences increased deformation and contact between micropillar backing layer and substrate, which may lead to increased adhesion and friction forces (Kern, Long, and Rentschler 2018).

Other shapes, such as cylindrical micropillars with wider tips (mushroom or spatula micropillars) have even higher adhesion against glass compared to cylindrical micropillars with flat tips (Drotlef et al. 2013; J. H. J. Lee et al. 2014). Other groups have worked on suction-based micropillar adhesion. Wang et al created finite element models of miniature hemispherical craters, finding that suction force increases against a flat, rigid substrate with lower surface tension and a reinforcing shell along the crater (L. Wang, Qiao, and Lu 2017). Octopus-inspired suction cups have demonstrated higher adhesion than cylindrical micropillars and flat PDMS against rigid substrates. Interestingly, these suction cups exhibit

higher wet adhesion against glass compared to dry adhesion(Thanh-Vinh et al. 2011), though most other micropillar work focuses on dry adhesion.

1.3 Micropillar Friction

Relatively less research has been performed on micropillar friction. Madji et al found high friction using high aspect ratio, relatively stiff polypropylene (up to 1GPa) micropillars on rigid substrates (Korpela, Suvanto, and Pakkanen 2012; Majidi et al. 2006). Even stiffer textured materials such as steel have been studied, but are not as relevant to this work (Muthukumar and Bobji 2018).

Soft PDMS micropillars have also demonstrated higher friction compared to flat surfaces when sheared against rigid substrates. Xue et al. sheared cylindrical, T-shaped, and asymmetric T-shaped micropillars against a ruby sphere. Friction force is largest for high aspect ratio micropillars compared to low aspect ratio micropillars and largest for T-shaped micropillars compared to cylindrical micropillars. The asymmetric micropillars also demonstrate differing friction properties when sheared in different directions (Xue et al. 2014). Raut et al. fabricated high aspect ratio hierarchal micropillars with high friction against a silicone wafer and demonstrated the ability of a robot to climb angled glass utilizing these micropillars (Raut et al. 2018).

A few papers investigate micropillar friction on soft substrates such as intestinal tissue. Sitti's group explored the effects of micropillar diameter. Low aspect ratio PDMS micropillars were coated in silicone oil and dragged across ex-vivo intestine on a weighted sled while friction force was measured. A 140μm diameter micropillar had the highest friction force compared to larger or smaller micropillars. High viscosity silicone oil also had the best performance. Tao Sun's group published a series of papers detailing cylindrical micropillar

friction against ex-vivo small intestine as well, finding micropillars increase friction and adhesion. 80μm diameter micropillars have the largest friction compared to larger and smaller diameters. They hypothesize that different micropillar geometries operate at different points on a Stribeck curve. With larger spacing, mucus can flow between micropillars, resulting in less friction than more tightly spaced micropillars (Kwon et al. 2006; Zhang et al. 2017).

1.4 Medical Devices/ Applications

Only two commercially available medical devices are textured. Roughened breast implants have lower complication rates compared to smooth implants (Randquist and Gribbe 2010). The head of hip orthoses are occasionally textured with dimples, though most are experimental (Roy et al. 2015; Ghosh et al. 2015; Ghosh and Abanteriba 2016). Thus, medical devices with micropillars to modulate their contact properties is a field with significant potential.

Cylindrical low-aspect ratio micropillars have been added to a series of experimental wheeled and treaded gastrointestinal robots. The traction performance of smooth versus patterned wheels were directly visually compared in an in-vivo gastrointestinal demonstration. A two-wheeled robot was actuated on the peritoneal surface of a CO_2-filled abdominal cavity. The smooth wheel experienced significant slip and is unable to drive the robot forwards. The patterned wheel, however, did not slip (Sliker et al. 2012). The *Endoculus* gastrointestinal exploratory robot was designed as an expansion upon this work. It utilizes low aspect ratio cylindrical micropillars on its treads for traction against the wall of the large intestine. This robot has demonstrated efficacy in navigating and traversing the length on an ex-vivo porcine large intestine (Formosa et al. 2019). For this series of related research,

micropillars have demonstrated traction in a slippery, wet, mucus-covered environment and show promise for other tissue-contacting devices. A few other endoscopy robots that utilize micropillars are discussed in the literature as well. Sitti's group created a robot with adhesive pads that utilize low aspect ratio micropillars that are either dry or coated with silicone oil. The pads with micropillars demonstrated higher adhesion relative to smooth pads in an intestinal environment (Karagozler et al. 2006).

A few other examples of medical devices that utilize micropatterns include surgical graspers and biomedical adhesives. Several low aspect ratio polygonal micropillar shapes – hexagon, diamond, triangle, and square – were patterned onto surgical graspers. Hexagonal micropillars produced superior grasping ability. Interestingly, this manuscript does not disclose the micropillar material, but can be assumed to be a typical metal grasper surface (H. Chen et al. 2015). Several groups have harnessed the enhanced adhesion properties of micropillars to design medical adhesives (W. G. Bae et al. 2013) for sensor attachment (Kwak, Jeong, and Suh 2011) and drug delivery (Tsai and Chang 2013).

1.5 Research Overview

This work focuses on applying micropillar technology to medical devices and exploring the friction mechanisms between micropillars and soft, tissue-like substrates. It is divided into three chapters. First, I test the performance of several micropillar morphologies on balloons used for double balloon enteroscopy in an ex-vivo porcine small intestine. Second, I investigate the bulk friction properties of soft, distensible micropillar arrays experimentally and with finite element models. I explore the role of strain, lubrication, and stiffness on friction between micropillars and a soft substrate. Third, I create micropillars with asymmetric friction properties. I experimentally determine the effects of micropillar stiffness

and lubrication on friction directionality. I also create finite element models to further investigate their underlying behavior. The ultimate goal of this work is twofold. First, I advance biomedical device technologies and second, I increase understanding of micropillar behavior and friction mechanisms.

CHAPTER 2

PATTERNED ENTEROSCOPY BALLOON DESIGN FACTORS INFLUENCE TISSUE ANCHORING[1]

2.1 Introduction

Balloon-assisted enteroscopy is used to diagnose and treat small intestinal diseases including ulcers, obstruction, occult bleeding, and other abnormalities. The small intestine is difficult to navigate using typical endoscopes for two reasons. First, the small intestine can only be reached endoscopically by first navigating through the colon (rectal route) or the esophagus and stomach (oral route). Second, the small intestine is approximately six meters long and often tortuous whereas a traditional endoscope is less than two meters long. In balloon enteroscopy procedures, any portion of the small intestine can be visualized by plicating and compressing the small intestine on the overtube, allowing endoscopic interventions to be performed such as dilation, stenting, hemostasis, polypectomy, biopsy, ablation, and resection (Yamamoto et al. 2014). Balloon enteroscopy allows the gastroenterologist to investigate more of the gastrointestinal tract than traditional "push" or direct enteroscopy. It is also interventional unlike capsule enteroscopy which can visualize the entire small intestine but cannot provide therapy or biopsy (Ciuti et al. 2016). Balloon enteroscopy is also is less invasive than surgical access (Yamamoto et al. 2014).

The balloon enteroscopy system includes an endoscope, balloon overtube, and pressure control unit for balloon inflation and deflation. For single balloon enteroscopy, the balloon is attached to the end of the overtube. The endoscope extends through the overtube and the two

[1] The results presented in this chapter are reported in the Journal of the Mechanical Behavior of Biomedical Materials:

Bowen LK*, Johannes K*, (*equal contributions) Zuetell E, Calahan K, Edmundowicz SA, Long R, Rentschler, M. Patterned Enteroscopy Balloon Design Factors Influence Tissue Anchoring. Journal of the Mechanical Behavior of Biomedical Materials, 2020.

slide freely against each other. After intubation, the endoscope is operatively advanced as far as possible. The balloon overtube is then advanced to this distal point and the balloon is inflated, anchoring it against the intestinal wall. The balloon overtube is then pulled backwards as the endoscope is advanced further. The endoscope tip then actuates to "hook" the tissue so that the balloon overtube can advance forward again after balloon deflation. As the balloon overtube and endoscope sequentially advance, the small intestine effectively pleats over the overtube and endoscope. Ultimately, this push-pull maneuvering of the balloon overtube interfaced with the intestine allows a two-meter long endoscope to investigate a much longer length of small intestine. For double balloon enteroscopy (DBE), one balloon attaches to the end of the overtube and the other balloon attaches directly to the endoscope near the distal camera end. The only difference in use is that in DBE the endoscope tip does not "hook" tissue, but instead the distal balloon inflates to anchor to the tissue before advancing the trailing balloon overtube (Figure 3) (Yamamoto et al. 2014; 2004; Manno et al. 2012; Gerson, Flodin, and Miyabayashi 2008).

Despite the immense benefits, balloon enteroscopy is a technically challenging procedure. One study reported an initial success rate for total endoscopic visualization of the small intestine of only eight percent for an endoscopist with 15 years of endoscopic practice (Gross and Stark 2008). Another study revealed that DBE procedures performed by experienced endoscopists had a 31% failure rate when advanced via a rectal route (Mehdizadeh et al. 2006). Additionally, both studies estimated the average procedure time for DBE to be over 90 minutes (Gross and Stark 2008; Mehdizadeh et al. 2006), compared to 20-40 minutes for a colonoscopy (Cotton et al. 2003). These lengthy and often incomplete procedures are frequently a result of slippage between the balloons used and the mucosal lining of the GI tract (Gerson et al. 2009; Teshima and May 2012; Pennazio et al. 2015). Small

intestine anatomy is a contributing factor to this difficulty. The small intestine is convoluted and has an inner layer of mucus central to the mucosa (Mahadevan 2014), making it difficult to navigate and slippery. The mucus layer is 25-54 μm in pigs (Varum et al. 2012; 2010) and is approximately 300 μm thick in the human large intestine (Gustafsson et al. 2012). During procedures, these balloon overtubes are pressure limited to prevent over-inflation of balloons. However, this limits the anchoring that can be achieved by increasing pressure. A balloon with enhanced anchoring could reduce costs and significantly improve access to care through more successful procedures and wider procedure adoption. Less balloon slippage would reduce procedure times, physician frustration, and repeat procedures, while leading to an increase in the number of completed procedures, diagnostic findings, and therapeutic success.

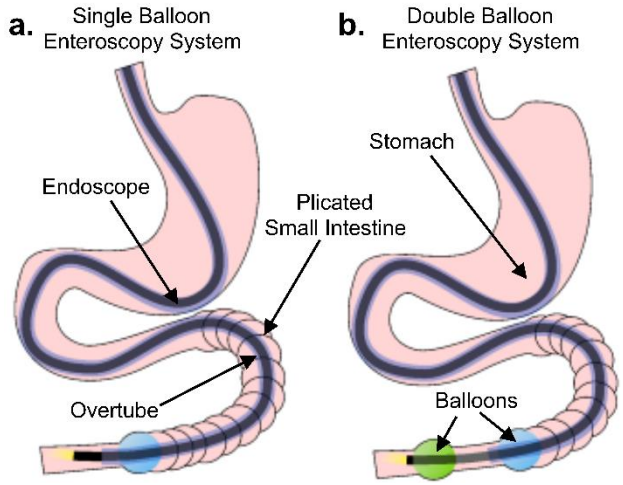

Figure 3: Overview of single and double balloon enteroscopy scope advancement techniques for diagnostic and therapeutic access into the small intestine. (a) In a single balloon endoscopy procedure, an endoscope and balloon overtube are inserted into the small intestine. The endoscope secures a section of small intestine by hooking it. Then, the overtube is moved distally, pleating the small intestine on the overtube. The balloon, attached to the overtube, is inflated, and holds the pleated small intestine on the overtube. This process is repeated, allowing advancement of the endoscope far into the small intestine and pleating the small intestine on the overtube as shown. (b) In the double balloon procedure, balloons are located on the overtube as well as endoscope tip. Compared to the single balloon procedure, the endoscope balloon secures a section of small intestine. The overtube balloon behaves in a similar manner in both procedures.

In this study, I propose that the addition of micropillars to enteroscopy balloons can improve anchoring of the tissue-balloon interface. Surface patterns have been shown to modulate contact properties, including adhesion and traction, compared to unpatterned or smooth surfaces (Del Campo, Greiner, and Arzt 2007; Xue et al. 2014; Li, Krahn, and Menon 2016). A large body of literature has shown that some types of soft patterns on relatively stiff substrates have increased adhesion relative to smooth surfaces in dry systems.

Micropillars can increase adhesion and can allow for multiple adhesion cycles during dry adhesion (Xue et al. 2014; W. G. Bae et al. 2013; Yue Wang et al. 2016). When considering a lubricated surface, such as the mucus-coated small intestine, Cheung et al. demonstrated adhesion can be enhanced by using high aspect ratio (height/radius>1), oil-coated, cylindrical patterns when in contact with an aluminum substrate (Cheung and Sitti 2008). In addition to affecting adhesion, surface patterns can also increase (Y. Kim et al. 2014) or decrease friction(He, Chen, and Wang 2008) on dry or wet (Wei et al. 2019) substrates, depending on pattern geometry. Finally, surface patterns have been applied to new technologies like robotic grippers. Soft gripper patterns such as circumferential ribs (Martinez et al. 2013) and microscopic wedges (Suresh et al. 2015) have demonstrated improved adhesion over unpatterned grippers (H. Tian et al. 2019).

However, less literature exists on the effects of patterns in contact with soft and/or wet surfaces such as the balloon-tissue interface. Assenbergh et al. showed microscale PDMS dimples have greater adhesion compared to smooth PDMS on 12 kPa polyvinyl alcohol (PVA) but not stiffer 18 kPa PVA (Peter van Assenbergh et al. 2019). McGhee et al. have discussed adhesive mechanisms of dehydrated gel adhesion to mucin. Mucin may transfer onto dehydrated gels, increasing adhesion (McGhee et al. 2019). Two studies of effects of size on cylindrical PDMS features found that a 70 μm radius increases friction relative to larger and

smaller feature radii on intestinal tissues. Kwon et al. measured friction force of micropillars against a cleaned porcine small intestine while varying normal force, lubricating silicone oil viscosity, and features size (Kwon et al. 2006). Zhang et al. measured coefficient of friction of micropillars on rabbit intestine while varying normal load and feature size. They suggest that on smooth surfaces, a continuous mucus layer forms, leading to fluid lubrication. A surface with small micropillars may not fully penetrate the mucus layer, leading to mixed lubrication. For a surface with large micropillars, features may more intimately contact the underlying mucosa, causing boundary lubrication to predominate (Zhang et al. 2016). Modeling and experiments have shown patterning surfaces with conical frustum feature decreases work of adhesion between soft substrates and PDMS features compared to smooth PDMS (Kern, Long, and Rentschler 2018). Additional modeling has demonstrated that adhesion between conical frustum features and soft tissue-like substrates decreases when feature aspect ratio increases and/or spacing decreases to reduce backing layer contact (Kern et al. 2017). Further, microscale PDMS cylindrical features have been successfully implemented as tread patterns on robotic capsule endoscopes in ex-vivo (Sliker, Kern, and Rentschler 2013) and in-vivo tissue environments (Sliker et al. 2012; 2016; Formosa et al. 2019).

Patterned medical devices is a relatively understudied field, with limited examples such as breast implants (Randquist and Gribbe 2010; Calobrace et al. 2018) and hip orthoses (Ghosh et al. 2015; Roy et al. 2015). Motivated by the technical challenges posed by balloon enteroscopy, I introduce a manufacturing method for single material and multi-material patterned enteroscopy balloons. I also investigate the influence of micropillar characteristics on the anchoring of the balloon-tissue interface.

2.2 Material and Methods

2.2.1 Balloon Fabrication

A molding process was developed that allows for varied materials and patterns (Figure 4). A 3D printed clamshell mold (Grey V4 Resin, Formlabs, Somerville, MA) creates the general structure of the balloon. A central balloon mold core inserts into the center of the clamshell to form the balloon cavity. Patterned mold inserts are created separately as a flexible strip and are inserted into the inner rim of the clamshell to pattern the balloon exterior. This process allows production of balloons with micropillars molded with the balloon, compared to other methods that adhere flat patterned sheets to existing curved surfaces (Sliker et al. 2016; Glick et al. 2018). Cylindrical patterns are referred to here with the naming convention: feature radius x feature height x feature center-to-center spacing where all units are μm. All features were arranged in a hexagonal pattern and were either soft (69 kPa) or stiff (1.93 MPa) silicone. Ecoflex-30 (Smooth-On, Inc), a platinum-cure silicone elastomer, was selected as the base balloon material due to its low modulus, high failure strain, and ease of manufacturing. Soft patterns were manufactured from Ecoflex-30. Stiff patterns were manufactured from SmoothSil-960, another higher modulus platinum-cure silicone, because it cures to Ecoflex-30. Additionally, both soft and stiff materials have been shown to be skin-safe with few effects from long-term use (W. J. Bae et al. 2015).

Patterned balloons were created using one of three methods: 1) direct 3D printing negative pattern geometry into the clamshell balloon mold, 2) reverse molding pattern inserts that were inserted into the clamshell mold (Figure 5), 3) fabrication of a positive pattern from a laser-etched Kapton mold (Potomac Photonics, Baltimore, MD), and then molding a flexible negative from PDMS that can be inserted into the clamshell mold (Figure 5a).

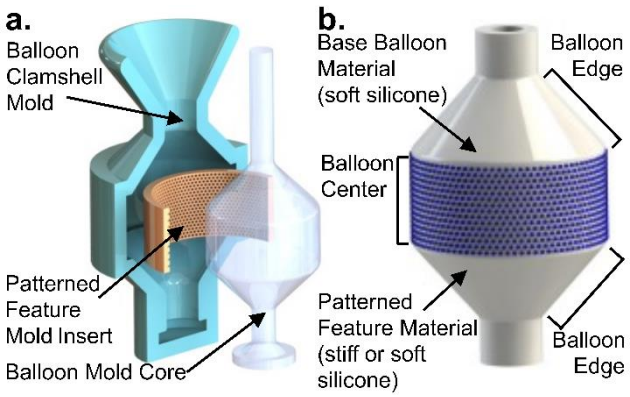

Figure 4: Balloon Manufacturing - Balloon. (a) Balloons were fabricated by adding the pattern mold insert into a clamshell mold along with a mold core. Then, uncured silicone was vacuum injected into a funnel at the top of the mold, degassed, and cured. (c) The completed balloon has a base layer of Ecoflex-30 silicone with patterns along its center of either soft (Ecoflex-30) silicone or stiff (SmoothSil-960) silicone.

To fabricate single-material Ecoflex-30 (Smooth-On, Inc., Easton, PA) balloons, the clamshell was assembled so that it contained the unfilled micropillar mold insert and balloon mold core. Next, the clamshell mold was injected with uncured Ecoflex-30 silicone and degassed under vacuum. The filled balloon mold cured at room temperature for a minimum of four hours. For the multi-material balloons, the pattern mold was separately filled with the additional material and degassed. The excess material was then scraped away, leaving the material just in the pattern. The filled pattern mold was then inserted into the clamshell mold and the balloon material was injected and cured yielding a completed balloon (Figure 5).

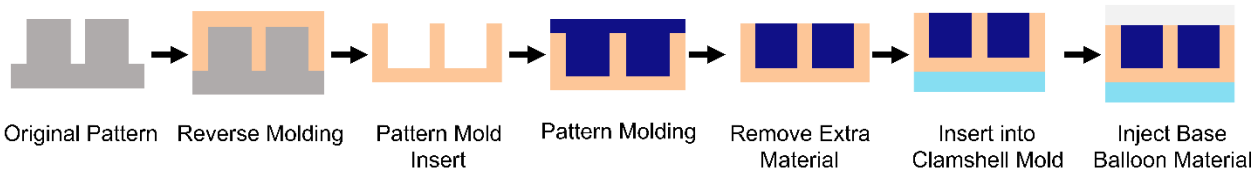

Figure 5: Balloon Manufacturing - Pattern. Several patterns were created using a reverse molding protocol so that patterns can be added to a curved surface.

2.2.2 Pattern Geometries

Twelve types of balloons with micropillars were tested (Figure 6). Conical, dome, and cylindrical micropillars are referred to using the naming convention: radius x height x center-to-center spacing in μm. Specific features are grouped into sub-studies and discussed below. The default patterning location was the center strip of the balloon as shown in Figure 6b.

Patterns tested were divided into five areas of investigation. First, micropillar size and scale was studied. Kwon et al found a peak in friction force of cylindrical low aspect ratio features at a 140 μm diameter (Cheung and Sitti 2008). Additional work has demonstrated performance of PDMS conical frustums of this diameter in modeling and as robotic wheels in an in-vivo and ex-vivo intestine environment (Sliker et al. 2012; Kern, Ortega Alcaide, and Rentschler 2014; Kern, Long, and Rentschler 2018). Therefore, 70x70x245 conical frustum features were selected for this first area of investigation. 70x70x245 conical frustum features were fabricated using Method 2. Larger 350x350x1225 dome negatives were fabricated using Method 1. Larger features were tested because I hypothesized they may be able to penetrate the mucus layer to reach the mucosa and achieve better anchoring compared to smaller features that may remain embedded within the slippery mucus. Both soft and stiff 70x70x245 conical frustums and 350x350x1225 domes were investigated in one animal as a sub-study. The results of the first sub-study informed micropillars tested for subsequent sub-studies. Second, the role of feature location was also investigated in three balloon types using stiff 350x350x1225 domes: the center strip (standard for other patterns), conical sides of the balloon (edge), and balloon center + edge. These patterned textures were fabricated using Method 1. Third, an additional sub-study investigated height and spacing of stiff cylindrical features: 350x700x1225, 350x350x2450, 350x700x1225, and 350x700x2450. These micropillars were fabricated with Method 3. Fourth, additional uncategorized features were

tested including soft circumferential 350x350x1225 ribs fabricated using Method 1 and stiff 350x350x1225 cones fabricated using Method 2. Smooth silicone balloons fabricated using Method 3 with a smooth PDMS pattern mold insert. These were used as a control for all studies and are referred to here as smooth silicone (PDMS-molded) or smooth silicone in a control context. Commercially available smooth latex balloons used for endoscopies were investigated as well. Because they were made from a different material, these were not used as a control so that the effects of balloon micropillars could be isolated.

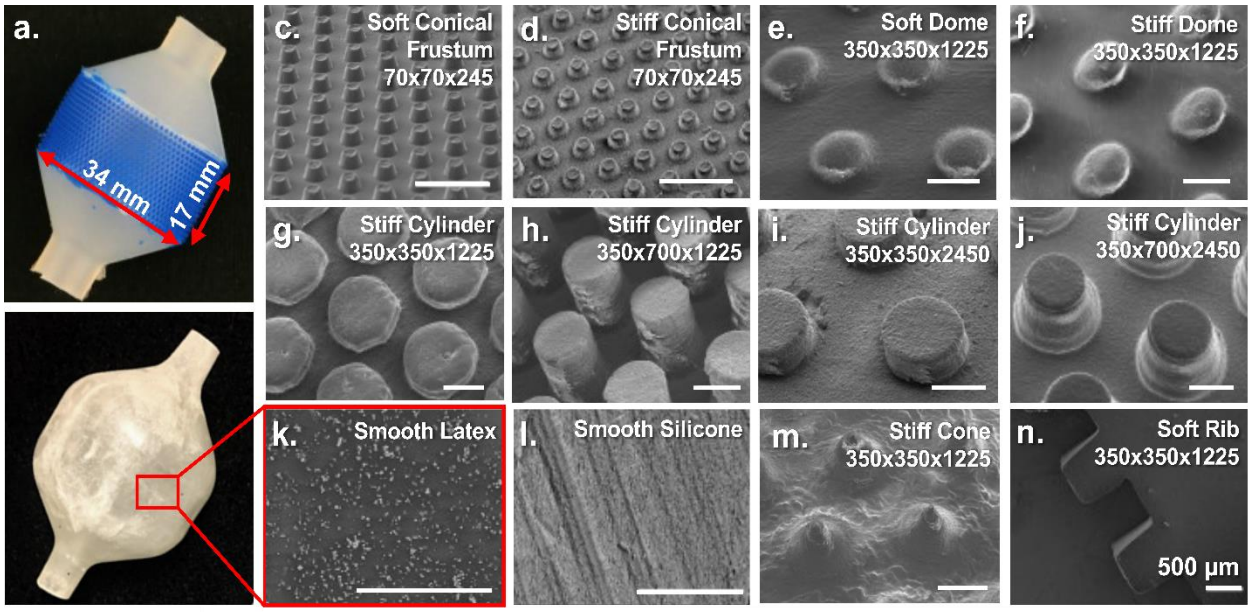

Figure 6: Balloon patterns. (a) Representative balloon molded with micropillars on the cylindrical center strip. (b) Smooth latex balloon used for balloon enteroscopy with the same dimensions as the molded balloons. Balloons in a passive uninflated state shown in part a and b, can be deflated further by pulling a vacuum. (c-n) Scanning electron microscope images of each micropillar tested on the molded balloons. Scale bars represent 500 µm. Micropillars have the naming convention: feature radius x feature height x feature center-to-center spacing in µm.

2.3.4 Ex-Vivo Tissue Testing

Balloons were evaluated in a porcine ex-vivo small intestine, an experimental platform that resembles the balloon's actual use. The goal of ex-vivo testing was to evaluate peak force, the maximum force it takes to dislodge an inflated balloon from a small intestine, between different patterned balloons. Peak force is suggestive of the force it takes a balloon to slip against the intestine in a clinical setting. A larger peak force is considered a more effective balloon.

To evaluate anchoring force of patterned balloons, a custom measurement system was built to hold a section of porcine intestine, inflate an inserted balloon, and pull it out while measuring force, displacement, and balloon pressure (Figure 7). Balloons were placed on a rigid acrylic tube to represent the endoscope or overtube. This tube contained a hosing piece that allowed for inflation, set to 6.5 kPa with a pressure regulator (NAR2000, SMC) and attachment to the force sensor. This pressure is similar to the maximum balloon pressure used in clinical balloon enteroscopy. A pressure sensor (MPXV6115 VC6U, NXP USA) recorded pressure inside the balloon during tests. A motor driver (2x7a Roboclaw, BasicMicro) controlled a motor (12V DC brushed motor, Pololu) attached to a reel and fishing line to pull the balloon at constant velocity and recorded displacement. A tensile force sensor (LCM100, Futek) was placed in line with the direction of balloon pull. Data were acquired with a Data Acquisition Device (MyDAQ, National Instruments) using a custom MATLAB script.

All animal procedures were performed in compliance with the appropriate Institutional Animal Care and Use Committee (facility accreditation number: 00235). Ex-vivo samples were obtained from animals used for other studies at the facility, reducing the need to sacrifice additional animals. Each animal was placed on a gelatin diet two days before

tissues were harvested, all data were collected within twelve hours of animal sacrifice, and harvested intestine was stored in phosphate buffered saline prior to testing. For each balloon tested, an approximately 30-cm segment of excised porcine small intestine was attached to the testing clamp. The balloon was inserted into the open end of the intestine sample and inflated with air to 6.5 kPa. The balloon was pulled out of the intestine sample at constant speed while force and air pressure are measured. Each individual balloon was tested ten times using one intestine sample. The intestine sample was changed between balloons. In total, tissue from six animals was used. Due to procedure length, all study procedures could not be completed in one sitting, necessitating the need for multiple animals. Two control balloons of smooth silicone were tested on each animal (n = 12) and two balloons of each pattern were tested except for soft 350x350x1225 (n = 4), stiff 350x350x1225 (n = 8), and smooth latex (n = 3).

To address variability between animals, tissue samples were not taken from any specific location along the small intestine and measured peak forces were normalized by the performance of smooth silicone balloons for each animal studied. Tissue directionality was not considered, but to the authors' knowledge no literature exists on directional contact properties of the small intestine. Smooth silicone balloons consistently demonstrated a lower peak force than all patterned balloons across all animals tested, providing a level of confidence for these assumptions.

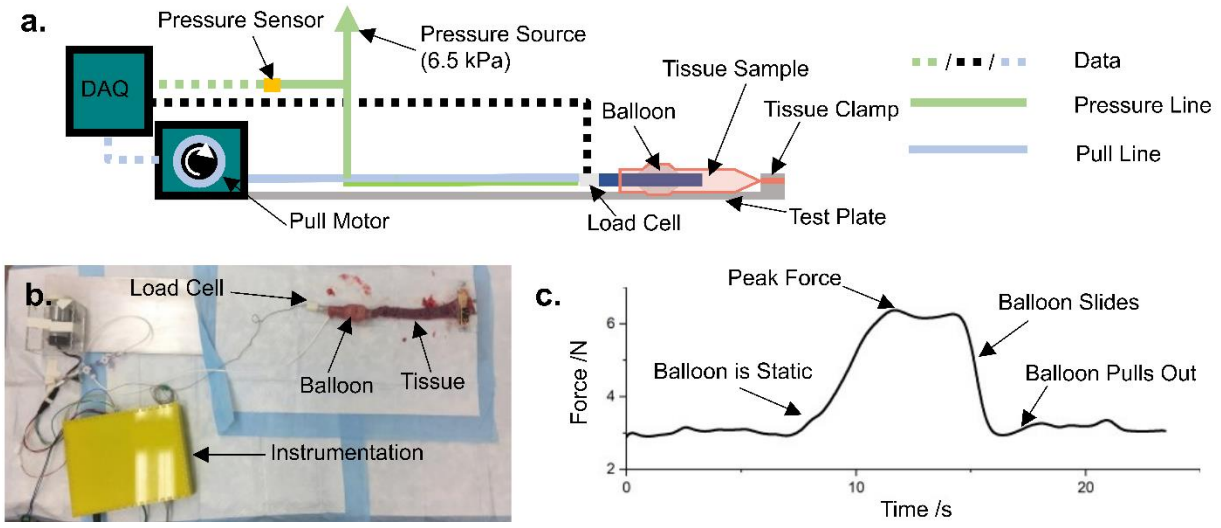

Figure 7: Ex-vivo testing. (a) Ex-vivo balloon testing device schematic. A balloon is inserted into a tissue sample clamped to a test plate. Then, the balloon is inflated from the pressure source. As the pull motor turns, the DAQ collects data from the pressure sensor and load cell. Data are recorded on a laptop computer with MATLAB. (b) Image of experimental ex-vivo balloon testing setup. (c) Representative force vs. time curve of a balloon pull test. Force is low when the motor starts turning and the balloon is static. Force rapidly increases as the motor continues turning. Peak force occurs when the balloon begins sliding. After a force plateau, force rapidly decreases as the balloon slides along the intestine. When the balloon pulls out, force returns to baseline.

2.3.5 Data Processing

Force data were smoothed using cubic splines and a smoothing parameter of 0.8. Peak force was the maximum force value of smoothed data (Figure 7c). A normalization constant for each animal was created by averaging peak forces from smooth silicone balloons. All trials were divided by this constant for each animal. Normalized values were then pooled between balloons of the same pattern type. A one-way ANOVA compared peak force between balloon groups with $\alpha = 0.01$. Non-normalized values are discussed in *2.4.8 Non-Normalized Data*.

2.3 Results

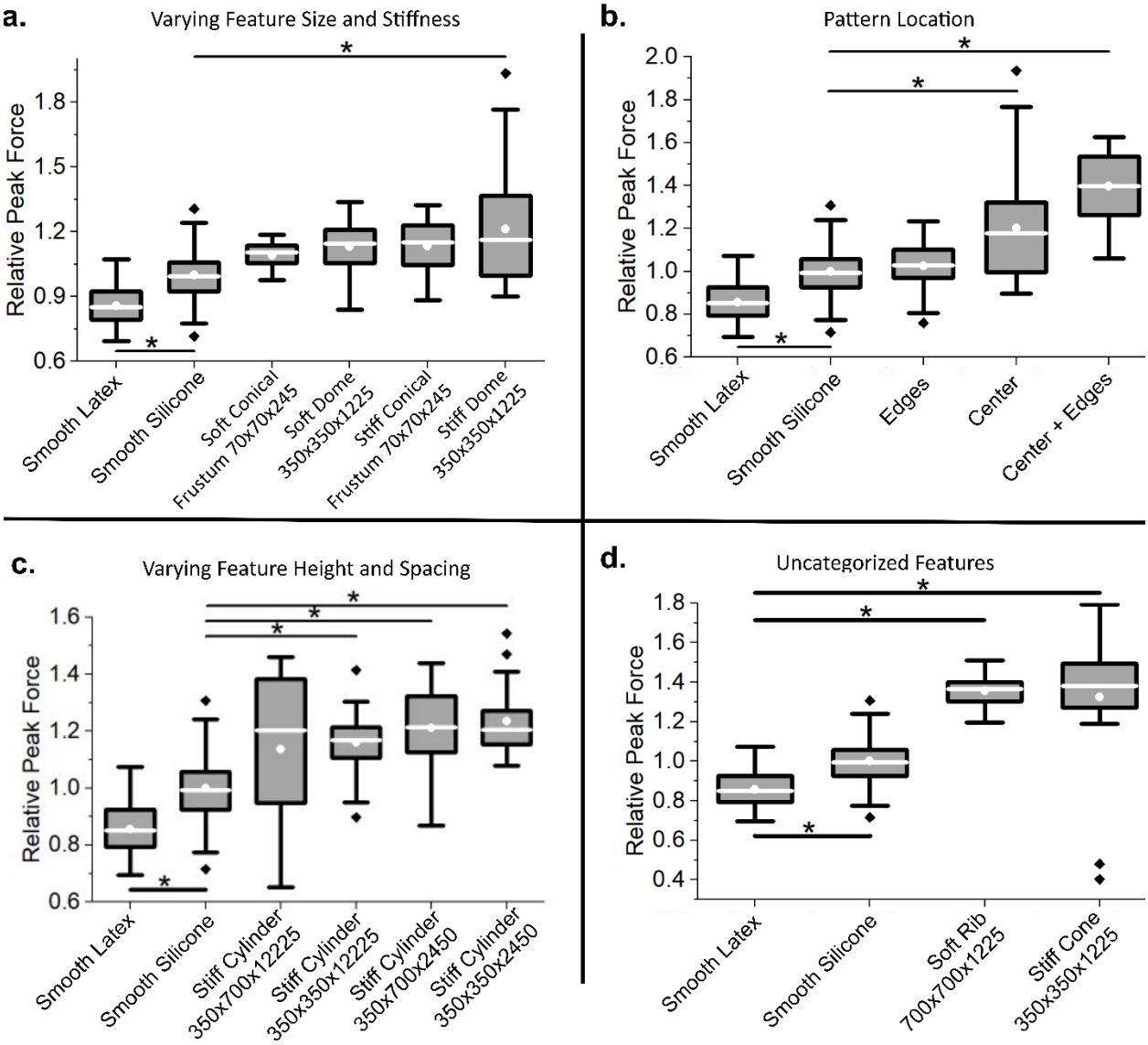

Figure 8: Results categorized by balloon type. Box and whisker plots show experimental results where the box represents the 25-75 percentile interval and whiskers show 1.5 standard deviations. The median is the near center line of the box and mean is the center white point. Outliers are black diamonds and significant differences ($p < 0.01$) are represented by black asterisks. (a) Stiff 350x350x1225 domes, stiff 70x70x245 conical frustums, and soft 350x350x1225 domes have significantly larger peak force than smooth silicone balloons. Soft 70x70x245 conical frustums do not have significantly higher peak force compared to smooth silicone balloons. (b) Center and center + edge balloons have significantly higher peak force than smooth silicone. Balloons with patterned edges do not have significantly different peak force than smooth silicone balloons. (c) All cylindrical features have similar peak force, including increased height, increased spacing, and increased height and spacing. These features all have significantly larger peak force than smooth silicone. (d) Ribs and conical features have significantly larger peak force compared to smooth silicone.

2.3.1 Varying Feature Scale and Stiffness

The soft and stiff silicone materials were compared in two feature types: smaller conical frustums (soft and stiff 70x70x245 conical frustums) and larger domes (soft and stiff 350x350x1225 domes). Of note, both geometries are approximately cylindrical, but differ due to manufacturing methods. Only stiff 350x350x1225 domes have significantly higher peak force compared to smooth silicone ($p = 7.00$ e-7). Both stiff features exhibit a higher peak force than their soft counterparts for both 70x70x245 conical frustums and 350x350x1225 domes, but this difference is not significant (Figure 8a).

These results differ from Kwon et al. and Zhang et al. who found a 70 μm feature diameter maximized friction. However, the features used in these two studies used different aspect ratios, slightly different but still cylindrical feature shapes, materials, and tissues. In this study, stiff features may penetrate better through the mucus layer of the small intestine (approximately 54 μm thick) (Randquist and Gribbe 2010) and bend less under shear loading, allowing for increased friction with the intestinal wall leading to a larger anchoring force. It is also reasonable that larger features may interface with villi of the small intestine (about 1 mm in length). Additionally, as suggested by Zhang et al., smaller features may embed in the mucus layer and experience hydrodynamic lubrication while mucus may only cover portions of larger features, resulting in boundary lubrication (Zhang et al. 2016).

2.3.2 Varying Pattern Location of Stiff Dome Features

Most patterns were located on the center strip of the balloon (center) due to ease of manufacturing, but patterning only the conical balloon edges (edges) or the entire balloon (both the center strip and conical edges: center + edges) with stiff 350x350x1225 domes was investigated to elucidate effects of pattern location on anchoring force. Patterns that cover the entire balloon are more effective than patterns that only cover the balloon center or edges. The balloons with the largest patterned surface area, center + edge, have the highest overall peak force of any balloon ($p = 7.00e-7$ compared to smooth silicone). Center + edge balloon peak force is significantly higher than the other two locations: edge ($p = 7.00e-7$) and center/350x350x1225 ($p = 4.85e-4$). Additionally, patterns on the center strip of the balloon contribute more to peak force than those on the angled edges of the balloons. Center/350x350x1225 patterns have significantly higher peak force than edge patterns ($p = 7.07e-04$) as shown in Figure 8b.

Stiff 350x350x1225 domes demonstrate an increased peak force when they cover the entire balloon surface. Adding more total features likely leads to more contact at the pattern-tissue interface and a soft, deformable material like mucus-covered tissue may conform to the features, generating a larger peak force. However, pattern location on balloons is also important. Balloons with patterned edges have a similar peak force to smooth silicone balloons and a smaller peak force compared to balloons with patterned centers. Patterning the center strip of the balloon significantly increases peak force. This is likely due to the fact that the balloon's central region engages with tissue first during inflation and likely imposes the largest amount of pressure against the tissue wall when compared to other balloon regions.

2.3.5 Varying Height and Spacing of Cylindrical Features

Aspect ratio and spacing have been previously shown to affect micropillar contact properties and were investigated in this sub-study (Kwon et al. 2006; Zhang et al. 2016; Kern, Long, and Rentschler 2018; Y. Tian et al. 2015). These features include stiff 350x350x1225 cylinder, widely spaced 350x350x2450 cylinder, high aspect ratio 350x700x1225 cylinders, and high aspect ratio and widely spaced 350x700x2450 cylinders. All cylindrical micropillars have statistically similar peak force, including taller or more widely spaced micropillars. Stiff 350x350x1225 cylinders, stiff 350x350x2450 cylinders and stiff 350x700x2450 cylinders have significantly higher peak force than smooth silicone balloons ($p = 6.41e\text{-}6$, 4.83e-6, and 8.09e-7, respectively) as shown in Figure 8c.

The two 350x350x1225 features, domes, and cylinders, have similar peak forces, suggesting that the sharp edge of these larger features may not be important to balloon anchoring. The finding that all cylindrical features have similar peak force suggests that the aspect ratios and spacing in this sub-study are not critical to balloon performance. It is possible that taller features contribute to peak force up to a certain height, after which increased height does not alter micropillar interaction with small intestinal mucus. Increased feature spacing can potentially increase contact with the backing layer between features, leading to increased adhesion (Kern et al. 2017). However, feature concentration per unit area decreases, potentially leading to similar true contact area and similar anchoring force in these cylindrical features.

2.3.6 Uncategorized Features

Additional features were studied that did not fit into any specific category. Soft rib features were investigated due to their relative ease of manufacturing. Stiff cones were

investigated as an additional feature shape. Both soft rib and stiff cone features have significantly higher peak force compared to smooth silicone ($p = 7.00e-7$, $p = 7.00e-7$, respectively) as shown in Figure 8d and have some of the largest peak forces overall compared to smooth silicone. For a continuous ring, such as the soft rib, material may only flow over the tops of features as compared to discrete micropillars where material may both flow over the tops of features and in between them. This could result in increased anchoring force for soft rib features. In addition, the point of the cones may create a large local stress that penetrates the mucus layer, increasing mucosal contact and increasing anchoring force.

2.3.7 Overall Results

Table 1 Textured Balloon Anchoring Force Results

Micropillar Type	Category	Performance Relative to Smooth Latex	p-value
Smooth Latex	Smooth	Very Poor	0.00764
Edges	Pattern Location	Poor	0.999
Soft Conical Frustum 70x70x245	Varying Size and Stiffness	Poor	0.624
Stiff Conical Frustum 70x70x245	Varying Size and Stiffness	Poor	0.0505
Stiff Cylinder 350x700x1225	Cylindrical Features Varying Size and Spacing	Poor	0.0375
Soft Dome 350x350x1225	Varying Size and Stiffness	Poor	0.0119
Stiff Dome 350x350x1225	Varying Size and Stiffness, Pattern Location	Medium	7.00 e-7
Stiff Cylinder 350x350x1225	Cylindrical Features Varying Size and Spacing	Medium	6.41 e-6
Stiff Cylinder 350x350x2450	Cylindrical Features Varying Size and Spacing	Medium	7.83 e-6
Stiff Cylinder 350x700x2450	Cylindrical Features Size and Spacing	Medium	8.09 e-7
Center + Edges	Pattern Location	High	7.00 e-7
Cone 350x350x1225	Uncategorized	High	7.00 e-7

Performance is categorized as follows: Very Poor – significantly lower peak force compared to smooth silicone, Poor – peak force not significantly different from smooth silicone, Medium – significantly higher peak force compared to smooth silicone and mean peak force < 1.3 times that of smooth silicone, High – significantly higher peak force compared to smooth silicone and mean peak force ≥ 1.3 times that of smooth silicone. α is set to 0.01.

In a combined analysis of sub-studies described above, all silicone balloons, apart from balloons with micropillars only on the edges, have significantly higher peak force compared to smooth latex, including smooth silicone balloons (Table 1). Unpatterned balloons are further compared in *2.4.9 Smooth Balloons*. Seven patterned balloon types have significantly higher peak force compared to smooth silicone including soft rib, stiff center + edge, stiff cone, stiff 350x350x2450 cylinder, stiff 350x700x2450 cylinder, stiff 350x350x1225 cylinder, and stiff 350x350x1225 dome. Five balloon types do not have significantly higher peak force than soft silicone: soft 70x70x245 conical frustum, stiff 70x70x245 conical frustum, soft 350x350x1225, stiff 350x700x1225 cylinder, and edges. The overall best balloon types from the limited design space explored are center + edge stiff 350x350x1225 domes, soft ribs, and stiff cones (Figure 9).

Uninflated balloons have significantly lower peak force compared to inflated balloons, indicating that balloon advancement and retraction will be minimally affected by balloons with increased anchoring force (*2.4.10 Uninflated Balloons*). Uninflated and inflated micropillar morphologies differ and are further discussed in *2.4.11 Effects of Inflation on Patterned Feature Morphology*. With balloon inflation, soft and stiff 70x70x245 conical frustums become more widely spaced from each other due to backing layer stretch. Soft micropillar geometry deforms more than stiff micropillars (Figure 13). Other stretched micropillars were not imaged, due to difficult sample preparation. However, it can be extrapolated that other micropillars exhibit similar geometry changes with stretch. Due to the combined effects of fabrication and deformation during balloon inflation, not all conceivable micropillars can ultimately be used in an inflated state. For example, a lower limit exists on how closely features can be spaced apart due to balloon inflation stretch, though the fabrication techniques outlined in this work allow for production of a wide range

of micropillars.

Additionally, the differing manufacturing methods and material properties of the latex versus silicone balloons may account for some differences in performance. For example, the walls of manufactured silicone balloons are thicker than those of the latex balloons though the outer dimensions are similar. Thus, smooth silicone balloons were considered the control and compared to patterned balloons. With these results, it appears clear that the addition of micropillars significantly contributes to anchoring force.

In all tests, including clinically available smooth latex balloons, visible tissue damage was observed where the tissue became duskier in color. It is unknown if these changes resemble those that occur in an in-vivo enteroscopy procedure where the small intestine has a viable blood supply. Histology should be performed during future in-vivo testing of balloons. In-vivo histology will likely give a better indication of damage compared to ex-vivo tissues undergoing degenerative changes independent of balloon damage. The presence of gross changes in all tissues during ex-vivo tests indicates patterned balloons do not cause greater damage than smooth latex balloons. Additionally, no trend in peak force was observed over the life of a tissue sample (*2.4.11 Balloon Cleaning and Performance over Multiple Trials)*, demonstrating that using the balloons multiple times does not significantly affect peak force (Figure 14).

The ex-vivo study protocol is a first approximation to the balloon enteroscopy procedure and therefore limited in several ways. The in-vivo small intestinal contents, tissue viability, hydration, mucus, and blood supply likely change upon excision. Tissue was used within several hours of animal sacrifice and kept in a phosphate buffered saline to reduce these changes. In addition, supporting structures such as the mesentery are absent in an excised small intestine. This may change anchoring force because the tissue may be less

distensible and because the in-vivo small intestine geometry is convoluted compared to straight ex-vivo segments. However, the differences found in balloon performance may translate to in-vivo evaluation. A balloon that anchors better in a straight, more deformable section of intestine will also likely anchor better in a curved, less distensible section. Future in-vivo studies should be performed to evaluate balloons in a more clinical setting.

Our study of the pattern design space finds several important factors that contribute to peak force. Stiff silicone features result in a larger peak force than features made from softer silicone. Larger features such as ribs, and 350x350x1225 cylinders, cones, and domes also demonstrate an increased peak force. Patterning the entire balloon also shows an increase in peak force. Location of micropillars are important as well. For example, the center strip of the balloons contributes more than the edges of the balloons to peak force. Finally, features with continuous rings like the ribs or features with areas of stress concentration like cones have increased peak force relative to smooth balloons. By patterning balloons with discrete features, I have created a balloon with significantly greater anchoring force in the small intestine compared to smooth balloons and over 1.6 times the anchoring force of standard smooth latex enteroscopy balloons.

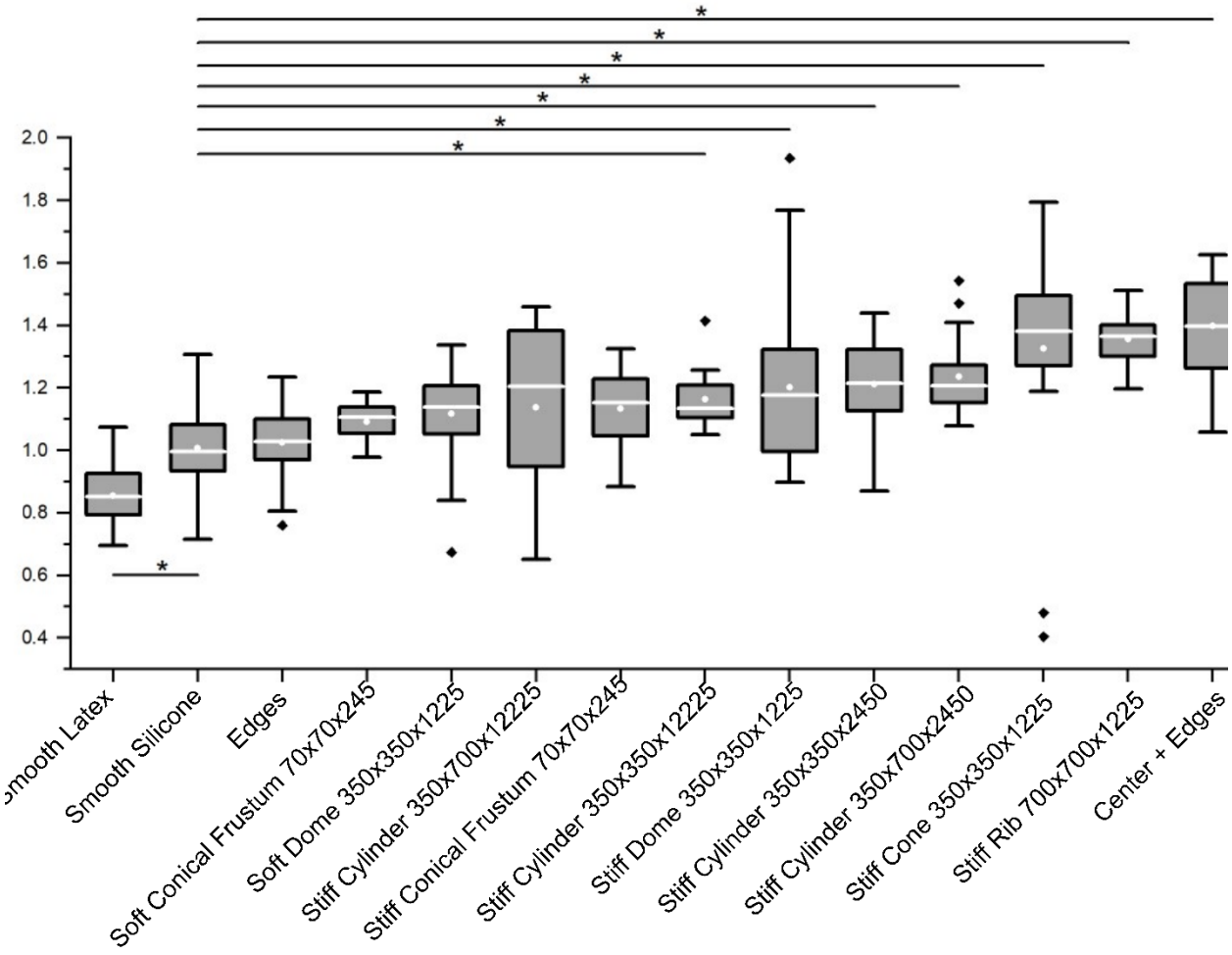

Figure 9: Normalized peak force of patterned balloons. Both smooth latex and smooth silicone balloons have significantly lower peak force than patterned balloons. Larger, stiffer, more conical patterns that cover a greater portion of the balloon's surface tend to have greater peak force.

2.3.8 Non-Normalized Data

Data shown in absolute peak force (Newtons) has a much larger variation than data normalized to smooth silicone balloons tested on each animal (Figure 10). A one-way ANOVA comparing absolute peak force between smooth silicone balloons shows significant differences between animals ($p = 3.325E-48$). Normalization lowers the spread of peak force values and allows for more accurate comparison of balloon performance.

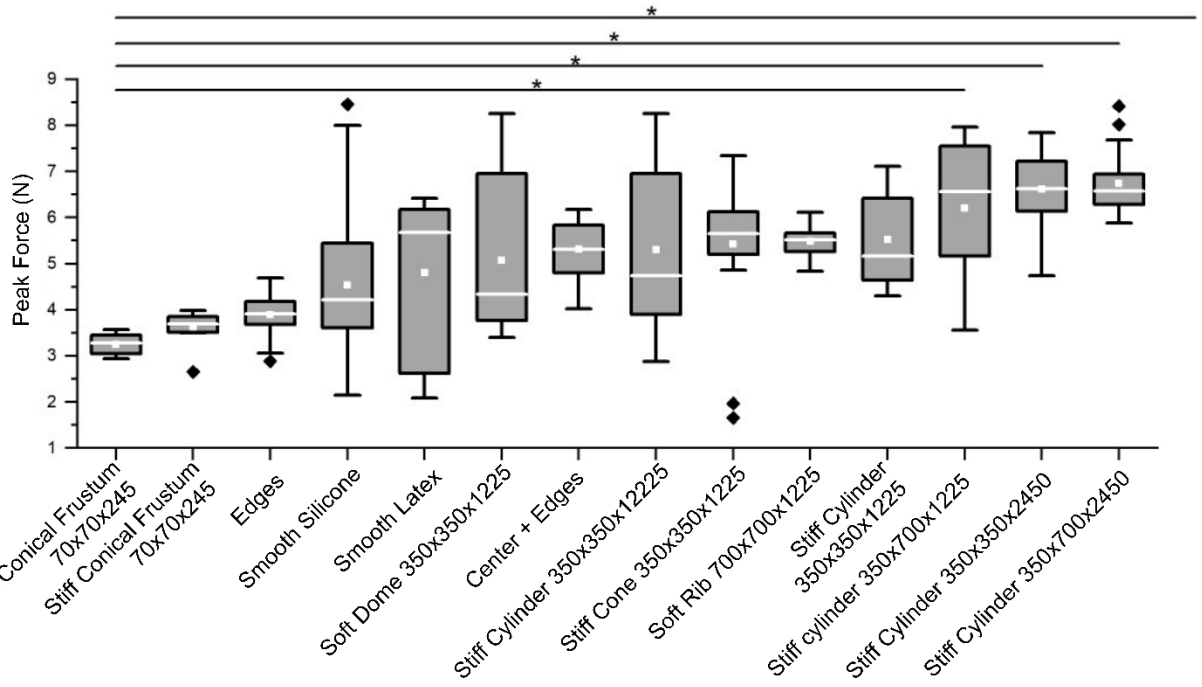

Figure 10: Pooled non-normalized results. Box plots show 25-75 percentile intervals of non-normalized results are much larger compared to normalized intervals.

2.3.9 Smooth Balloons

An additional "rougher" smooth silicone balloon molded to a 3D-printed surface was also investigated – smooth silicone (3D print-molded). All three smooth balloons have lower peak force compared to patterned balloons. Since smooth latex had the lowest peak force compared to both smooth silicone balloons ($p = 0.00764$ for PDMS molded, $p = 0.0286$ for 3D print-molded), I can conclude that this is likely a material property of latex. Indeed, latex is observationally less "sticky" than Ecoflex-30. Both smooth silicone balloons had statistically similar peak forces. This indicates a randomly rough surface with a relatively low degree of roughness does not affect peak force (Figure 11).

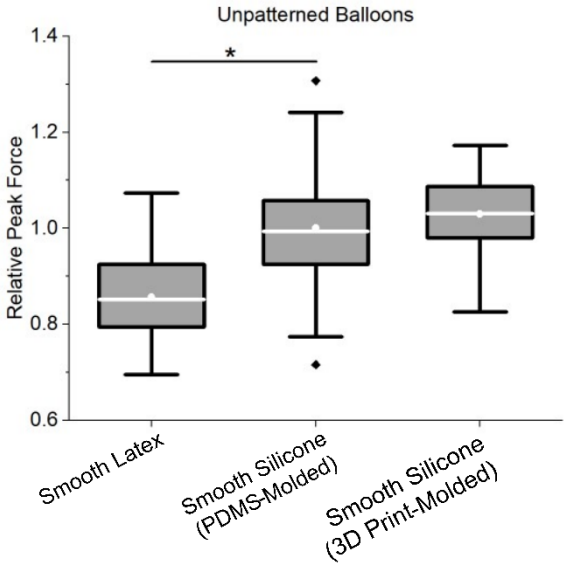

Figure 11: Comparison of smooth patterns. Both silicone patterns have similar peak forces. Both types of smooth silicone balloons have larger peak forces than the smooth latex balloons. This indicates a mildly rough surface does not affect peak force and latex balloons have the lowest performance.

2.3.10 Uninflated Balloons

Peak force between inflated smooth silicone, uninflated smooth silicone, and uninflated stiff 350x350x1225 domes are not significantly different. The only significantly higher peak forces are between inflated stiff 350x350x1225 domes and inflated and uninflated smooth silicone ($p = 7.00e\text{-}7$ and $p = 2.14e\text{-}6$, respectively). Additionally, both uninflated smooth silicone and uninflated stiff domes have statistically similar peak force compared to smooth latex peak force. This indicates patterned balloons will not have significant difficulties moving deeper into or pulling out of the small intestine at times when their anchoring properties are not needed (Figure 12).

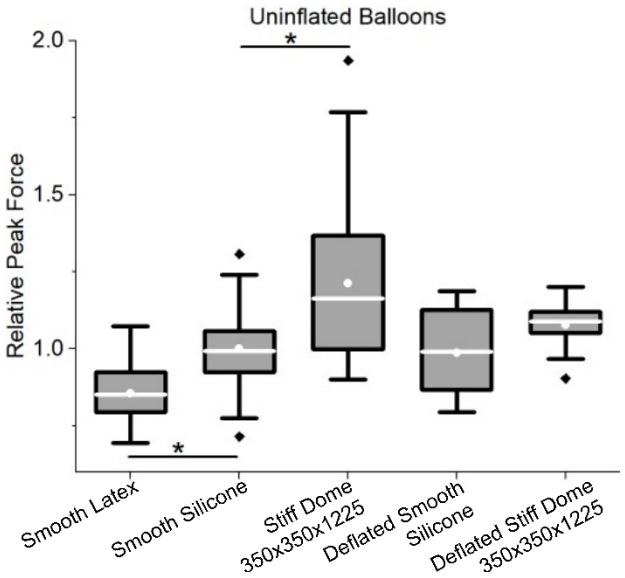

Figure 12: Comparison of peak force of inflated to uninflated balloons. Peak force of smooth silicone, deflated smooth silicone, and uninflated stiff 350x350x125 domes were statistically similar and significantly lower than peak force of the balloons patterned with stiff 350x350x125 domes. This indicates patterned balloons will not have significant difficulties moving deeper into or pulling out of the small intestine at times when their anchoring properties are not needed.

2.3.11 Effects of Inflation on Micropillar Morphology

Soft and stiff 70x70x245 conical frustums were stretched 100% to represent balloon inflation. Stretched samples were imaged with scanning electron microscope (Figure 13). Both soft and stiff features increase spacing when stretched. Soft features deform much more than stiff features. Soft features become shorter with a central depression with stretch compared to stiff features that look similar in their unstretched and stretched state. This finding may extrapolate to other micropillars where soft features deform more with balloon inflation than stiff features, though both become more widely spaced. With an inflation stretch of 100%, spacing between micropillars effectively doubles. Thus, in this example the lower limit for micropillar spacing, during inflated balloon use, is double the limit for spacing micropillars on the balloon during fabrication.

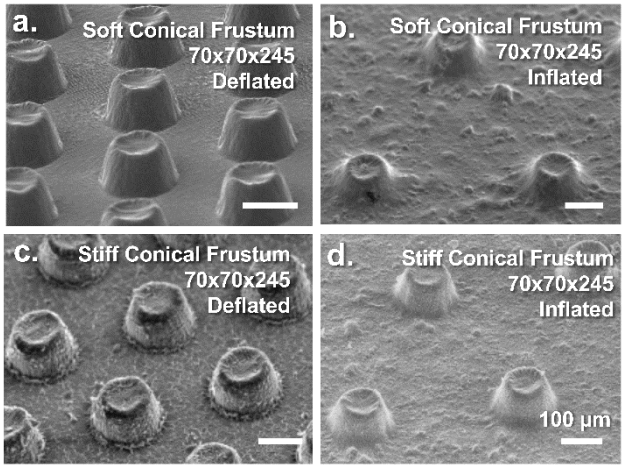

Figure 13: **Soft and stiff 70x70x245 conical frustums change geometry with stretch.** (a) Unstretched soft conical frustums change morphology with stretch (b), becoming more widely spaced, shortening, and developing a central depression. (c) Unstretched stiff conical frustums do not change morphology with stretch (c) and only become more widely spaced.

2.3.12 Balloon Cleaning and Performance over Multiple Trials

The effect of multiple uses was studied to investigate if tissue or balloon damage affects peak force. A linear regression was fit to peak force versus trial number for each balloon. A one-sample t-test compared the regression slope and was nonsignificant. This indicates no significant linear trends with trial number were observed. A representative sample of the peak force of ten individual balloons over ten pull trials is shown in Figure 14a. Endoscopy balloons must anchor the overtube multiple times during a procedure and are not cleaned during intubation. In this case, it is ideal to have a balloon that does not lose performance with use. This data suggests that both balloons and tissue do not change with use.

A paired t-test compared peak force between pull tests where balloons were cleaned with an alcohol wipe and those that were not. Eight balloons were compared with five cleaned pull tests and five non cleaned pull tests. There is no significant difference between peak force of balloons that were cleaned with an alcohol wipe between trials and those that were not (Figure 14b). This potentially reflects a balloon's performance during its intended use. During endoscopy, balloons are not cleaned between each inflation and anchoring and it is important for balloons to retain performance even when coated with small intestinal residue.

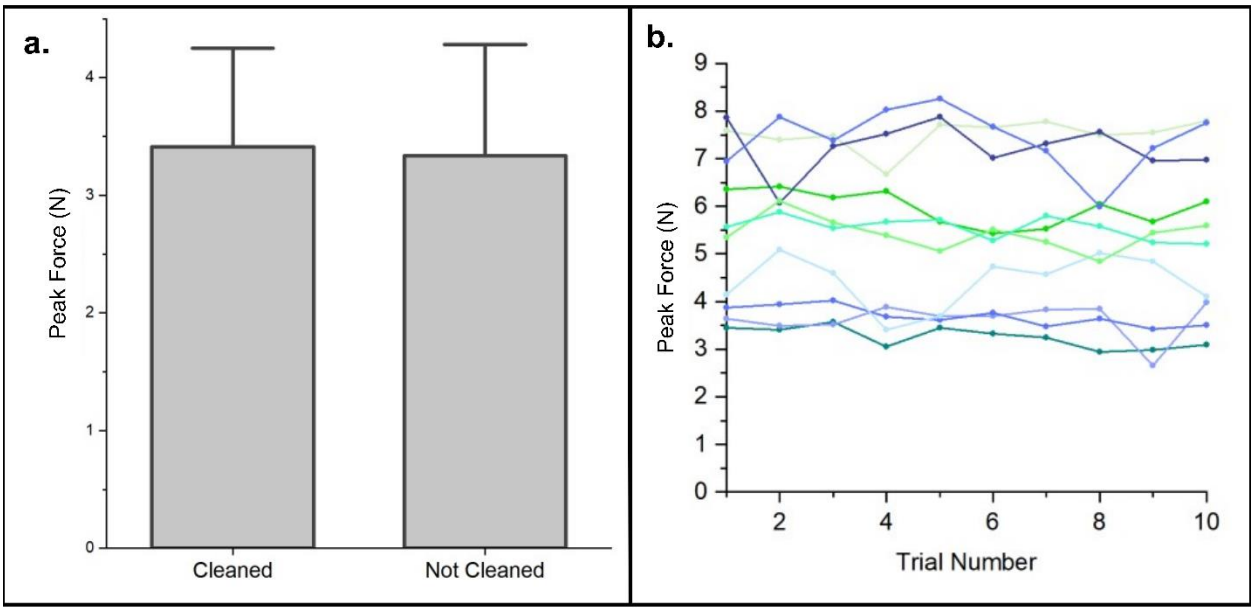

Figure 14: Balloon performance with use is consistent. (a) Cleaned and not cleaned balloons have the same peak force. Balloons have similar behavior when used multiple times. This is representative of a balloon's use in endoscopy where it will anchor multiple times during a procedure. (b) No trend is observed in balloon performance over multiple uses. A representative sample of ten individual balloons tested shows that balloons retain their anchoring properties as they are used.

2.4 Conclusions

Enteroscopy balloons were fabricated with micropillars and determined larger, stiffer, conical micropillars that cover a large surface area of medical balloons increase their anchoring abilities to soft, mucus-covered intestinal substrates. First, I demonstrate the ability to add micropillars to curved surfaces. Most micropillar research to date is on planar surfaces (Carbone and Pierro 2012; Brodoceanu et al. 2016) and most textured medical devices are random rough surfaces (Calobrace et al. 2018) or in the case of hip implants, negative dimples (Roy et al. 2015; Ghosh et al. 2015), making this technique an important tool for increasing the range of micropillars and types of objects that can be patterned. For example, textured stents with superior anchoring could reduce migration. Patterned medical robots could benefit from application-specific contact properties. For example, medical robots utilized in the intestine could improve traction and/or locomotion against the intestine resulting from wheels or tracks with micropillars (Sliker et al. 2012; Formosa et al. 2019).

Second, I demonstrate that patterning balloons can increase peak force relative to smooth balloons. Stiffer, larger, conical patterns over the entire balloon surface have improved performance. Future work should focus on specific micropillar attributes and the mechanisms by which micropillars anchor to soft tissue.

Finally, I demonstrate improvement upon balloon enteroscopy. Additional translational studies are indicated such as balloon testing with an endoscope in-vivo where gastroenterologists can give feedback on device performance. I have overall demonstrated that the addition of micropillars to medical devices can have profound effects on their performance. With further investigation, patterned balloons could lead to more effective balloon enteroscopies, resulting in wider adoption of balloon enteroscopy procedures among gastroenterologists and improved patient outcomes.

CHAPTER 3

FRICTION MECHANICS OF DEFORMABLE SOFT MICROPILLARS IN CONTACT WITH SOFT SUBSTRATES

3.1 Introduction

In the previous chapter, I demonstrate that texturing endoscopy balloons with micropillars significantly enhances their anchoring to ex-vivo small intestine. Here, I investigate the underlying friction mechanisms of soft micropillars and soft substrates. More specifically, I investigate the effects of straining micropillar arrays, akin to balloon inflation, on their friction against a soft substrate with and without a lubricant, simulating interaction with the wet, mucus-lined small intestine.

Most micropillar mechanics research focuses on enhancing dry adhesion against stiff substrates (Hensel, Moh, and Arzt 2018; Brodoceanu et al. 2016). However, the friction properties of micropillars, particularly against soft substrates, remain poorly understood. Little is known about the properties or underlying mechanisms behind soft micropillars contacting soft materials, including basic contact mechanisms such as friction (Style et al. 2018). Tribological properties are difficult to investigate due to the soft, distensible nature of these systems (Pitenis et al. 2017). In this chapter I present a custom traction measurement platform and evaluate the effects of strain, micropillar stiffness, and lubrication on friction. I also develop finite element methods that describe this system.

Knowledge of micropillar mechanics for soft materials is important for a variety of applications. Most micropillar applications tend to comprise two areas: climbing robots (Hawkes et al. 2013; Krahn et al. 2011; Li et al. 2012) and pick-and-place grippers (Hensel, Moh, and Arzt 2018; H. Tian et al. 2019). However, an intimate knowledge of soft-on-soft

micropillar friction mechanics is particularly relevant to the medical field where compliant devices interface with soft tissue. Many medical devices may benefit from tuned contact properties with tissue, allowing application-specific friction. But very few utilize specifically engineered device-tissue interfaces. As discussed in previous chapters, micropillars assist capsule-style robots in moving along tissue, primarily in the gastrointestinal system. The addition of micropillars to a wheeled robot has demonstrated superior traction compared to a smooth wheel on in-vivo abdominal tissue (Sliker et al. 2012). A capsule endoscope utilizes micropillars on caterpillar-style treads and was easily steerable in ex-vivo, insufflated colon (Formosa et al. 2019). Other experimental or theoretical gastrointestinal robots utilize micropillars for increased purchase on the intestinal wall as well (Karagozler et al. 2006; B. Guo, Liu, and Prasad 2019). A greater understanding of the mechanisms by which micropillars can enhance friction can improve these devices.

Micropillars with real-time tunable friction properties may be even more useful for devices that change conformation or interaction with tissue such as the endoscopy balloons I discuss in Chapter 2. A balloon with increased friction on the small intestine when inflated for anchoring, but reduced friction when uninflated and advancing or retracting could result in more effective procedures. I have shown that micropillars increase endoscopy balloon anchoring force on the small intestine (Bowen et al. 2020), but their mechanisms of action remain unknown. Here, I investigate the role of strain, akin to balloon inflation on friction between soft micropillars and soft, tissue-like substrates.

Most micropillar research focuses on adhesion of unlubricated, relatively soft micropillars against a rigid substrate. However, a few groups have explored soft micropillar friction on soft tissue substrates. Sitti's group explored friction between PDMS cylindrical micropillars and a cleaned, flattened small intestine sample lubricated with silicone oil. They

found both micropillar diameter and lubricant viscosity influence friction, with peak friction occurring at a 140 μm diameter and higher viscosities. Zhang et al found that cylindrical PDMS micropillars have increased friction compared to smooth PDMS in rabbit small intestine (Zhang et al. 2016; 2017). I previously show that endoscopy balloons with micropillars have superior anchoring in ex-vivo small intestine compared to smooth balloons. Micropillars that are stiffer, larger, and cover move surface area are attributes that further increase anchoring (Bowen et al. 2020).

Both micropillar material and shape influence their friction against rigid substrates. Stiff, high aspect ratio (tall and thin) micropillars have demonstrated high friction against glass (Majidi et al. 2006). Tian et al. found that iron oxide additives alter the stiffness of PDMS micropillars and their friction (Y. Tian et al. 2015). Zimmer et al. also fabricated textured ridges where PDMS micropillars are attached to a flexible, inflatable backing layer. When this backing layer is inflated, contact with the glass substrate increases, increasing shear force. They also found that more compliant materials resulted in higher friction. Kim et al investigated micropillar shape. They chemically etched cylindrical micropillars to create conical or hourglass shapes. Friction against glass initially increases, then decreases with further etching. A suggested mechanism is that increasing lateral contact increases friction. An ideal micropillar in this scenario would be maximally compliant – thick, tall micropillars and short, thin micropillars bend less than micropillars of medium height and width and have less lateral contact with the substrate (Y. Kim et al. 2014). Combining micropillars of different shapes and/or sizes in a hierarchal format can increase or decrease friction. Badler, et al. created surfaces that combine mushroom-shaped micropillars and ridges, finding that different structures result in differing friction properties (Badler and Kasem 2020).

Further, several groups have investigated friction through wrinkle formation, another type of microtexture. Ohzono et al. created wrinkles by either compressing a textile embedded in an elastomer or relaxing a pre-stretched elastomer with an embedded textile. Parallel wrinkles form along the thread lines, resulting in wavelength-dependent adhesion (Suzuki and Ohzono 2016; Ohzono and Teraoka 2017). Several groups have also created wrinkles by uneven swelling of polymers and other materials. These wrinkled surfaces have altered adhesion properties relative to smooth surfaces, but little is known about their friction (Kato et al. 2016; Chan et al. 2008; Kundu et al. 2011). Jeong et al. combined wrinkles and micropillars. By adding parallel rows of micropillars to a strained surface, parallel wrinkles form on relaxation, changing micropillar orientation. When strained, the micropillars are normal to a substrate and when unstrained, the micropillars are angled. The angled micropillars have decreased friction and adhesion relative to strained, normal micropillars (Jeong, Kwak, and Suh 2010).

Some modeling work has been done on micropillar contact mechanics, though methods are not well established. Soft textures and soft substrates are two deformable and nonlinear contacting bodies, making modeling this system particularly challenging. Indeed, few usable theoretical or analytical models exist for these systems. Kern et al. investigated the effects of micropillar geometry on adhesion between soft cylindrical micropillars and a soft substrate. They used a triangular representative volume element, hyperelastic material models, and a cohesive zone model, finding that backing layer contact contributes to adhesive force. When micropillars have a lower aspect ratio or are more widely spaced, more backing layer contact occurs, increasing adhesion (Kern, Long, and Rentschler 2018). Skondras-Giousios et al. sheared a smooth, SiO_2 sphere against a two dimensional planar array of soft, high aspect ratio micropillars. Both coefficient of friction and cohesive zone models were used. These

models intuitively found that increasing micropillar density increases resultant friction (Skondras-Giousios, Karkalos, and Markopoulos 2020).

Despite considerable advances in the fabrication of micropillars with altered contact properties relative to smooth substrates, few have explored the mechanisms behind these effects. Furthermore, most of this work focuses on adhesion against rigid substrates, leaving soft micropillar friction against soft substrates relatively unexplored. In this chapter, I investigate the behavior and mechanisms behind soft micropillar friction with soft substrates. This chapter focuses on the behavior and underlying mechanisms between soft, distensible microtextures and their friction interactions with soft substrates. Here, I characterize friction of soft, distensible micropillar arrays and model this behavior. I investigate the effects of micropillars strain, lubrication, and stiffness on their friction properties.

3.2 Methods

3.2.1 Micropillar Fabrication

Micropillars used for this study were fabricated from a laser cut Kapton mold. They are approximately 140 µm in diameter, with an aspect ratio of 0.5 (micropillar base is 2 times larger than the micropillar height), 245 µm center-to-center spacing, and a 1 mm thick backing layer. The hyperelastic Ecoflex-50 backing layer (SmoothOn, Inc.) allows for significant strain. Micropillars were made from either Ecoflex-50 or a stiffer silicone rubber SmoothSil-960 (SmoothOn, Inc.) and are referred to here as softer and stiffer micropillars, respectively. Sheets of micropillars on a backing layer were strained with a custom device. This device uses channels that slide past each other to increase distance between a ring of bolts. The bolts puncture the micropillars and backing layer. Sandpaper washers and nuts further secure the bolts to the micropillars. The equally biaxially strained surface can be

considered the center of this ring (Figure 15). Three representative micropillars from 0, 25, 50, 75, and 100% strain were imaged at 50x magnification with a Keyence VK-X1000 Laser Scanning Microscope. For coefficient of friction testing, radially strained micropillars were glued to an acrylic backing with SilPoxy silicone adhesive (Smooth-On Inc., Easton, PA). An additional piece of acrylic was bolted on the free side of the textured piece further secure the strained micropillars.

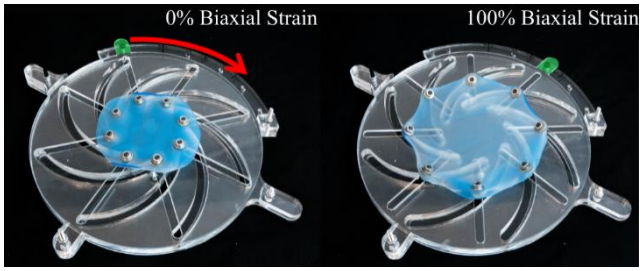

Figure 15: A sheet of micropillars is bolted to a spinning system to create equal biaxial strain

3.2.2 Experimental Coefficient of Friction Measurements

Bulk friction measurements were made with a custom friction measurement device (Figure 16). This device pushes a substrate sled over another material with adjustable normal load, stroke length, and speed. A servo motor picks up and places the substrate sled. The sled mounting system uses a single through-axle pin, allowing for interchangeable sleds of differing sizes, shapes, and materials. The clear mounting platform allows imaging and has bolt holes for easy sample changing. Two orthogonal sets of four load cells measure normal and traction force, respectively. A Data Acquisition device (DAQ) collects force data from the load cells. A custom MATLAB code processes this data, calculating coefficient of friction as the ratio between normal and traction forces at a manually selected steady state.

Soft polyvinyl chloride (PVC) serves as a soft substrate. A 2mm-thick layer of PVC was heat-bonded to an acrylic tube, forming the substrate sled. The circular shape minimizes edge effects. Friction between PVC and three textures was evaluated: softer Ecoflex-50 micropillars, stiffer SmoothSil-960 micropillars, and smooth Ecoflex-50. Each texture was strained to 0, 25, 50, 75, or 100% biaxial engineering strain. Friction was measured with a 0.588N (60g) load at 5mm/s sliding speed. Friction measurements were performed with and without a mineral oil lubricant (Hydrobrite, Sonneborn). The lubricant may resemble the fluid and mucus found in biologic systems. Thirty tests were performed for each strain, material, and lubrication, resulting in thirty cases. Outliers were removed and results pooled.

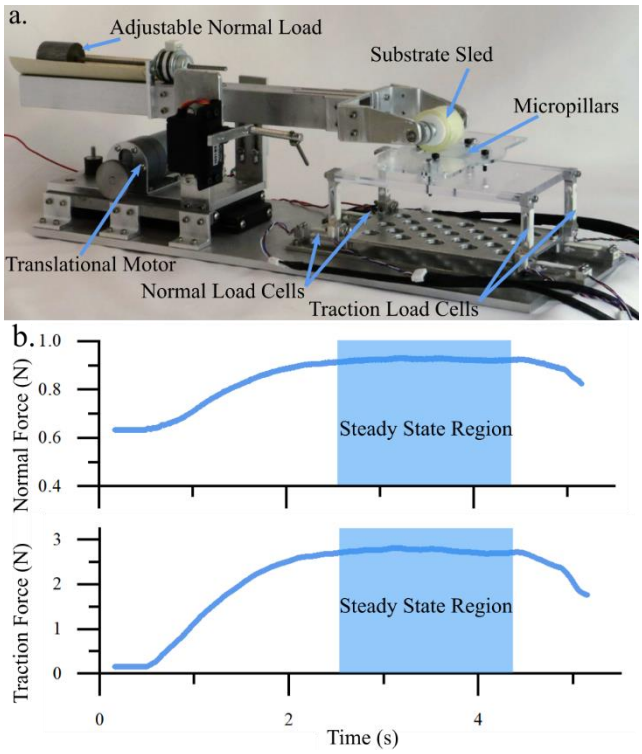

Figure 16: Experimental setup to measure coefficient of friction between soft micropillar arrays and a soft substrate (a) A custom friction measurement device pushes a soft substrate sled over strained micropillar arrays at a set speed and load. Four pairs of perpendicular load cells concurrently record normal and shear forces. (b) Coefficient of friction is averaged from the ratio between normal and shear forces at steady state.

Modeling

A finite element model was constructed to explore the mechanisms behind experimental results. A model allows investigation of how spacing and geometry individually contribute to friction, compared to the experiment where they cannot be unentangled. A sliding friction model is computationally expensive due to large deformation of the soft, hyperelastic materials. Thus, the model presented here qualitatively reflects the experiment to reduce computational expense due to the high-deformation, complex nature of the system.

A two-dimensional plane strain model represents a cross section of the experimental setup in the shear direction. A two-dimensional model reduces computation time, though it approximates the micropillars as ribs versus circular features. Additionally, the model assumes boundary lubrication and laminar flow between micropillars and substrate, further discussed in *3.3 Conclusions*.

The assembly consists of two components: the substrate sled and micropillars on a backing layer. Hyperelastic material models were fit to uniaxial strain data collected with an Instron tensile testing device for the softer micropillar and backing layer material Ecoflex-50, stiffer micropillar material SmoothSil-960, and PVC sled. A 2mm-thick PVC circle segment (60 degrees) with radius 60 mm is constrained by a rigid half circle backing to represent the substrate sled.

Three micropillar *shapes* and two *spacings* are modeled as four *representations*. The shapes include a simplified cylindrical shape, the unstrained shape, and the strained shape of the soft micropillars at 100% strain. Since the model is two dimensional, each shape is actually a rib. The cylindrical shape is simplified to a roughly cylindrical micropillar. The unstrained and strained shapes follow confocal profilometry measurements. These shapes primarily differ in their sidewalls with the cylindrical features having a vertical sidewall and

no taper, the unstrained shape having a medium sidewall taper, and the strained shape having a large amount of sidewall taper. The cylindrical, unstrained, and strained representations each use the same micropillar shapes between 1x and 2x spacing and this is a cylindrical, unstrained, or strained shape respectively. A fourth representation, the realistic representation, varies micropillar shape with spacing to reflect the true unstrained and strained profiles. The unstrained micropillars at 1x spacing and strained micropillars at 2x spacing form the realistic representation. For all representations the micropillars themselves are not strained to remove potential effects of strain stiffening.

Micropillars are constrained from displacement in the indentation (vertical) direction along the bottom backing surface. The edges of the micropillar part are constrained in the shear (horizontal) direction. Substrate displacements are applied to a reference point at the center of the substrate sled. Two quasi-static steps occur during the simulation. First, the sled indents into the micropillars. This step is displacement-controlled rather than force-controlled like the experimental setup. Next, the PVC wheel shears 1cm or until steady-state sliding occurs (Figure 17).

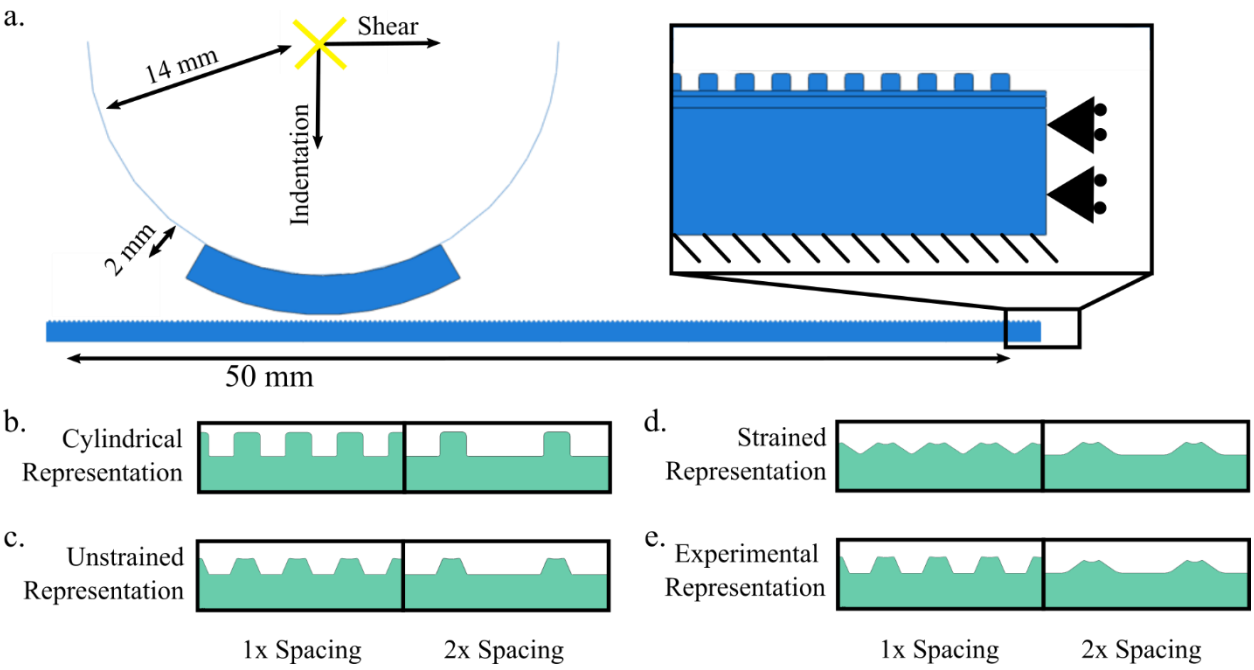

Figure 17. Finite Element Model of soft micropillar indentation and shear. (a) The simulation consisted of three two-dimensional planar parts. An arc of soft, hyperelastic material was attached to a rigid half circle, representing the substrate sled. Indentation and shear were applied at a reference point at the center of this semicircle (yellow "X"). The substrate sled indents and shears into the micropillar part while reaction forces are recorded at the reference point. (b) Four micropillar geometries are simulated and micropillar spacing is varied to represent pillar strain. First, micropillars are simplified to a cylindrical representation where their cylindrical shape do not vary with spacing. (c) For the unstrained representation, micropillar shape does not change with spacing and is made to reflect unstrained micropillar shape. (d) The unstrained representation varied=s spacing with a constant geometry that reflects the strained micropillar shape. (e) Finally, for the experimental representation, micropillar shape reflects micropillar strain so that shape changes as pillars become more widely spaced.

A coefficient of friction describes interaction between the substrate and micropillars and is set as the experimentally determined coefficient of friction between lubricated smooth Ecoflex-50 and the PVC substrate sled, 0.044. Both cohesive zone model and coefficient of friction interactions were modeled, but yielded similar results. So, only the coefficient of friction model is interpreted and shown here.

Geometry, contact area, strains, and stresses during indentation and shear are the primary outcome parameters for the models. Results are determined for multiple indentation depths and interpolated for a load of 0.15 N to match the force-controlled experiment. Micropillar material models were also compared for Ecoflex-50 and SmoothSil-960. The backing layer for both these micropillar parts was Ecoflex-50.

3.3 Results

3.3.1Micropillar Geometry

Unstrained micropillars are shaped like conical frustums with an average height of 80.48 μm, top diameter of 83.19 μm, bottom diameter of 149.61 μm, and center-to-center spacing of 249.879 μm. A two-tailed t-test yields $p>0.05$ for these measurements between soft and stiff micropillars, indicating their unstrained shapes are similar. As micropillars are biaxially strained from 0-100%, soft micropillars deform more than stiff micropillars. Two-tailed t-tests ($p<0.05$) compare data between 0 and 100% strain. Height and top diameter significantly decrease while the bottom fillet and bottom diameter significantly increase for the soft and stiff micropillars. The top fillet, central crater radius, and central crater depth do not significantly change. The soft micropillars become significantly shorter and develop a significantly larger bottom diameter compared to the stiff micropillars (Figure 18).

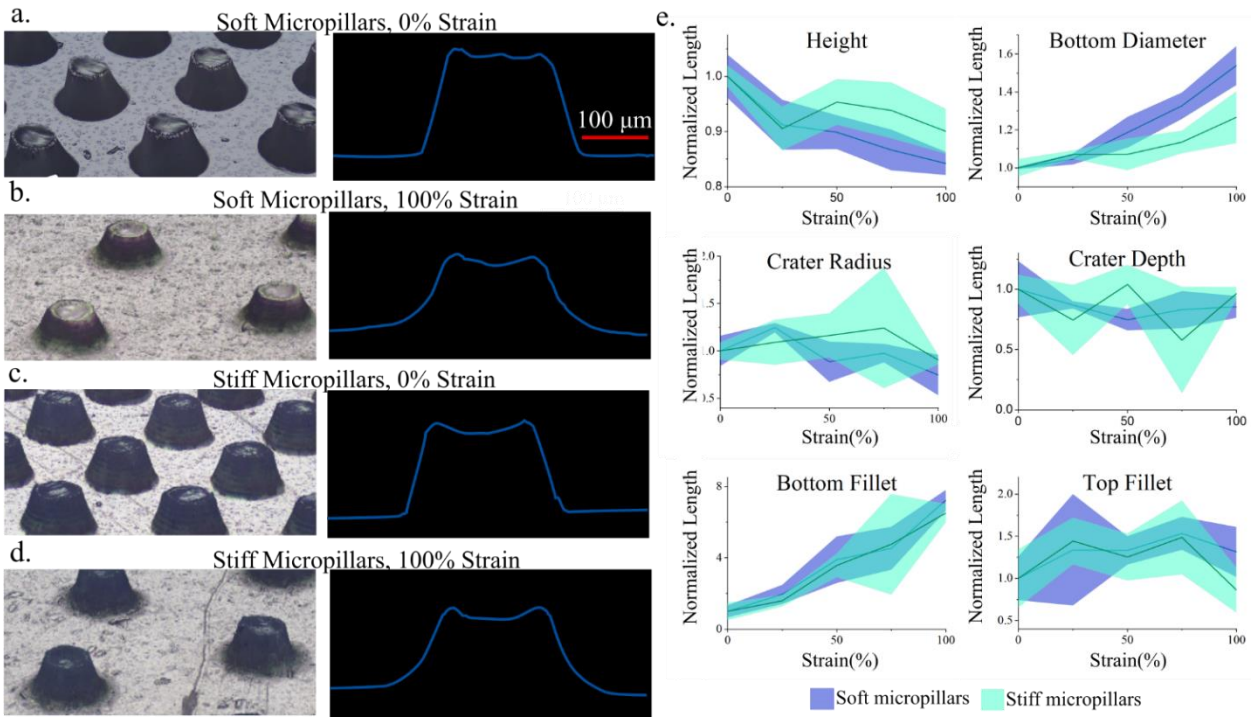

Figure 18. Soft micropillars deform more with strain compared to stiff micropillars. (a-d) three-dimensional surface images (left panel) and single micropillar profiles (right panels) for soft and stiff micropillars at 0% and 100% strain show changes to micropillar spacing and shape with strain (e) Height, bottom diameter, and bottom fillet change significantly with strain while crater radius, crater depth, and top fillet do not when measured by optical profilometry. Soft micropillars deform more than stiff micropillars. Their height decreases and bottom diameter increases much more than stiff micropillars when strained.

3.3.2 Experimental Results

Coefficients of friction between micropillars and soft substrates trend with material, strain, and lubrication status. For the unlubricated case, untextured materials have the highest friction, followed by softer micropillars, then stiffer micropillars. Friction of the smooth material does not trend with strain. However, both softer and stiffer micropillar friction increases proportionally with strain. For the lubricated case, the smooth surface has the lowest friction, followed by softer micropillars, then stiffer micropillars. This is the opposite trend to the unlubricated findings. Again, the smooth surface's friction does not trend with strain. Friction decreases with strain for both micropillar types. Friction is higher in unlubricated samples compared to lubricated samples. The difference in coefficients of friction between materials is larger in the unlubricated samples compared to the lubricated samples (Figure 19).

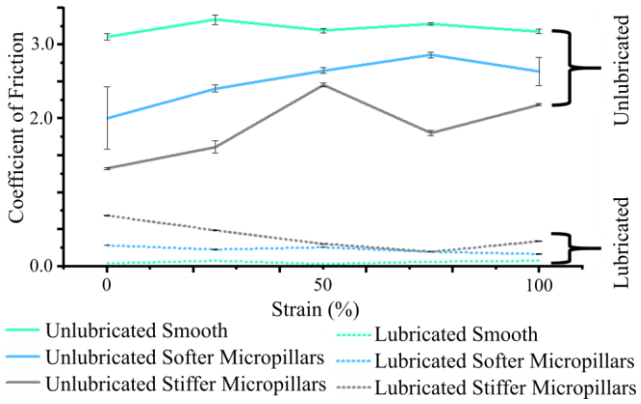

Figure 19: Experimentally determined coefficient of friction reverses trends in unlubricated compared to lubricated tests. For unlubricated friction, untextured silicone has the highest coefficient of friction, then soft textured, then stiff textured. Soft and stiff textured materials increase friction with strain while untextured silicone does not seem to have a relationship with strain. For lubricated friction, stiff textured materials have the highest friction, then soft textured and untextured materials. Both textured materials decrease friction with strain.

3.3.3 Modeling

Both contact models, coefficient of friction/lubricated and cohesive zone model/unlubricated, reach steady state shear. Coefficient of friction was taken as the ratio between normal and tractive forces during steady state sheer. However, relative coefficient of friction trends are similar between the two models. This indicates the interaction models cannot fully describe steady-state coefficient of friction. Therefore, model coefficient of friction results are not considered here. However, other aspects of the models, namely the deformation between micropillars and substrate, identify several factors that contribute to friction behavior. Normal stresses and strains were examined during indentation and shear. σ_{11} during indentation and ε_{22} are the most illustrative and are discussed below.

Geometry and stress at the end of the indentation step are shown below. Indentation depth was set to achieve equal normal force for all representations. Contact between substrate and backing layer occurs for more tapered micropillar shapes and larger spacing, the 2x spacing for unstrained and strained representations. This suggests that more conformal contact with micropillar and substrate may increase unlubricated ones. More compressive stress occurs at the top corners of the micropillars and increases with increased spacing and decreased sidewall taper, suggesting that increased micropillar stress correlates with lubricated friction.

Substrate distension increases with increased micropillar spacing. 2x cylindrical and unstrained shapes visibly deform with indentation and appear pushed out of the way by the indenting substrate. The 2x spacing strained shape does not deform. This is likely due to the more conformal contact of the strained representation relative to other representations. 1x spacing shapes do not visibly deform either, potentially due to the increased number of micropillars to distribute stress.

Tensile stress occurs in both the micropillar backing layer and substrate where they are both distended between the micropillars. Regions of higher stress extend further into the substrate and backing layer for more widely spaced micropillars, showing that increased micropillar density relieves some of this stress. Negative micropillar stress concentrations tend to occur at corners. Positive stress concentrations occur where substrate and backing layers are distended, indicating that the micropillars stretch these regions. Regions of higher stress also extend further into the backing layer for more widely spaced micropillars. This indicates that the micropillars push against both their backing layer and the substrate to create regions of distension spanning the space in between micropillars. This suggests a competing effect of strain on friction. Increased spacing from 1x to 2x increases substrate deformation because stress is less distributed between features. Features with less sidewall taper also increase substrate deformation, such as the unstrained compared to the strained micropillar shape (Figure 20).

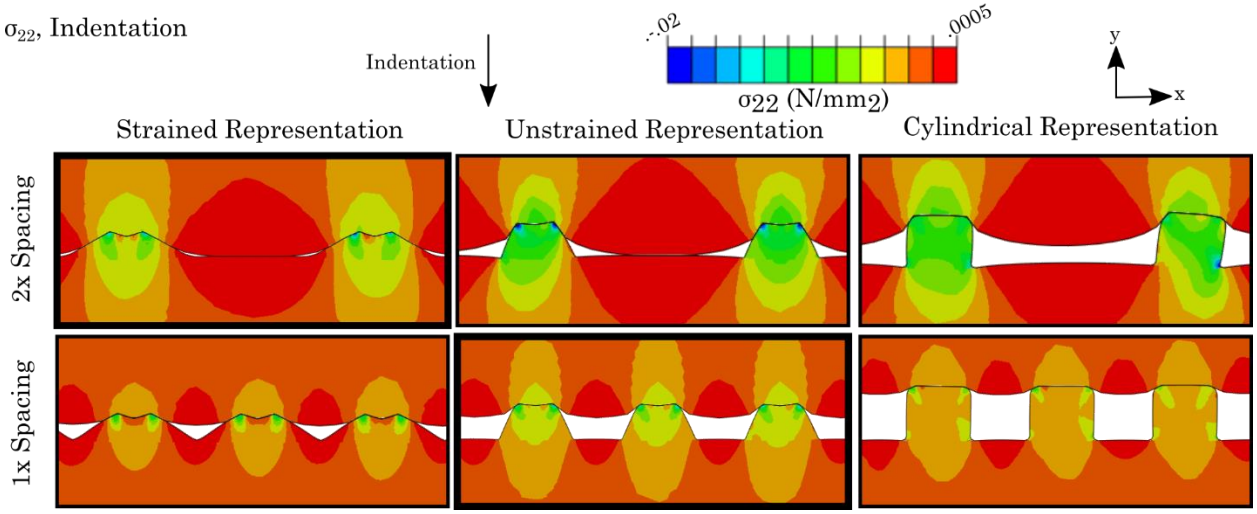

Figure 20: Principal Normal Stress for Micropillar Indentation. Normal stresses were recorded at the end of the indentation step at the same normal indentation force for varying micropillar geometry and spacing. The experimental representation is outlined with a bold border. Contact between substrate and micropillar backing layer increases for more tapered micropillar shapes (unstrained and strained geometries) and larger spacing. More compressive stress occurs at the micropillar top corners. Compressive stress increases with increased micropillar spacing and decreased sidewall taper. Maximal tensile stress occurs in the backing layer and substrate that is deformed between the pillars. Stress on individual pillars increases with pillar spacing.

Normal strains in the direction of shear were recorded during the shear step. Micropillars tilt towards the direction of shear for the unstrained 2x representation and the cylindrical 1x and 2x representations. None of the other representations visibly deform with shear. This indicates that micropillars tilt more with increased spacing and decreased sidewall taper.

Strain is greater in the substrate compared to the micropillars. An arc of compressive strain occurs in substrate where it distends between micropillars. This arc is asymmetric for the 2x unstrained and cylindrical representations, but is more symmetric for the strained representation. This is potentially because the substrate and micropillars highly conform for the 2x spacing strained shape. For all 2x spacing simulations, a tensile region occurs where the substrate contacts the micropillar tops. This tensile region enlarges as micropillar sidewall taper decreases. Compressive strain occurs at the tops of the micropillars, increasing with increased spacing. This strain is generally asymmetric and shifted away from the direction of shear. Another small region of compressive strain occurs in the bottom corners in the direction of shear for the unstrained 2x spacing and cylindrical 2x spacing representations. This correlates with the visible tilt of these micropillars compared to the strained representation and unstrained 1x spacing representation. Overall, representations with higher strain tend to be more widely spaced and have less sidewall taper and micropillars with these attributes may have higher lubricated friction (Figure 21).

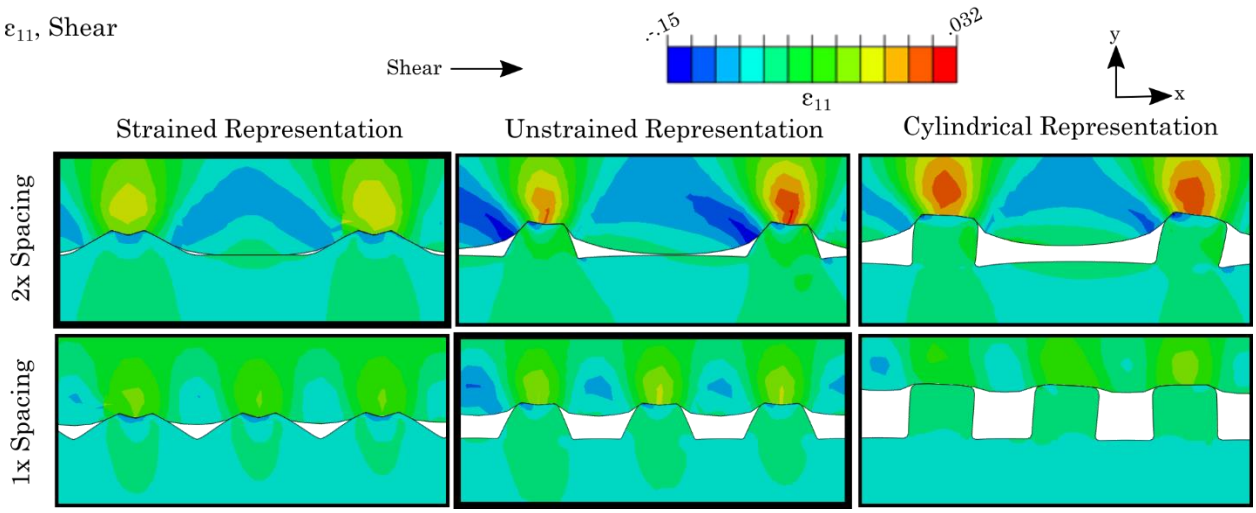

Figure 21: Principal Strain Results for Micropillar Shear. Normal strains were recorded during substrate shear against the micropillars. The experimental representation is outlined with a bold border. Visible micropillar deformation occurs for the unstrained representation for 2x spacing and for the cylindrical representation for both spacings. The substrate experiences higher strain compared to the micropillars. A compressive strain band occurs in the substrate between the micropillars for 2x spacing. This is asymmetric for the unstrained and cylindrical 2x representations but is symmetric for the strained 2x representation. A region of tension occurs across the top edge of all 2x spacing features and increases with decreasing sidewall taper. Strain is much lower for all 1x spacing representations.

Contact length, the two-dimensional equivalent of contact area, may explain experimental friction results for the unlubricated/cohesive zone model. As more of the micropillar contacts the substrate, the force required to separate the two surfaces may increase. Contact area increases with spacing for both the strained and experimental geometries, supported by the close conformation of substrate and micropillar. Contact area increases with increased micropillar spacing for both the strained and unstrained geometries. This is likely due to increased backing layer and sidewall contact. Contact area decreases with increased spacing for the cylindrical geometry. This is likely because backing layer contact is not achieved and only the micropillar tops are in contact. With fewer micropillars per unit length, contact area decreases with increased spacing if backing layer and sidewall contact does not occur (Figure 22).

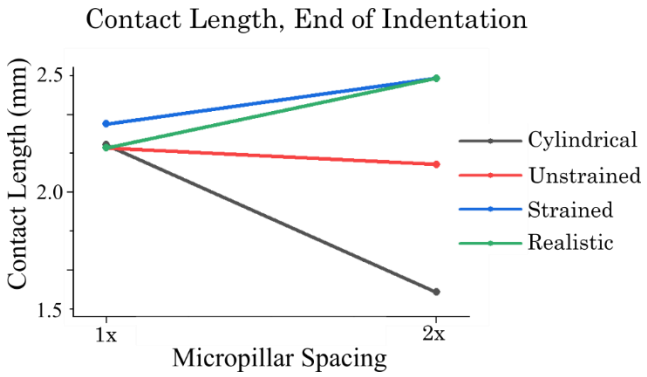

Figure 22. Contact area correlates with experimental unlubricated friction. The length of contact between micropillar substrate was measured at the end of indentation. Contact length increases with spacing for strained and experimental representation but decreases for cylindrical and unstrained geometries.

Combined with experimental results, modeling supports differing potential mechanisms for lubricated and unlubricated friction. Lubricated friction correlates with representations that have increased micropillar and substrate deformation. These increase with increased micropillar spacing and decreasing sidewall taper. This suggests that increased lubricated friction occurs with increased micropillar and substrate deformation, but particularly substrate deformation with high distension and regions of distortion that have a small radius of curvature. Thee tend to be produced by micropillars that are spaced where they can most penetrate into the substrate and have the least tilted sidewalls, allowing for increased stress concentrations. Unlubricated friction correlates with contact area. Contact area increases with micropillar strain and sidewall taper. This suggests that unlubricated friction may be adhesion-dominated so that micropillars with greater contact area have greater adhesion and thus, require more force to separate micropillars and substrate.

Micropillar stiffness modeling supports these suggested mechanisms. Softer and stiffer micropillars interact differently with the soft substrate, pointing to differing friction behavior. Softer micropillars deform more compared to stiffer micropillars at the same normal force. Stiff micropillars deform the substrate more at the same normal force. The indentation depth, or total distance between rigid top of substrate and bottom of the micropillar part is greater for soft micropillars.

Stiffer micropillars penetrate more into the substrate because they compress less than softer micropillars. Stiffer micropillars cause higher substrate strain compared to softer micropillars, a likely mechanism for their increased lubricated friction.

Softer micropillars have larger contact length compared to stiffer micropillars at the same normal force. This increased contact length may be responsible for the softer micropillars' higher unlubricated coefficient of friction (Figure 23).

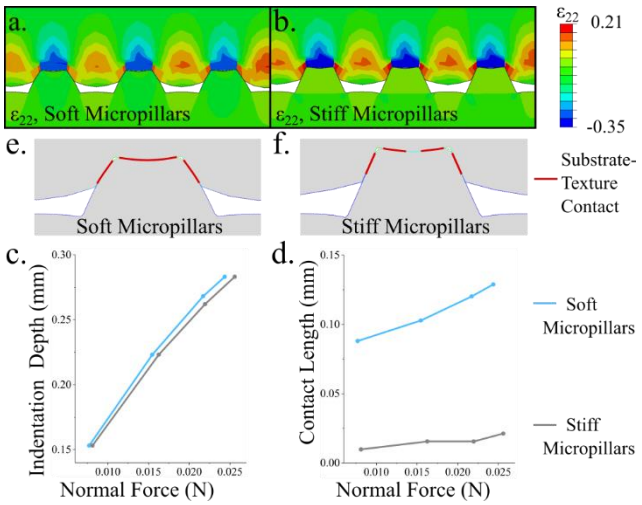

Figure 23. Softer and stiffer micropillars interact differently with a soft substrate, explaining their differing friction behaviors. (a) Soft micropillars deform more than stiffer micropillars, but stiffer micropillars deform the substrate more, shown here as strain, for the same indentation force. (c) Indentation of softer micropillars is greater compared to stiffer micropillars to produce the same normal force (d) contact length between micropillars and substrate is greater for softer micropillars compared to stiffer micropillars (e) Contact for softer micropillars goes further down the sides, and is more continuous for the top compared to stiffer micropillars (f) for the same indentation depth.

These modeling results suggest a complex interplay of micropillar shape, spacing, and stiffness. For lubricated friction, micropillar shape and spacing may be competing mechanisms. Micropillars with less sidewall taper, such as the unstrained micropillars, may have less conformal contact with the substrate, contributing to their higher friction. Increased micropillar spacing results in more deformation of micropillars and substrates. Smaller micropillar spacings have relatively less stress and strain, which may contribute to less lubricated friction. In addition, stiffer micropillars produce higher substrate strain and deformation, potentially leading to their higher friction. Contact area correlates with increased friction for both the realistic representation and micropillar stiffness. For adhesion-dominated interactions, increased contact area may make it more difficult to separate micropillars and substrate in contact. This suggests that adhesion is the primary mechanism for unlubricated friction.

3.3 Conclusions

In this chapter, I explore the effects of straining micropillar arrays on their friction against soft substrates through experiment and finite element modeling. Strain alters micropillar spacing and geometry, and thus micropillar-substrate interactions.

A custom traction measurement platform measured coefficient of friction of strained micropillars with and without a lubricant. For the lubricated case, micropillars have a larger coefficient of friction compared to a smooth control. Stiffer silicone micropillars have larger friction compared to softer micropillars. Friction decreases with strain for the lubricated micropillars. For the unlubricated case, these trends reverse, indicating differing mechanisms between systems. The smooth surface has the largest coefficient of friction and stiff micropillars have the lowest. Friction increases with increasing strain.

A finite element model describes the experiment and suggests multiple mechanisms that contribute to system friction. This model identifies some of the main mechanisms behind soft texture friction and thus focuses on qualitative trends. In future work, as this model becomes more refined, it may become quantitative so that it can be used to iteratively design micropillar improvements.

Micropillar shapes with increased sidewall taper results in more conformal contact between micropillar and substrate, increased contact area, decreased stress, and decreased strain. Increased spacing results in higher stresses, strains, and both substrate and backing layer distension. Increased micropillar stiffness results in higher substrate distension and lower contact area. From these findings, I conclude that unlubricated friction is likely adhesion-dominated so that interfaces with higher contact area have higher friction. Lubricated friction is dominated by substrate deformation. These proposed mechanisms suggest a stiffer micropillar with a pronounced tip may produce the most friction. Indeed, the stiff cone micropillar in Chapter 2 produced some of the largest anchoring forces of any micropillar type tested.

Future versions of this model should aim to improve in a few areas. The interaction models used, a coefficient of friction and cohesive zone model, do not adequately describe the experimental differences seen with the addition of a lubricant. These interaction types are not well established in finite element modeling for soft, high-deformation materials and present an important area for future research. Material limitations also exist. This model relies on hyperelastic materials, but steady-state shear may be better described with the addition of viscoelasticity or strain hardening. Finally, this model is two-dimensional. Three-dimensional models are possible, but a parametric study like the one described in this chapter is very computationally expensive.

Fluid flow is assumed to be laminar in this model. Calculating Reynolds number using a kinetic viscosity of 10-14 mm^2/s, flow speed of 5 mm/s based on the shear speed between substrate and micropillars, and a characteristic length of 245 μm based on the center-to-center micropillar spacing yields a value of 0.49, indicating laminar lubricant flow. Since the Reynolds number is small, the drag coefficient is also small, estimated at 0.001. This is much lower than the experimental coefficient of friction between the soft substrate and a smooth lubricated material, 0.044. Since the estimated drag coefficient is about 2% of the total friction coefficient, it is reasonable to neglect it for these simulations. Future simulations may focus on the fluid effects for larger micropillars, lower viscosity fluids, or higher speeds.

From the work presented in this chapter, I conclude that straining soft micropillars changes their shape, changing their friction properties. The mechanisms for unlubricated and lubricated friction differ. The findings presented here have important implications for future applications, namely compliant, deformable devices that contact soft materials.

CHAPTER 4

FRICTION MECHANICS OF ASYMMETRIC SOFT TEXTURES

4.1 Introduction

Textures with asymmetric friction properties have potential utility in applications where increased force, or decreased slip is desirable in one direction compared to another. This chapter focuses on friction of asymmetric soft textures on soft substrates. This area is of particular interest in medical applications. Esophageal stents, for example, migrate distally 18% of the time (Freeman, Vyverberg, and Ascioti 2011; Anderloni, Lollo, and Repici 2019). Directional textures could increase friction in the direction of food movement, reducing migration. Lower friction in the proximal direction could make these stents easier to remove compared to traditional esophageal stents. Internal stents such as ureteral stents require low friction during placement but need high friction in the direction of urine flow when placed (al-Aown et al. 2010). 45% of intravascular stents migrate distally (Zarins et al. 2004; Resch et al. 1999), indicating a need for devices with superior friction. Catheters, J-tubes, and external wearable devices could benefit as well.

Enteroscopy balloons could also utilize textures with directional friction. They often slip when anchoring against the walls of the small intestine and are discussed in greater detail in Chapter 2. Asymmetric friction could improve balloon anchoring (pulling proximally) and still allow for easy advancement (pushing distally). Other active, tissue-contacting devices with asymmetric textures could move efficiently with low friction towards the direction of advancement but high friction in the direction of slip. For example, the experimental Endoculus enteroscopy robot utilizes symmetrically textured treads (Formosa et al. 2019), but may benefit from directional ones.

Asymmetric textures occur naturally where they alter many animals' interactions with their environment, inspiring morphology of and applications for synthetic asymmetric textures. The most canonical example of asymmetric animal texturing for grip is the gecko. Geckos have microscopic sets of setae on their footpads. These flexible textures angle backwards towards the gecko's tail and can produce attachment forces of three times the gecko's weight (Autumn and Peattie 2002). Gecko contact with rigid, dry materials have been extensively characterized, particularly normal and shear adhesion, equivalent to static friction. Attachment and detachment of setae from substrate occur at different orientations. The setae flip towards the gecko's head for attachment, are pushed down, then the foot pulls backwards towards the animal's tail. Setae peel away from the substrate during detachment (Autumn et al. 2000). Geckos have demonstrated excellent attachment to rough surfaces as well, though these mechanics are less well-characterized. Geckos have variable attachment abilities to different wavelengths of synthetic rough surfaces (Huber et al. 2007; Gillies et al. 2014). This is scale-dependent. Some wavelengths allow conformation of the gecko toe, some allow conformation of sub-structures, etc. This is thought to be due to both footpad structure size and compliance (Takahashi et al. 2006). Gecko attachment to soft surfaces is much less understood.

These fibrillar textures also rely on the concept of contact splitting to enhance the gecko's climbing ability. The use of multiple features compared to a single smooth surface reduces failure of the entire footpad. The experiences of one feature do not necessarily affect the experiences of other features. Essentially, not all features fail concurrently and contact defects do not propagate to all features as compared to a single surface (Kamperman et al. 2010; Majumder, Sharma, and Ghatak 2010). Although contact splitting is well-established to contribute to the adhesion properties of these types of textures, it is unclear what effects these have on friction.

The textures described in this work also share some attributes of shark denticles. Shark skin is covered by small, tilted, triangular features that point backwards towards the shark's tail (Ankhelyi, Wainwright, and Lauder 2018). The denticles produce a rough texture and alter the shark's contact with water (Anderson, McGillis, and Grosenbaugh 2001). This allows for efficient motion of the shark through water. In dry applications, sharkskin has demonstrated asymmetric friction where friction is less in the direction the denticles point and higher away from the direction the denticles point (Manoonpong et al. 2016).

However, even the basic mechanics of this type of system are unknown. Most soft texture and micropillar research focuses on adhesion of soft, symmetric features against rigid substrates. This work addresses a different mechanics problem: asymmetric soft texture friction against soft substrates. However, it is still useful to review the work done on other types of soft textures.

A common way to achieve textures with anisotropic friction is manufacture cylindrical features at an angle rather than perfectly vertical. Angled soft features have demonstrated asymmetric static friction/shear adhesion (T. Il Kim et al. 2009; J. Lee, Fearing, and Komvopoulos 2008)) and kinetic friction (Zhengzhi Wang 2018; Moon et al. 2010) against smooth, rigid materials. Asymmetric but vertically oriented micropillars (Tamelier, Chary, and Turner 2012) as well as vertically oriented features with asymmetric tip shapes such as triangles (Kwak et al. 2011; Jin et al. 2014), spatulas (Murphy, Aksak, and Sitti 2009; J. H. J. Lee et al. 2014; Xue et al. 2014), and step-shaped Ts (Yue Wang et al. 2016) have demonstrated higher friction in one direction compared to another. Directional friction has also been shown against rough rigid surfaces with slanted features that decrease stiffness going towards the feature tip (Zhengzhi Wang 2018).

Relatively less work has been done on the contact between soft textures and soft substrates. Van Assenberg, et al. explored the effects of surface and internal features on

friction and shear forces, but did not directly compare directionality (P. van Assenbergh et al. 2020). For soft substrates, shear forces generated are highest for materials with low normal stiffness and higher shear stiffness due to increased contact. More deformable substrates have increased shear stiffness. They also found that internal geometries (rows of pores) significantly contributes to shear forces.

The work presented in this chapter investigates mechanisms of asymmetric micropillar-like textures when both features and substrate are soft. Specifically, I look at friction behavior as feature stiffness changes with and without a lubricant.

4.2 Methods

4.2.1 Texture Fabrication

Textures consisting of individual *features* were fabricated using a reverse molding method. Texture positives were 3D-printed (FormLabs). Each feature making up the texture was designed to be cylindrical and tilted at 30 degrees relative to vertical. A negative mold was created from the texture positives out of SmoothSil-960, a silicone rubber. Finally, silicone rubber texture positives with a 1mm thick backing layer were molded from the negative mold. These texture positives are those used experimentally. A layer of Mold Release (Reynolds) separated the micropillars. Textures were produced from four hyperelastic materials: Ecoflex-10, Ecoflex-30, Ecoflex-50, and SmoothSil-960 (Smooth-On, Inc). The Ecoflexes are a family of silicone rubbers whose suffixes reflected their Shore hardness. Thus, Ecoflex-10 is the softest material, Ecoflex-30 is stiffer, and Ecoflex-50 is the stiffest. The moduli for the Ecoflex materials tested are 55, 69, and 83 kPa respectively. SmoothSil-960 is the stiffest material tested with a stiffness of 1930 kPa (Smooth-On 2013).

Feature morphology was measured with a confocal laser profilometer. Features are roughly cylindrical, about 821 μm tall, and are tilted 30° from vertical. They are angled with

a more rounded top corner away from the tilt and a more pointed corner in the direction of tilt. The base is slightly wider than the top. The entire feature cross section is circular and top parallel to backing layer (Figure 24).

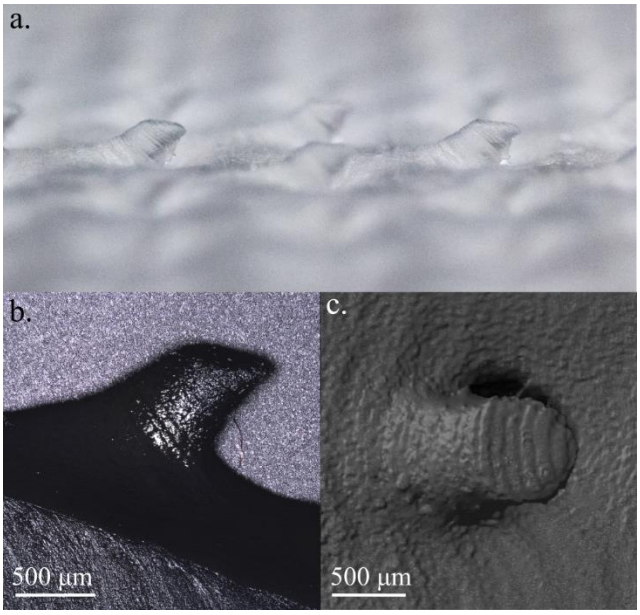

Figure 24: Asymmetric textures are fabricated as tilted features shaped like conical frustums. (a) light microscopy image of features arranged in a texture, image courtesy of Brian Johnson (b) confocal profilometry side view of a single feature (c) confocal profilometry top-down view of a single feature

A soft polyvinyl chloride (PVC) substrate was fabricated by polymerizing PVC and heat-bonding a 2 mm-thick layer to an acrylic tube. The substrate was designed to be cylindrical to minimize edge effects and for ease of fabrication. PVC is soft and distensible, making this material desirable as a substrate. This is the same substrate material used in Chapter 3.

4.2.2 Experiment

Coefficient of friction was determined between the soft silicone textures and soft substrate using a custom traction measurement device, previously described in Chapter 3: Friction Mechanics of Deformable Soft Micropillars in Contact with Soft Substrates. This device moves a substrate at constant speed across another material (in this case, the textures) and calculates coefficient of friction as the ratio between traction and normal forces between substrate and textures at steady state.

Coefficient of friction was measured for each texture material against the soft substrate. Two shear directions were measured, either towards or away from the direction of feature tilt. Normal force was set at 0.16 N, equivalent to a 60g load. Friction was measured with and without a mineral oil lubricant for each direction. A total of 30 trials were performed for each set of experimental conditions (texture material, direction, and lubrication). Video and still optical microscopy images were taken of the leading and trailing substrate edges for the unlubricated experimental setup. Lubricant caused significant optical distortion of the texture-substrate interface, so imaging was not performed for the lubricated experiments (Figure 25).

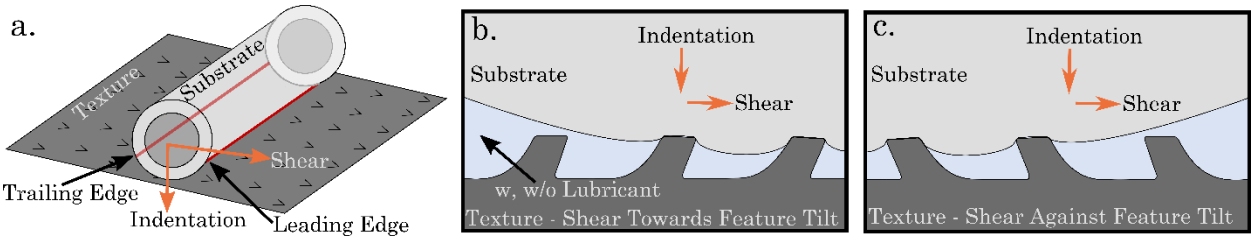

Figure 25: Experimental Setup Drawing. (a) A soft substrate indented and sheared into soft micropillars textures while coefficient of friction was measured at steady state. Texture stiffness was varied for four elastomeric materials ranging from modulus 55 kPa to 1931 kPa. Sliding friction was measured with and without presence of a lubricant. (b-c) Close-ups of features, substrate, lubricant, and direction of shear. Coefficient of friction was compared between two shear directions - towards feature tilt or against feature tilt.

4.2.3 Simulation

A two-dimensional plane strain finite element model was developed to describe the experiment and mechanisms of texture-substrate interaction (Abaqus, Dassault Systémes). In this model, an arc of soft circular substrate material shears across texture. The arc is bonded to a rigid circular backing, representing the soft PVC substrate bonded to the acrylic tube. The substrate is modeled as a hyperelastic material with stiffness of 6 kPa. Texture stiffness is varied by changing the stiffness coefficient of a neo-Hookean hyperelastic model:

$$W = C_1 (I_1 - 3) \tag{4.1}$$

This equation describes the strain energy density function for an incompressible neo-Hookean solid Here, W is the strain energy density, C_1 the stiffness coefficient, and I_1 the identity matrix.

A cohesive zone model is used to describe the interaction. Both a coefficient of friction and frictionless model were compared but produced similar results. Thus, only a cohesive zone model is considered here. Cohesive zone models describe crack formation between two contacting surfaces in terms of stress. The bilinear cohesive zone model is triangular and situated on 2 axes: stress and distance along the cohesive zone/crack. Interaction is influenced by three terms. First, work of adhesion, w_{adh} describes the energy that adheres the two surfaces and is the area of the triangle. Maximum stress, σ_{nn} describes the stress at which two points decohere. Finally, k_{nn} describes the stiffness of this interaction, or the slope of the left half of the triangle (Figure 26).

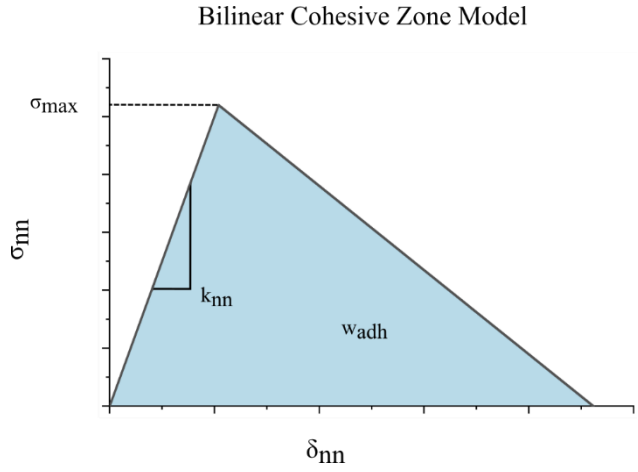

Figure 26: A bilinear cohesive zone model describes adhesive behavior between surfaces.

Cracks propagate across this zone as the surfaces separate. Here, a bilinear cohesive zone model is used with a separation stiffness (K_{nn} and K_{tt}) of 0.5 N/m^3, maximum stress (σ_n) of 2.6x10^{-2} N/mm^2, and adhesion energy of 0.012 mJ/mm^2. This interation is used in shear and both normal (x and y) directions. The primary outcome measure of this simulation is visualization of feature deformation for varying stiffness and interaction (cohesive zone model vs. frictionless). Stresses, strains, and contact area are also investigated (Figure 27).

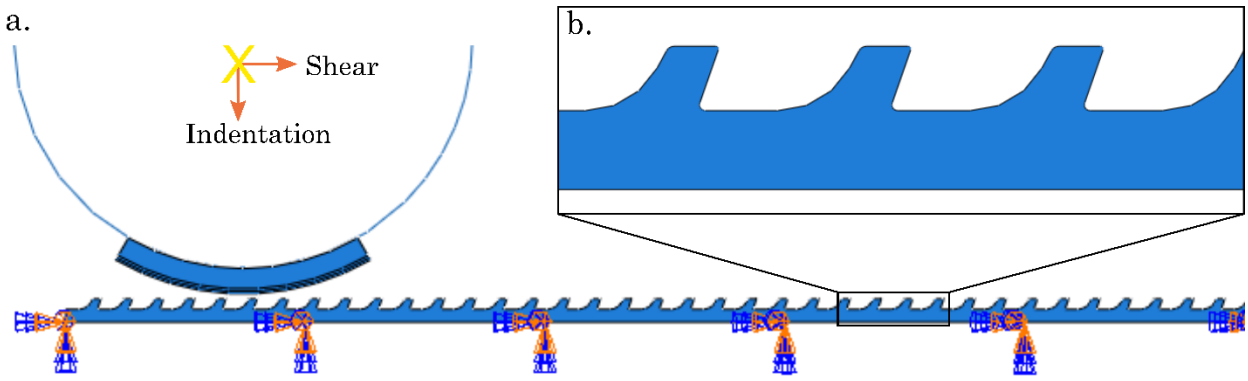

Figure 27: Finite Element Model. A two-dimensional plane strain finite element model describes the experiment. (a) A hyperelastic semicircular substrate indents into and shears across the hyperelastic asymmetric texture. The location and shear direction of the substrate indenter are mirror images for each shear direction. Thus, shear occurs either away from or towards the feature tilt. Cohesive zone models and frictionless interactions describe the unlubricated and lubricated experiments, respectively. (b) Textures follow the profile measured with a laser profilometer.

4.3 Results

4.3.1 Experimental Results

For the unlubricated experiment, coefficient of friction is larger for shear towards feature tilt compared to shear away from feature tilt. This difference is significant for the three softest textures. There is no significant difference in coefficient of friction with direction for the stiffest texture. Coefficient of friction generally decreases with increasing texture stiffness. The magnitude of the difference in directional coefficient of friction (coefficient of friction with shear towards feature tilt – coefficient of friction with shear against feature tilt) increases with increasing Ecoflex stiffness, but is the smallest for the stiffest material, SmoothSil-960.

Lubrication lowers coefficient of friction and generally reverses friction trends compared to unlubricated friction. Coefficient of friction is larger with shear away from angle of feature tilt friction with shear towards direction of feature tilt. This difference is nonsignificant for the softest texture material but is significant for the three stiffer materials. Friction generally increases with increasing texture stiffness. The magnitude of the difference in friction between the two shear directions also increases with stiffness (Figure 28).

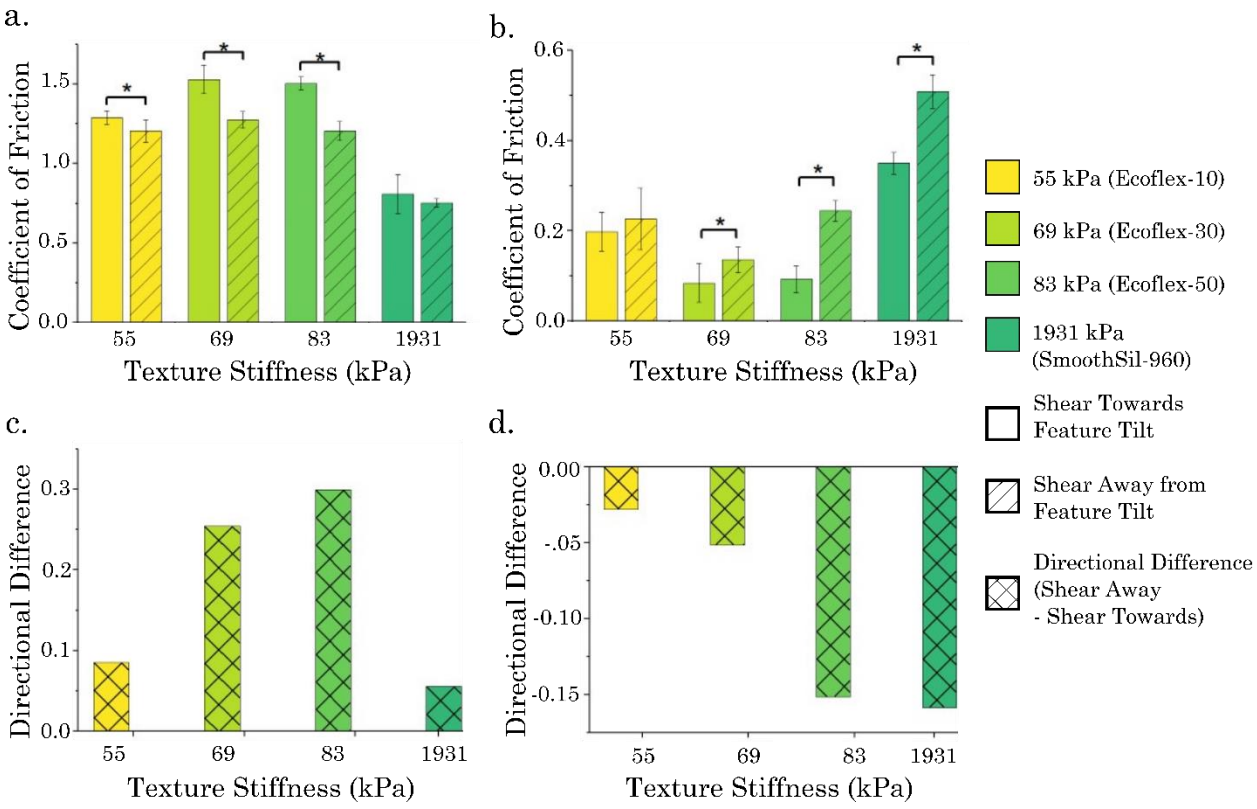

Figure 28: Experimental Coefficient of Friction Results. (a) Coefficient of friction for each experimental group is reported with standard deviation error bars. Unlubricated friction is highest for shear towards feature tilt compared to shear away from feature tilt. Coefficient of friction generally decreases with increasing texture stiffness. (b) Coefficient of friction trends reverse when a lubricant is added so that friction is highest for shear away from feature tilt compared to shear towards feature tilt. Coefficient of friction increases with increasing texture stiffness. (c) For unlubricated friction, the directional difference, or the difference in coefficient of friction between the two shear directions, increases with increasing feature stiffness. (d) This reverses with lubrication, so that the directional difference is negative and larger for stiffer textures.

Video microscopy footage captured the interaction between substrate and textures for unlubricated friction. Addition of a lubricant caused too much optical distortion for video footage of similar quality and utility to be obtained. Soft and stiff unlubricated micropillars exhibit differing behavior. All of the softer materials (Ecoflexes) appeared similar in videos, so only the softest material, Ecoflex-10 is shown. For soft features sheared towards feature tilt, features are pushed downwards along the leading edge. Features bend down along most of their length as the substrate passes over them. For the trailing edge, as the substrate passes away from the features, each feature springs back up as the substrate passes by. Feature tops scrape against the back edge of the substrate as features become more vertical. The features themselves are bent over, and spring back up when released by the substrate.

Soft textures sheared away from feature tilt show different behavior. Rather than flattening, these features bend backwards as the substrate pushes up against feature tips. The feature deforms backwards as the substrate shears over them and spring back to their original orientation when unloaded. Shear towards the feature tilt produces much more contact between substate and texture since the lateral side of the feature can contact the substrate. For shear against feature tilt, each feature has less contact with the substrate (Figure 29).

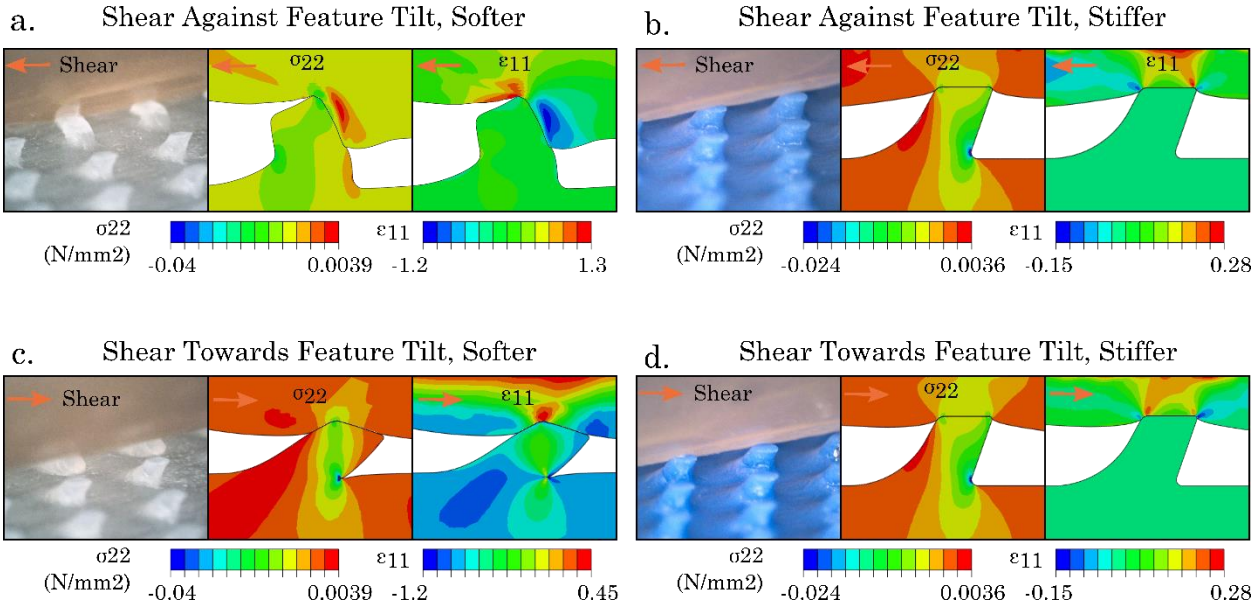

Figure 29. Texture-Substrate Interaction. Substrate shear towards or against feature tilt is shown for softer and stiffer textures. Intermediate stiffnesses display behavior in between the two stiffnesses shown. From left to right, each set of panels includes an experimental unlubricated video still, simulation normal stress (σ_{22}), and simulation normal strain (ε_{11}). (a) Softer features sheared against the direction of feature bend backwards against the substrate. This causes a buildup of substrate material on the trailing (against shear) lateral side of the feature. (b) Stiffer features sheared against the direction of feature tilt do not deform as much. Substrate deformation here is relatively concentrated around the top of the feature. (c) Softer features sheared with feature tilt flatten out against the backing layer. (d) Stiffer features sheard with the direction of feature tilt also deform very little and concentrate substrate deformation at their corners.

Modeling

Plane strain 2D finite element models were developed with two interaction types between texture and substrate, a cohesive zone interaction and frictionless interaction. Models did not converge to reach steady state shear. This is due to the high deformability of textures and substrate. Images were manually selected during the shear step that had realistic deformations and resembled experimental images. Outcome measures were feature-substrate deformation, normal stresses, normal strain as well as indentation depth, deformation, and normal strain with normal indentation for several material stiffnesses.

Simulated texture stiffness was varied by changing the C_1 coefficient of a Neo-Hookean hyperelastic material model. A soft substrate indented to depths that produced the same normal force for each material stiffness. Softer materials required larger indentation depths to achieve the same normal force. The softest features deform more compared to stiffer features. The softest features fold along their tilted axis towards the backing layer, flattening, and making a region of high at the most folded corner. The softest features also have a tensile region that extends from backing layer through the feature center or "core". Feature deformation decreases as feature stiffness increases and substrate deformation becomes concentrated at the top feature corners. Stiffer features have much less strain than the softest feature. The substrate has a region of compressive strain over the top of the softest feature. As texture stiffness increases, substrate strain also increases. Tensile strain occurs the feature corners and compressive strain occurs over the feature tops (Figure 30b). This points to regions of concentrated substrate deformation as a driving factor for lubricated friction. Stiffer features create more concentrated regions of substrate deformation, potentially resulting in their higher lubricated friction.

For the same normal force, indentation depth decreases as texture stiffness increases. This means that for softer textures, more vertical compression occurs in the system compared

to stiffer textures for the same indentation force (Figure 30a). Contact length also decreases as texture stiffness increases (Figure 30c). This correlates with unlubricated friction, pointing to unlubricated friction mechanisms dominated by adhesion and contact area.

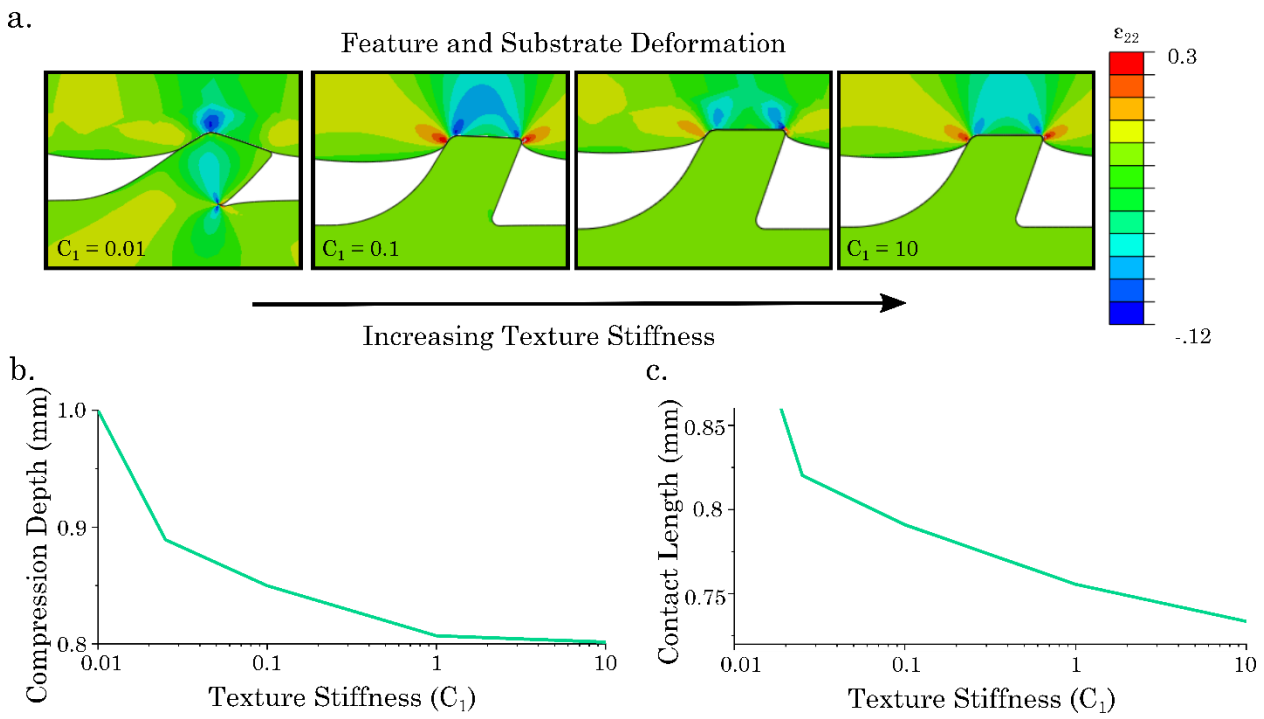

Figure 30: Effects of Texture Stiffness on Feature-Substrate Deformation. (a) Features and substrate deform less as texture stiffness increases. For very soft textures with significant deformation, strain is relatively less than that of stiffer features. Generally, strain decreases with increasing texture stiffness. (b) As texture stiffness increases, the substrate indents less to achieve the same normal force. (c) Contact length decreases as texture stiffness increases

Simulated deformation of unlubricated shear matches experimental video observations. The simulation uses a cohesive zone contact model to add adhesion, or stickiness, to the interaction between texture and substrate. Other contact models produced similar results. This suggests textures may deform similarly with lubricated and unlubricated friction, though this cannot be confirmed using the methods described in this chapter.

Softer textures sheared against feature tilt are deformed backwards so that they tilt opposite their original direction. Positive stress is concentrated in the substrate as it builds up against the trailing edge of the feature. Negative stress is concentrated in the feature at its tip. Most deformation occurs in the substrate. This creates a pushing effect behind the feature and pulling effect across the top of the feature to tilt it backwards. Relatively little strain occurs in the soft feature, but a band of increased stressed occurs across the middle of the feature. Tensile strain is concentrated where the substrate shears over the feature top. Compressive strain occurs in the same region as the stress concentration. These findings suggest that for softer features sheared against the direction of feature tilt, the substrate builds up against the trailing side of the feature, causing the feature to tilt over. (Figure 29a).

Stiffer features deform much less compared to the softer features. The substrate deforms less compared to the softer features when sheared against feature tilt. This may be because it takes quite a bit of substrate deformation to tilt the softer features backwards. However, the substrate does experience deformation with a smaller radius of curvature as it deforms around the stiffer feature corners. Substrate stress decreases over the tops of the features and increases as it distends between features. Negative strain occurs at the feature tip corner towards the direction of shear and positive strain occurs over the top of the feature. The high feature stiffness prevents significant feature deformation (Figure 29b).

Softer features sheared towards feature tilt flatten in the direction of tilt. The substrate conforms to the top and side of the flattened feature. Again, less stress occurs over the top of the feature in the substrate and positive strain occurs in this region as well. Negative strain and positive stress occur between the features. The contact for soft features clearly differs between the two directions. Contact area cannot be compared between the two since the simulation moves, making it difficult to select which frames and features to calculate contact for (Figure 29c).

Finally, stiffer features sheared towards feature tilt deform very little. Stress concentrations are similar for the stiffer features sheared in different directions. Strain patterns are similar as well but occur in the substrate on different sides of the feature (Figure 29d).

Overall, modeling results show that softer features deform much more compared to stiffer features. Softer features bend backwards when sheared against the direction of feature tilt. They flatten when sheared towards feature tilt. Stiffer features deform very little but cause substrate deformation and strain over smaller areas.

Differing substrate and texture interactions may explain experimental results and are supported by finite element models. Contact length (contact area in three dimension) increases with decreasing feature stiffness. It may be larger for softer features sheared towards the direction of feature tilt compared to shear against soft feature tilt. This supports the finding that unlubricated friction may correlate with contact area due to adhesion between textures and substrates. For the lubricated case, the geometry of the stiffer textures remains more intact compared to the high deformation of the softer features. The feature "sharpness" may remain with deformation for the stiffer features, resulting in higher friction and directional differences for stiffer features compared to softer features that deform readily.

4.3 Conclusions

In this chapter, I investigate the role of stiffness on friction of asymmetric textures and soft substrates. I find that softer textures behave differently compared to stiffer, but still soft, materials.

I successfully made textures with significantly different friction between two shar directions. The features I fabricated have a relatively simple geometry – arrays of slanted cylinders - but produce significant differences in directional friction. It is notable that the equipment and materials to manufacture these textures are inexpensive. The 3D printer to make texture positives and silicone rubbers are commercially available and textures cure at room temperature. The ease and cost of manufacturing makes the textures described in this chapter available for a wide variety of applications. It is unknown if other, more complex shapes have superior asymmetric friction properties. The feature design space is almost infinite, and future work should focus on feature properties besides tilt that can enhance friction while keeping realistic manufacturing considerations in mind.

Interestingly, directional friction trends reverse with lubrication. The effects of shear direction and stiffness on friction are opposite for unlubricated versus lubricated texture friction. Visually, for the unlubricated case, very soft textures deform significantly, but as stiffness increases, they deform less. Soft ones flatten out when sheared in the direction of feature tilt and bend backwards when sheared away from the direction of feature tilt. Stiffer features do not visibly deform.

A finite element model with a cohesive zone interaction describes the unlubricated friction experiment. Simulated feature deformation resembles experimental observations,

providing a level of confidence. Stiffer textures deform less compared to softer features. The substrate deforms more sharply for stiffer features compared to softer features.

Many follow-up questions arise from the work presented in this chapter. Experimentally, many more areas can be investigated. Other soft materials may interact differently with other soft substrates. However, I expect polydimethylsiloxane (PDMS), a commonly used micropillar material, to show similar behavior since it is also a silicone-based elastomer. Hydrogel substrates may exhibit poroelastic behavior compared to the hyperelastic PVC substrate used for these experiments. Different sliding speeds and lubricants may change interactions as well, and warrant further study.

The finite element models described here cannot fully describe the complex nature of the interaction between soft, asymmetric features and a soft substrate. These models are rarely used to describe sliding friction. Methods are not well established for this type of system and are difficult to converge due to the high deformation. The finite element models used here are two-dimensional and qualitative, since they represent a simplification of this complex system. Yet, they still provide valuable information on the deformation of both texture and substrate. Future finite element work should focus on improved material models or contact behavior, allowing enhanced descriptions of soft sliding textures.

Finally, an enhanced understanding of soft, asymmetric friction is quite useful, particularly in the medical field where devices contact soft tissues. Enhancing textures can provide superior directional anchoring and sliding friction in often wet environments. Other potential commercial uses for asymmetric textures include food handling or underwater applications. Though the exact contact requirements are application-specific, this work presents new findings that can be used to enhance these interfaces.

CONCLUSIONS

The overall conclusions of this work include:

1. Patterned Enteroscopy Balloon Design Factors Influence Tissue Anchoring
    - Enteroscopy balloons can be manufactured with a wide variety of textures on their tissue-contacting surface.
    - Textures increase anchoring force relative to smooth balloons in ex-vivo intestine. This finding is true for all micropillars studied.
    - Features that are stiffer, larger, and cover move surface area produce higher anchoring forces.

2. Friction Mechanics of Deformable Soft Micropillars and Soft Substrates
    - I construct a custom platform that measures sliding coefficient of friction between two materials, in this case strained elastomeric micropillars and a soft substrate.
    - Experimentally, coefficient of friction increases with micropillar strain and for softer micropillars compared to stiffer micropillars. Micropillars have decreased friction compared to flat surfaces. These trends reverse with addition of a lubricant.
    - Micropillars deform with strain, but stiffer micropillars deform less than softer micropillars.
    - Finite element models support different mechanisms for unlubricated and lubricated friction between soft micropillars and a soft substrate. Unlubricated friction for this system may be dominated by adhesion - micropillars with higher

contact area have higher friction. Lubricated friction is higher for micropillars that produce more substrate distension and lateral contact result in higher friction. These factors also may contribute to the differences in friction for varying micropillar stiffnesses.

3. Behavior and Mechanisms of Soft Texture Friction Against Soft Substrates
    - Tilted soft features produce asymmetric friction against a soft substrate.
    - Coefficient of friction between soft, tilted textures and a soft substrate is larger for shear towards feature tilt compared to shear away from feature tilt. Coefficient of friction also decreases with increasing micropillar stiffness.
    - Experimental video shows softer features deform significantly and flatten in the direction of shear. Stiffer features do not visibly deform.
    - Like in Chapter 3, these friction trends reverse with lubrication.
    - Finite element analysis confirms experimental findings. Stiffer textures deform less, indent less into the substrate, and have lower contact area compared to softer textures. Substrate regions of stress and strain depend on feature deformation.

DISCUSSION

In this thesis I investigate translational medical device applications for micropillars and the underlying mechanisms of soft micropillar friction with soft substrates. Here, I consider unanswered questions and future research directions.

The next steps for the balloon enteroscopy work lie in the clinical and manufacturing realm rather than in bench research. Further evaluations should focus on clinical performance where experimental balloon evaluations occur during an enteroscopy procedure. Outcome measures for this type of study could compare time to complete procedure, number of times balloons slip, and subjective endoscopist experience between standard and experimental balloons. In addition, assessment of tissue for damage should occur. This should involve sectioning and histologic analysis of tissue used for balloon anchoring with micropillars compared to standard, commercially available balloons. Finally, practical manufacturing considerations such as scale-up, approved materials, and sterilization should be studied.

An additional topic for consideration is that the micropillar design space is infinite. Micropillar literature spans a huge range of morphologies. I have only investigated some design components in this work – a few sizes, shapes, speeds, loads, materials, and substrates. When can you stop? It is logical to approach this question from the standpoint of practicality. What micropillars are easy to make, and do they work as well as other micropillars with more "pristine" or complicated shapes? Thus, an additional area for micropillar research is manufacturing. It remains largely unknown what micropillar features are most essential to their contact properties, though this work suggests total contact area and ability to deform a soft substrate. Most micropillars are manufactured using photolithography techniques, but these are time and labor-intensive. Some work has been

done on roll-to-roll micropillar manufacturing (Yi et al. 2014) and laser microtexturing (T. Jiang et al. 2012; Z. Chen et al. 2017) but it is still unclear how these methods compare to each other.

Additional questions arise regarding simulations. Finite element models for friction between soft materials are poorly established; this work is one of the few times this system has ever been represented. Interaction models are compared in both Chapter 3 and Chapter 4, but are not different enough to elicit all experimental behavior. Our current understanding of soft sliding friction is incomplete. Interaction models must be improved, through better understanding of soft friction and better mathematical representations. Features to add to existing models potentially include viscoelasticity, strain stiffening, and other ways to describe stickiness.

Another interaction question is how to treat a fluid layer such as a lubricant. In this thesis, I consider the fluid layer to be thin due to feature and substrate deformation. This thin layer and low sliding speeds allow for assumption of laminar flow. Therefore, I have not included fluid flow in the interaction between texture and substrate.

But, other systems may have larger fluid layers, less viscous fluids, or faster speeds. The Stribeck Curve (Figure 31) describes friction between two surfaces. The Stribeck Number on the x-axis is a dimensionless number relating velocity, viscosity, and load. The y-axis is coefficient of friction. At slow speeds boundary lubrication occurs, and friction is dominated by asperity contact between the two surfaces. This is likely where friction behavior between lubricated textures and substrate lies for Chapters 3 and 4. At higher speeds, loads are supported by hydrodynamic pressure. Mixed lubrication, or a combination of boundary and hydrodynamic behavior occurs at medium speeds, creating a continuum. Xie et. al. lubricated PDMS micropillars with physiologic, mucus-containing fluids and determined that the

Stribeck curve is left-shifted for friction against class and that micropillars increase coefficient of friction (Xi et al. 2020).

Other micropillar morphologies, lubricant properties, or applications may approach the hydrodynamic regime of the Stribeck curve and in these cases, fluid flow may become important to consider. Joelle Frechette's group at Johns Hopkins has found that indentation of soft materials can trap fluid pockets between the soft indenter and rigid substrate. They suggest surface roughness and material elasticity contribute to slip, affecting trapping behavior (Yumo Wang and Frechette 2018). Fluid drainage can change from between micropillar channels to along feature surfaces as indentation into a rigid substrate increases (Gupta and Fréchette 2012). For the micropillars in Chapter 3 and the soft textures in Chapter 4, feature deformation is high so only a small amount of fluid remains between the two. For the stiffer features in Chapter 4, some fluid may remain between individual features, but the sliding speed is low, allowing assumption of laminar, thin flow.

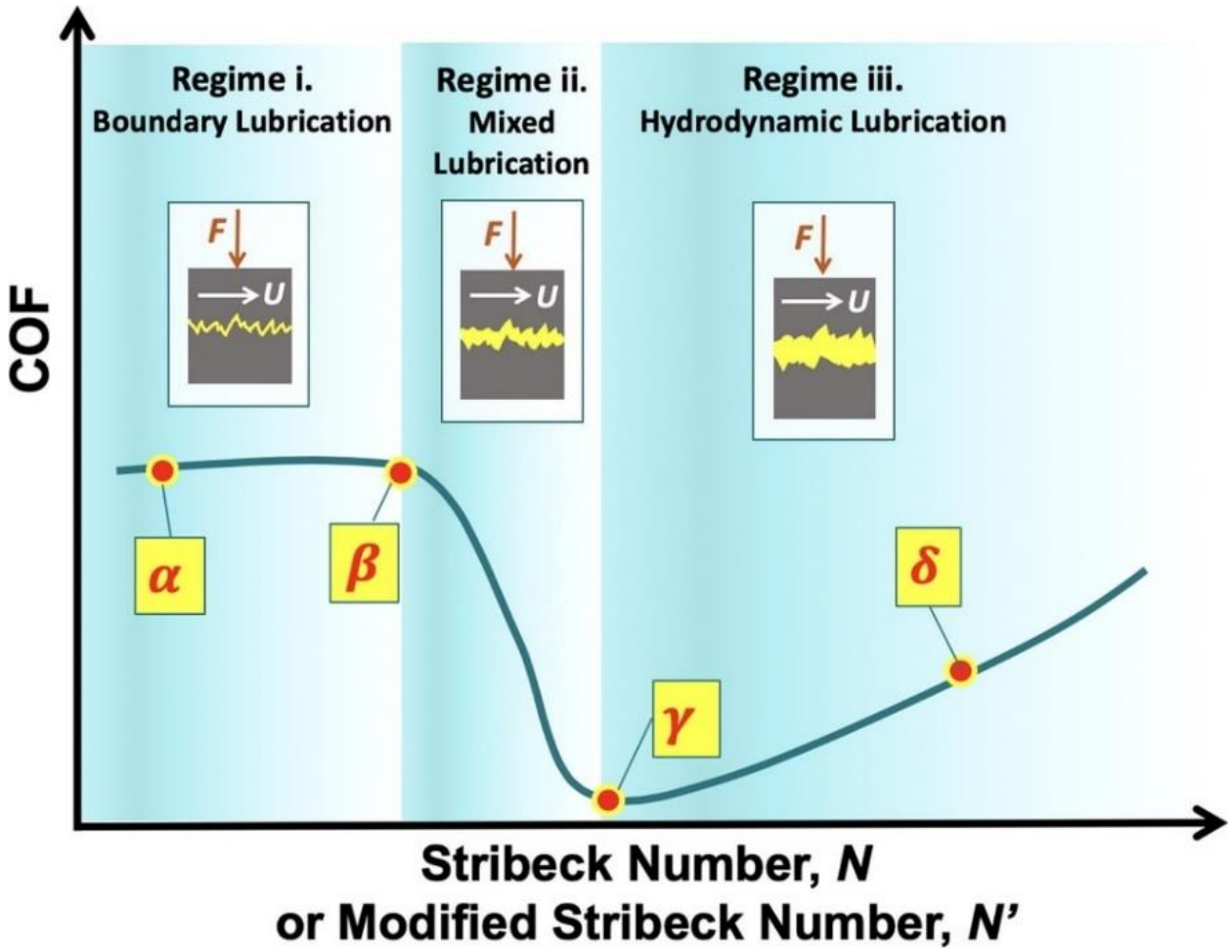

Figure 31: Stribeck curve for potential lubricated micropillar interaction with substrates (Xi et al. 2020)

Finally, applications for micropillars are just beginning to be realized. There are no nonexperimental medical devices that use micropillars. Yet, this field has great potential. Medical applications for micropillars generally fall into three areas: wearables, implantable devices, and devices used for procedures. Wearables include various tubes or patches that could benefit from enhanced or directional friction. Implantable devices include stents, ports, and implantable catheters. Procedural devices include balloons, capsule robots, catheters, and other endoscopic devices. Micropillars are already studied for their antibiofouling properties (Carve, Scardino, and Shimeta 2019), but further research is required on their biocompatibility.

Soft micropillar friction may also have value in food handling. Pick-and-place grippers with adhesion-enhancing textures have been demonstrated for rigid materials (Hensel, Moh, and Arzt 2018), but gripper for irregular and nonplanar soft or slippery shapes (Shintake et al. 2018) such as that shown in Figure 32 may require enhanced friction.

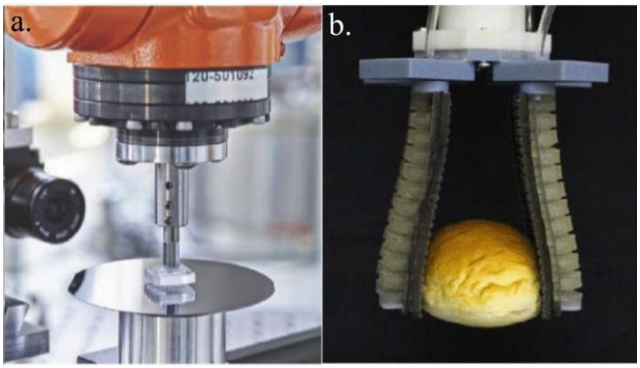

Figure 32: Micropillar gripper applications. (a) Micropillars are used for enhanced adhesion to rigid materials for some types of pick and place grippers. (b) Other gripper styles, such as soft robotic grippers that have potential in food handling (Zhongkui Wang, Torigoe, and Hirai 2017), may benefit more from increased friction to soft materials.

Overall, the field of micropillars for enhanced contact has recently seen significant expansion. However, friction of soft textures against soft substrates remains largely unknown. This area has great potential for new understanding and applications, especially in the medical field. As summarized by a review of the Contact Mechanics Challenge: “we have only touched the surface of the unknown” (Style et al. 2018).

REFERENCES

[1] al-Aown, Abdulrahman, Iason Kyriazis, Panagiotis Kallidonis, Pantelis Kraniotis, Christos Rigopoulos, Dimitrios Karnabatidis, Theodore Petsas, and Evangelos Liatsikos. 2010. "Ureteral Stents: New Ideas, New Designs." *Therapeutic Advances in Urology*. https://doi.org/10.1177/1756287210370699.

[2] Anderloni, Andrea, Gianluca Lollo, and Alessandro Repici. 2019. "Palliation of Malignant Dysphagia and Esophageal Fistulas." In *Clinical Gastrointestinal Endoscopy*. https://doi.org/10.1016/b978-0-323-41509-5.00028-1.

[3] Anderson, E. J., W. R. McGillis, and M. A. Grosenbaugh. 2001. "The Boundary Layer of Swimming Fish." *Journal of Experimental Biology* 204 (1).

[4] Ankhelyi, Madeleine V., Dylan K. Wainwright, and George V. Lauder. 2018. "Diversity of Dermal Denticle Structure in Sharks: Skin Surface Roughness and Three-Dimensional Morphology." *Journal of Morphology* 279 (8). https://doi.org/10.1002/jmor.20836.

[5] Arzt, Eduard, Stanislav Gorb, and Ralph Spolenak. 2003. "From Micro to Nano Contacts in Biological Attachment Devices." *Proceedings of the National Academy of Sciences of the United States of America* 100 (19). https://doi.org/10.1073/pnas.1534701100.

[6] Assenbergh, P. van, Frank Haring, Joshua A. Dijksman, and Dimitra Dodou. 2020. "Anisotropic Stiffness Adhesives for High Shear Forces on Soft Substrates." *Advanced Materials Interfaces* 7 (22). https://doi.org/10.1002/admi.202001173.

[7] Assenbergh, Peter van, Marike Fokker, Julian Langowski, Jan van Esch, Marleen Kamperman, and Dimitra Dodou. 2019. "Pull-off and Friction Forces of Micropatterned Elastomers on Soft Substrates: The Effects of Pattern Length Scale and Stiffness." *Beilstein Journal of Nanotechnology* 10 (1): 79–94. https://doi.org/10.3762/bjnano.10.8.

[8] Autumn, Kellar, and Nick Gravish. 2008. "Gecko Adhesion: Evolutionary Nanotechnology." *Philosophical Transactions of the Royal Society A: Mathematical, Physical and Engineering Sciences* 366 (1870). https://doi.org/10.1098/rsta.2007.2173.

[9] Autumn, Kellar, Yiching A. Liang, S. Tonia Hsieh, Wolfgang Zesch, Wal Pang Chan, Thomas W. Kenny, Ronald Fearing, and Robert J. Full. 2000. "Adhesive Force of a Single Gecko Foot-Hair." *Nature* 405 (6787). https://doi.org/10.1038/35015073.

[10] Autumn, Kellar, and Anne M. Peattie. 2002. "Mechanisms of Adhesion in Geckos." In *Integrative and Comparative Biology*. Vol. 42. https://doi.org/10.1093/icb/42.6.1081.

[11] Badler, David, and Haytam Kasem. 2020. "Synergetic Effect of the Simultaneous Use of Different Biomimetic Adhesive Micro-Structures on Tribological Performances." *Biotribology* 22 (June): 100124. https://doi.org/10.1016/j.biotri.2020.100124.

[12] Bae, Won Gyu, Doogon Kim, Moon Kyu Kwak, Laura Ha, Seong Min Kang, and Kahp Y.

Suh. 2013. “Enhanced Skin Adhesive Patch with Modulus-Tunable Composite Micropillars.” *Advanced Healthcare Materials*. https://doi.org/10.1002/adhm.201200098.

[13] Bae, Woong Jin, Jin Bong Choi, Kang Sup Kim, Su Jin Kim, Hyuk Jin Cho, U Syn Ha, Sung Hoo Hong, Ji Youl Lee, and Sae Woong Kim. 2015. “AB168. Evaluation of the Biocompatibility of Packing Materials for a Catheter.” *Translational Andrology and Urology* 4 (Suppl 1). https://doi.org/10.3978/j.issn.2223-4683.2015.s168.

[14] Bowen, Leah K., Karl Johannes, Emily Zuetell, Kristin N. Calahan, Steven A. Edmundowicz, Rong Long, and Mark E. Rentschler. 2020. “Patterned Enteroscopy Balloon Design Factors Influence Tissue Anchoring.” *Journal of the Mechanical Behavior of Biomedical Materials* 111. https://doi.org/10.1016/j.jmbbm.2020.103966.

[15] Brodoceanu, D., C. T. Bauer, E. Kroner, E. Arzt, and T. Kraus. 2016. “Hierarchical Bioinspired Adhesive Surfaces-A Review.” *Bioinspiration and Biomimetics*. https://doi.org/10.1088/1748-3190/11/5/051001.

[16] Calobrace, M. Bradley, Michael R. Schwartz, Kamakshi R. Zeidler, Troy A. Pittman, Robert Cohen, and W. Grant Stevens. 2018. “Long-Term Safety of Textured and Smooth Breast Implants.” *Aesthetic Surgery Journal*. https://doi.org/10.1093/asj/sjx157.

[17] Campo, Aránzazu Del, Christian Greiner, and Eduard Arzt. 2007. “Contact Shape Controls Adhesion of Bioinspired Fibrillar Surfaces.” *Langmuir*.

[18] Carbone, Giuseppe, and Elena Pierro. 2012. “Sticky Bio-Inspired Micropillars: Finding the Best Shape.” *Small*. https://doi.org/10.1002/smll.201102021.

[19] Carve, Megan, Andrew Scardino, and Jeff Shimeta. 2019. “Effects of Surface Texture and Interrelated Properties on Marine Biofouling: A Systematic Review.” *Biofouling* 35 (6): 597–617. https://doi.org/10.1080/08927014.2019.1636036.

[20] Chan, E. P., E. J. Smith, R. C. Hayward, and A. J. Crosby. 2008. “Surface Wrinkles for Smart Adhesion.” *Advanced Materials* 20 (4): 711–16. https://doi.org/10.1002/adma.200701530.

[21] Chen, Huawei, Liwen Zhang, Deyuan Zhang, Pengfei Zhang, and Zhiwu Han. 2015. “Bioinspired Surface for Surgical Graspers Based on the Strong Wet Friction of Tree Frog Toe Pads.” *ACS Applied Materials and Interfaces*. https://doi.org/10.1021/acsami.5b03039.

[22] Chen, Zhaozhao, Yujiao Zhang, Junying Li, Hom-lay Wang, and Haiyang Yu. 2017. “Influence of Laser-Microtextured Surface Collar on Marginal Bone Loss and Peri-Implant Soft Tissue Response: A Systematic Review and Meta-Analysis.” *Journal of Periodontology* 88 (7). https://doi.org/10.1902/jop.2017.160805.

[23] Cheung, Eugene, and Metin Sitti. 2008. “Adhesion of Biologically Inspired Oil-Coated Polymer Micropillars.” *Journal of Adhesion Science and Technology*. https://doi.org/10.1163/156856108X295545.

[24] Ciuti, Gastone, R. Caliò, D. Camboni, L. Neri, F. Bianchi, A. Arezzo, A. Koulaouzidis, et al. 2016. "Frontiers of Robotic Endoscopic Capsules: A Review." *Journal of Micro-Bio Robotics*. https://doi.org/10.1007/s12213-016-0087-x.

[25] Cotton, Peter B., Patrick Connor, Daniel McGee, Paul Jowell, Nick Nickl, Steve Schutz, Joseph Leung, John Lee, and Eric Libby. 2003. "Colonoscopy: Practice Variation among 69 Hospital-Based Endoscopists." *Gastrointestinal Endoscopy* 57 (3): 352–57. https://doi.org/10.1067/mge.2003.121.

[26] Drotlef, Dirk Michael, Lukas Stepien, Michael Kappl, W. Jon P. Barnes, Hans Jürgen Butt, and Aránzazu Del Campo. 2013. "Insights into the Adhesive Mechanisms of Tree Frogs Using Artificial Mimics." *Advanced Functional Materials* 23 (9): 1137–46. https://doi.org/10.1002/adfm.201202024.

[27] Federle, W., W. J.P. Barnes, W. Baumgartner, P. Drechsler, and J. M. Smith. 2006. "Wet but Not Slippery: Boundary Friction in Tree Frog Adhesive Toe Pads." *Journal of the Royal Society Interface* 3 (10). https://doi.org/10.1098/rsif.2006.0135.

[28] Formosa, Gregory, Micah J. Prendergast, Steven Edmundowicz, and Mark Rentschler. 2019. "Novel Optimization-Based Design and Surgical Evaluation of a Treaded Robotic Capsule Colonoscope." *IEEE TRANSACTIONS ON ROBOTICS*. https://doi.org/10.1109/TRO.2019.2949466.

[29] Freeman, Richard K., Amy Vyverberg, and Anthony J. Ascioti. 2011. "Esophageal Stent Placement for the Treatment of Acute Intrathoracic Anastomotic Leak after Esophagectomy." *Annals of Thoracic Surgery* 92 (1). https://doi.org/10.1016/j.athoracsur.2011.02.016.

[30] Gerson, Lauren B., Jason T. Flodin, and Kenichi Miyabayashi. 2008. "Balloon-Assisted Enteroscopy: Technology and Troubleshooting." *Gastrointestinal Endoscopy* 68 (6): 1158–67. https://doi.org/10.1016/j.gie.2008.08.012.

[31] Gerson, Lauren B., Jeffrey Tokar, Michael Chiorean, Simon Lo, G. Anton Decker, David Cave, Doumit BouHaidar, et al. 2009. "Complications Associated With Double Balloon Enteroscopy at Nine US Centers." *Clinical Gastroenterology and Hepatology* 7 (11). https://doi.org/10.1016/j.cgh.2009.07.005.

[32] Ghosh, Subir, and Sylvester Abanteriba. 2016. "Status of Surface Modification Techniques for Artificial Hip Implants." *Science and Technology of Advanced Materials*. https://doi.org/10.1080/14686996.2016.1240575.

[33] Ghosh, Subir, Dipankar Choudhury, Taposh Roy, Azuddin Bin Mamat, H. H. Masjuki, and Belinda Pingguan-Murphy. 2015. "Tribological Investigation of Diamond-like Carbon Coated Micro-Dimpled Surface under Bovine Serum and Osteoarthritis Oriented Synovial Fluid." *Science and Technology of Advanced Materials*. https://doi.org/10.1088/1468-6996/16/3/035002.

[34] Gillies, Andrew G., Amy Henry, Hauwen Lin, Angela Ren, Kevin Shiuan, Ronald S. Fearing, and Robert J. Full. 2014. "Gecko Toe and Lamellar Shear Adhesion on Macroscopic, Engineered Rough Surfaces." *Journal of Experimental Biology* 217 (2). https://doi.org/10.1242/jeb.092015.

[35] Glick, Paul, Srinivasan A. Suresh, Donald Ruffatto, Mark Cutkosky, Michael T. Tolley, and Aaron Parness. 2018. "A Soft Robotic Gripper with Gecko-Inspired Adhesive." *IEEE Robotics and Automation Letters* 3 (2): 903–10. https://doi.org/10.1109/LRA.2018.2792688.

[36] Gross, Seth A., and Mark E. Stark. 2008. "Initial Experience with Double-Balloon Enteroscopy at a U.S. Center." *Gastrointestinal Endoscopy* 67 (6): 890–97. https://doi.org/10.1016/j.gie.2007.07.047.

[37] Guo, Bingyong, Yang Liu, and Shyam Prasad. 2019. "Modelling of Capsule–Intestine Contact for a Self-Propelled Capsule Robot via Experimental and Numerical Investigation." *Nonlinear Dynamics* 98 (4). https://doi.org/10.1007/s11071-019-05061-y.

[38] Guo, Dong Jie, Rui Liu, Yu Cheng, Hao Zhang, Li Ming Zhou, Shao Ming Fang, Winston Howard Elliott, and Wei Tan. 2015. "Reverse Adhesion of a Gecko-Inspired Synthetic Adhesive Switched by an Ion-Exchange Polymer-Metal Composite Actuator." *ACS Applied Materials and Interfaces* 7 (9). https://doi.org/10.1021/am509163m.

[39] Gupta, Rohini, and Joëlle Fréchette. 2012. "Measurement and Scaling of Hydrodynamic Interactions in the Presence of Draining Channels." *Langmuir* 28 (41). https://doi.org/10.1021/la303508x.

[40] Gustafsson, Jenny K., Anna Ermund, Malin E.V. Johansson, André Schütte, Gunnar C. Hansson, and Henrik Sjövall. 2012. "An Ex Vivo Method for Studying Mucus Formation, Properties, and Thickness in Human Colonic Biopsies and Mouse Small and Large Intestinal Explants." *American Journal of Physiology - Gastrointestinal and Liver Physiology* 302 (4): 430–38. https://doi.org/10.1152/ajpgi.00405.2011.

[41] Hansen, W. R., and K. Autumn. 2005. "Evidence for Self-Cleaning in Gecko Setae." *Proceedings of the National Academy of Sciences of the United States of America* 102 (2). https://doi.org/10.1073/pnas.0408304102.

[42] Hawkes, Elliot W., Eric V. Eason, Alan T. Asbeck, and Mark R. Cutkosky. 2013. "The Gecko's Toe: Scaling Directional Adhesives for Climbing Applications." *IEEE/ASME Transactions on Mechatronics* 18 (2). https://doi.org/10.1109/TMECH.2012.2209672.

[43] He, Bo, Wei Chen, and Q. Jane Wang. 2008. "Surface Texture Effect on Friction of a Microtextured Poly(Dimethylsiloxane) (PDMS)." *Tribology Letters*. https://doi.org/10.1007/s11249-008-9351-0.

[44] Hensel, René, Karsten Moh, and Eduard Arzt. 2018. "Engineering Micropatterned Dry Adhesives: From Contact Theory to Handling Applications." *Advanced Functional Materials*. https://doi.org/10.1002/adfm.201800865.

[45] Huber, Gerrit, Stanislav N. Gorb, Naoe Hosoda, Ralph Spolenak, and Eduard Arzt. 2007. “Influence of Surface Roughness on Gecko Adhesion.” *Acta Biomaterialia* 3 (4). https://doi.org/10.1016/j.actbio.2007.01.007.

[46] Jeong, Hoon Eui, Moon Kyu Kwak, and Kahp Y. Suh. 2010. “Stretchable, Adhesion-Tunable Dry Adhesive by Surface Wrinkling.” *Langmuir* 26 (4): 2223–26. https://doi.org/10.1021/la904290g.

[47] Jiang, Tao, Jürgen Koch, Claudia Unger, Elena Fadeeva, Anastasia Koroleva, Qingliang Zhao, and Boris N. Chichkov. 2012. “Ultrashort Picosecond Laser Processing of Micro-Molds for Fabricating Plastic Parts with Superhydrophobic Surfaces.” *Applied Physics A: Materials Science and Processing* 108 (4). https://doi.org/10.1007/s00339-012-6985-4.

[48] Jiang, Weitao, Biao Lei, Hongzhong Liu, Dong Niu, Tingting Zhao, Bangdao Chen, Lei Yin, Yongsheng Shi, and Xiaokang Liu. 2017. “Fabrication of Directional Nanopillars with High-Aspect-Ratio Using a Stretching Imprint Process with a Microcavity Mold.” *Nanoscale* 9 (6). https://doi.org/10.1039/c6nr06957f.

[49] Jin, Kejia, Joseph C. Cremaldi, Jeffrey S. Erickson, Yu Tian, Jacob N. Israelachvili, and Noshir S. Pesika. 2014. “Biomimetic Bidirectional Switchable Adhesive Inspired by the Gecko.” *Advanced Functional Materials* 24 (5). https://doi.org/10.1002/adfm.201301960.

[50] Kamperman, Marleen, Elmar Kroner, Aránzazu Del Campo, Robert M. McMeeking, and Eduard Arzt. 2010. “Functional Adhesive Surfaces with ‘Gecko’ Effect: The Concept of Contact Splitting.” *Advanced Engineering Materials*. https://doi.org/10.1002/adem.201000104.

[51] Karagozler, Mustafa Emre, Eugene Cheung, Jiwoon Kwon, and Metin Sitti. 2006. “Miniature Endoscopie Capsule Robot Using Biomimetic Micro-Patterned Adhesives.” In *Proceedings of the First IEEE/RAS-EMBS International Conference on Biomedical Robotics and Biomechatronics, 2006, BioRob 2006*. https://doi.org/10.1109/BIOROB.2006.1639068.

[52] Kato, Masatoshi, Yasuyuki Tsuboi, Akihiko Kikuchi, and Taka Aki Asoh. 2016. “Hydrogel Adhesion with Wrinkle Formation by Spatial Control of Polymer Networks.” *Journal of Physical Chemistry B* 120 (22): 5042–46. https://doi.org/10.1021/acs.jpcb.6b01449.

[53] Kern, Madalyn D., Rong Long, and Mark E. Rentschler. 2018. “A Representative Volume Element Model for the Adhesion between a Micro-Pillared Surface and a Compliant Substrate.” *Mechanics of Materials* 119. https://doi.org/10.1016/j.mechmat.2018.01.004.

[54] Kern, Madalyn D., Joan Ortega Alcaide, and Mark E. Rentschler. 2014. “Soft Material Adhesion Characterization for in Vivo Locomotion of Robotic Capsule Endoscopes: Experimental and Modeling Results.” *Journal of the Mechanical Behavior of Biomedical Materials* 39: 257–69. https://doi.org/10.1016/j.jmbbm.2014.07.032.

[55] Kern, Madalyn D., Yuan Qi, Rong Long, and Mark E. Rentschler. 2017. "Characterizing Adhesion between a Micropatterned Surface and a Soft Synthetic Tissue." *Langmuir* 33 (4): 854–64. https://doi.org/10.1021/acs.langmuir.6b03643.

[56] Kesel, Antonia B., Andrew Martin, and Tobias Seidl. 2004. "Getting a Grip on Spider Attachment: An AFM Approach to Microstructure Adhesion in Arthropods." *Smart Materials and Structures* 13 (3). https://doi.org/10.1088/0964-1726/13/3/009.

[57] Kim, Tae Il, Hoon Eui Jeong, Kahp Y. Suh, and Hong H. Lee. 2009. "Stooped Nanohairs: Geometry-Controllable, Unidirectional, Reversible, and Robust Gecko-like Dry Adhesive." *Advanced Materials* 21 (22): 2276–81. https://doi.org/10.1002/adma.200803710.

[58] Kim, Yongkwan, Yunsie Chung, Angela Tsao, and Roya Maboudian. 2014. "Tuning Micropillar Tapering for Optimal Friction Performance of Thermoplastic Gecko-Inspired Adhesive." In *ACS Applied Materials and Interfaces*. https://doi.org/10.1021/am5007518.

[59] Korpela, Tarmo, Mika Suvanto, and Tuula T. Pakkanen. 2012. "Friction and Wear of Periodically Micro-Patterned Polypropylene in Dry Sliding." *Wear* 289. https://doi.org/10.1016/j.wear.2012.04.023.

[60] Krahn, J., Y. Liu, A. Sadeghi, and C. Menon. 2011. "A Tailless Timing Belt Climbing Platform Utilizing Dry Adhesives with Mushroom Caps." *Smart Materials and Structures* 20 (11). https://doi.org/10.1088/0964-1726/20/11/115021.

[61] Kundu, Santanu, Chelsea S. Davis, Thomas Long, Ravi Sharma, and Alfred J. Crosby. 2011. "Adhesion of Nonplanar Wrinkled Surfaces." *Journal of Polymer Science, Part B: Polymer Physics*. https://doi.org/10.1002/polb.22181.

[62] Kwak, Moon Kyu, Hoon Eui Jeong, Won Gyu Bae, Ho-Sup Jung, and Kahp Y. Suh. 2011. "Anisotropic Adhesion Properties of Triangular-Tip-Shaped Micropillars." *Small* 7 (16): 2296–2300. https://doi.org/10.1002/smll.201100455.

[63] Kwak, Moon Kyu, Hoon Eui Jeong, and Kahp Y. Suh. 2011. "Rational Design and Enhanced Biocompatibility of a Dry Adhesive Medical Skin Patch." *Advanced Materials* 23 (34). https://doi.org/10.1002/adma.201101694.

[64] Kwon, Jiwoon, Eugene Cheung, Sukho Park, and Metin Sitti. 2006. "Friction Enhancement via Micro-Patterned Wet Elastomer Adhesives on Small Intestinal Surfaces." *Biomedical Materials* 1 (4): 216–20. https://doi.org/10.1088/1748-6041/1/4/007.

[65] Lee, Jongho, Ronald S. Fearing, and Kyriakos Komvopoulos. 2008. "Directional Adhesion of Gecko-Inspired Angled Microfiber Arrays." *Applied Physics Letters* 93 (19). https://doi.org/10.1063/1.3006334.

[66] Lee, Jongho Hyun Jehong, Seungwan Seo, Jongho Hyun Jehong Lee, Kwang Seop Kim, Kwang Hee Ko, and Jongho Hyun Jehong Lee. 2014. "Anisotropic Adhesion of

Micropillars with Spatula Pads." *ACS Applied Materials and Interfaces* 6 (3): 1345–50. https://doi.org/10.1021/am4044135.

[67] Li, Yasong, Ausama Ahmed, Dan Sameoto, and Carlo Menon. 2012. "Abigaille II: Toward the Development of a Spider-Inspired Climbing Robot." *Robotica* 30 (1). https://doi.org/10.1017/S0263574711000373.

[68] Li, Yasong, Jeffrey Krahn, and Carlo Menon. 2016. "Bioinspired Dry Adhesive Materials and Their Application in Robotics: A Review." *Journal of Bionic Engineering*. Science Press. https://doi.org/10.1016/S1672-6529(16)60293-7.

[69] Liu, Quan, Di Tan, Fandong Meng, Baisong Yang, Zhekun Shi, Xin Wang, Qian Li, Chang Nie, Sheng Liu, and Longjian Xue. 2021. "Adhesion Enhancement of Micropillar Array by Combining the Adhesive Design from Gecko and Tree Frog." *Small* 17 (4): 2005493. https://doi.org/10.1002/smll.202005493.

[70] Lloyd, Charlie James, Jeffrey Peakall, Alan Burns, Gareth Keevil, Robert Dorrell, Paul Wignall, and Thomas Fletcher. 2021. "Hydrodynamic Efficiency in Sharks: The Combined Role of Riblets and Denticles." *Bioinspiration & Biomimetics*. https://doi.org/10.1088/1748-3190/abf3b1.

[71] Mahadevan, Vishy. 2014. "Anatomy of the Small Intestine." *Surgery (United Kingdom)* 32 (8): 391–95. https://doi.org/10.1016/j.mpsur.2014.06.003.

[72] Mahdavi, Alborz, Lino Ferreira, Cathryn Sundback, Jason W. Nichol, Edwin P. Chan, David J.D. Carter, Chris J. Bettinger, et al. 2008. "A Biodegradable and Biocompatible Gecko-Inspired Tissue Adhesive." *Proceedings of the National Academy of Sciences of the United States of America* 105 (7). https://doi.org/10.1073/pnas.0712117105.

[73] Majidi, C., R. E. Groff, Y. Maeno, B. Schubert, S. Baek, B. Bush, R. Maboudian, et al. 2006. "High Friction from a Stiff Polymer Using Microfiber Arrays." *Physical Review Letters*. https://doi.org/10.1103/PhysRevLett.97.076103.

[74] Majumder, Abhijit, Ashutosh Sharma, and Animangsu Ghatak. 2010. "Bio-Inspired Adhesion and Adhesives: Controlling Adhesion by Micro-Nano Structuring of Soft Surfaces." In *Microfluidics and Microfabrication*. https://doi.org/10.1007/978-1-4419-1543-6_7.

[75] Manning, D. P., J. E. Cooper, I. Stirling, C. M. Jones, M. Bruce, and P. C. McCausland. 1985. "Studies on the Footpads of the Polar Bear (Ursus Maritimus) and Their Possible Relevance to Accident Prevention." *Journal of Hand Surgery*. https://doi.org/10.1016/S0266-7681(85)80049-8.

[76] Manno, Mauro, Carmelo Barbera, Helga Bertani, Raffaele Manta, Vincenzo Giorgio Mirante, Emanuele Dabizzi, Angelo Caruso, Flavia Pigo, Giampiero Olivetti, and Rita Conigliaro. 2012. "Single Balloon Enteroscopy: Technical Aspects and Clinical Applications." *World Journal of Gastrointestinal Endoscopy* 4 (2): 28. https://doi.org/10.4253/wjge.v4.i2.28.

[77] Manoonpong, Poramate, Dennis Petersen, Alexander Kovalev, Florentin Wörgötter, Stanislav N. Gorb, Marlene Spinner, and Lars Heepe. 2016. "Enhanced Locomotion Efficiency of a Bio-Inspired Walking Robot Using Contact Surfaces with Frictional Anisotropy." *Scientific Reports* 6. https://doi.org/10.1038/srep39455.

[78] Martinez, Ramses V., Jamie L. Branch, Carina R. Fish, Lihua Jin, Robert F. Shepherd, Rui M. D. Nunes, Zhigang Suo, and George M. Whitesides. 2013. "Robotic Tentacles with Three-Dimensional Mobility Based on Flexible Elastomers." *Advanced Materials* 25 (2): 205–12. https://doi.org/10.1002/adma.201203002.

[79] McGhee, Eric O., Samuel M. Hart, Juan Manuel Urueña, and W. Gregory Sawyer. 2019. "Hydration Control of Gel-Adhesion and Muco-Adhesion." *Langmuir* 35 (48): 15769–75. https://doi.org/10.1021/acs.langmuir.9b02816.

[80] Mehdizadeh, Shahab, Andrew Ross, Lauren Gerson, Jonathan Leighton, Ann Chen, Drew Schembre, Gary Chen, et al. 2006. "What Is the Learning Curve Associated with Double-Balloon Enteroscopy? Technical Details and Early Experience in 6 U.S. Tertiary Care Centers." *Gastrointestinal Endoscopy* 64 (5): 740–50. https://doi.org/10.1016/j.gie.2006.05.022.

[81] Moon, Myoung Woon, Tae Gon Cha, Kwang Ryeol Lee, Ashkan Vaziri, and Ho Young Kim. 2010. "Tilted Janus Polymer Pillars." *Soft Matter* 6 (16). https://doi.org/10.1039/c0sm00126k.

[82] Murphy, Michael P., Burak Aksak, and Metin Sitti. 2009. "Gecko-Inspired Directional and Controllable Adhesion." *Small* 5 (2). https://doi.org/10.1002/smll.200801161.

[83] Murphy, Michael P., Seok Kim, and Metin Sitti. 2009. "Enhanced Adhesion by Gecko-Inspired Hierarchical Fibrillar Adhesives." *ACS Applied Materials and Interfaces* 1 (4). https://doi.org/10.1021/am8002439.

[84] Muthukumar, M., and M. S. Bobji. 2018. "Effect of Micropillar Surface Texturing on Friction under Elastic Dry Reciprocating Contact." *Meccanica* 53 (9). https://doi.org/10.1007/s11012-017-0816-9.

[85] Northen, Michael T., Christian Greiner, Eduard Arzt, and Kimberly L. Turner. 2008. "A Gecko-Inspired Reversible Adhesive." *Advanced Materials* 20 (20). https://doi.org/10.1002/adma.200801340.

[86] Ohzono, Takuya, and Kay Teraoka. 2017. "Unique Load Dependency of Static Friction of Wrinkles Formed on Textile-Embedded Elastomer Surfaces." *AIP Advances*. https://doi.org/10.1063/1.4983800.

[87] Pennazio, Marco, Cristiano Spada, Rami Eliakim, Martin Keuchel, Andrea May, Chris J. Mulder, Emanuele Rondonotti, et al. 2015. "Small-Bowel Capsule Endoscopy and Device-Assisted Enteroscopy for Diagnosis and Treatment of Small-Bowel Disorders: European Society of Gastrointestinal Endoscopy (ESGE) Clinical Guideline." *Endoscopy*.

https://doi.org/10.1055/s-0034-1391855.

[88] Pitenis, Angela A, Juan Manuel Urueña, Eric O McGhee, Samuel M Hart, Erik R Reale, Jiho Kim, Kyle D Schulze, et al. 2017. "Challenges and Opportunities in Soft Tribology." *Tribology-Materials, Surfaces & Interfaces* 11 (4): 180–86. https://doi.org/10.1080/17515831.2017.1400779.

[89] Randquist, Charles, and Örjan Gribbe. 2010. "Highly Cohesive Textured Form Stable Gel Implants." In *Aesthetic and Reconstructive Surgery of the Breast*. https://doi.org/10.1016/B978-0-7020-3180-9.00025-1.

[90] Raut, Hemant Kumar, Avinash Baji, Hassan Hussein Hariri, Hashina Parveen, Gim Song Soh, Hong Yee Low, and Kristin L. Wood. 2018. "Gecko-Inspired Dry Adhesive Based on Micro-Nanoscale Hierarchical Arrays for Application in Climbing Devices." *ACS Applied Materials and Interfaces* 10 (1). https://doi.org/10.1021/acsami.7b09526.

[91] Resch, Timothy, Krassi Ivancev, Jan Brunkwall, Ulf Nyman, Martin Malina, and Bengt Lindblad. 1999. "Distal Migration of Stent-Grafts after Endovascular Repair of Abdominal Aortic Aneurysms." *Journal of Vascular and Interventional Radiology* 10 (3). https://doi.org/10.1016/S1051-0443(99)70027-8.

[92] Roscoe, D T, and G Walker. 1991. "The Adhesion of Spiders to Smooth Surfaces." *Bull.Br.Arachnol.Soc*. Vol. 8.

[93] Roy, Taposh, Dipankar Choudhury, Subir Ghosh, Azuddin Bin Mamat, and Belinda Pingguan-Murphy. 2015. "Improved Friction and Wear Performance of Micro Dimpled Ceramic-on-Ceramic Interface for Hip Joint Arthroplasty." *Ceramics International*. https://doi.org/10.1016/j.ceramint.2014.08.123.

[94] Schubert, B., C. Majidi, R. E. Groff, S. Baek, B. Bush, R. Maboudian, and R. S. Fearing. 2007. "Towards Friction and Adhesion from High Modulus Microfiber Arrays." *Journal of Adhesion Science and Technology* 21 (12–13): 1297–1315. https://doi.org/10.1163/156856107782328344.

[95] Shintake, Jun, Vito Cacucciolo, Dario Floreano, and Herbert Shea. 2018. "Soft Robotic Grippers." *Advanced Materials* 30 (29): 1707035.

[96] Skondras-Giousios, D, N E Karkalos, and A P Markopoulos. 2020. " Finite Element Simulation of Friction and Adhesion Attributed Contact of Bio-Inspired Gecko-Mimetic PDMS Micro-Flaps with SiO 2 Spherical Surface ." *Bioinspiration & Biomimetics* 15 (6). https://doi.org/10.1088/1748-3190/ab983e.

[97] Sliker, Levin J., Gastone Ciuti, Mark E. Rentschler, and Arianna Menciassi. 2016. "Frictional Resistance Model for Tissue-Capsule Endoscope Sliding Contact in the Gastrointestinal Tract." *Tribology International*. https://doi.org/10.1016/j.triboint.2016.06.003.

[98] Sliker, Levin J., Madalyn D. Kern, and Mark E. Rentschler. 2013. "Preliminary

Experimental Results and Modeling for a Four Degree of Freedom Automated Traction Measurement Platform for Quantitative Evaluation of in Vivo Robotic Capsule Colonoscopy Mobility Effectiveness." In *Proceedings - IEEE International Conference on Robotics and Automation*. https://doi.org/10.1109/ICRA.2013.6631273.

[99] Sliker, Levin J., Madalyn D. Kern, Jonathan A. Schoen, and Mark E. Rentschler. 2012. "Surgical Evaluation of a Novel Tethered Robotic Capsule Endoscope Using Micro-Patterned Treads." *Surgical Endoscopy and Other Interventional Techniques* 26 (10): 2862–69. https://doi.org/10.1007/s00464-012-2271-y.

[100] Smooth-On. 2013. "Material Safety Data Sheet: Ecoflex Series." https://www.smooth-on.com/msds/files/Ecoflex_Series.pdf.

[101] Stark, Alyssa Y., Mena R. Klittich, Metin Sitti, Peter H. Niewiarowski, and Ali Dhinojwala. 2016. "The Effect of Temperature and Humidity on Adhesion of a Gecko-Inspired Adhesive: Implications for the Natural System." *Scientific Reports* 6. https://doi.org/10.1038/srep30936.

[102] Style, Robert W., Brandon A. Krick, Katharine E. Jensen, and Gregory W. Sawyer. 2018. "The Contact Mechanics Challenge: Tribology Meets Soft Matter." *Soft Matter* 14 (28). https://doi.org/10.1039/c8sm00823j.

[103] Suresh, Srinivasan A., David L. Christensen, Elliot W. Hawkes, and Mark Cutkosky. 2015. "Surface and Shape Deposition Manufacturing for the Fabrication of a Curved Surface Gripper." *Journal of Mechanisms and Robotics* 7 (2): 1–7. https://doi.org/10.1115/1.4029492.

[104] Suzuki, K., and T. Ohzono. 2016. "Wrinkles on a Textile-Embedded Elastomer Surface with Highly Variable Friction." *Soft Matter*. https://doi.org/10.1039/c6sm00728g.

[105] Takahashi, Kunio, Jose Oriol Lopez Berengueres, Kenichi J. Obata, and Shigeki Saito. 2006. "Geckos' Foot Hair Structure and Their Ability to Hang from Rough Surfaces and Move Quickly." *International Journal of Adhesion and Adhesives* 26 (8). https://doi.org/10.1016/j.ijadhadh.2005.12.002.

[106] Tamelier, John, Sathya Chary, and Kimberly L. Turner. 2012. "Vertical Anisotropic Microfibers for a Gecko-Inspired Adhesive." *Langmuir* 28 (23). https://doi.org/10.1021/la3004855.

[107] Tan, Di, Xin Wang, Quan Liu, Kui Shi, Baisong Yang, Sheng Liu, Zhong-Shuai Wu, and Longjian Xue. 2019. "Switchable Adhesion of Micropillar Adhesive on Rough Surfaces." *Small* 15 (50): 1904248. https://doi.org/10.1002/smll.201904248.

[108] Teshima, Christopher W., and Gary May. 2012. "Small Bowel Enteroscopy." *Canadian Journal of Gastroenterology*.

[109] Thanh-Vinh, N., H. Takahashi, T. Kan, K. Noda, K. Matsumoto, and I. Shimoyama. 2011. "Micro Suction Cup Array for Wet/Dry Adhesion." In *Proceedings of the IEEE*

International Conference on Micro Electro Mechanical Systems (MEMS), 284–87. https://doi.org/10.1109/MEMSYS.2011.5734417.

[110] Tian, Hongmiao, Xiangming Li, Jinyou Shao, Chao Wang, Yan Wang, Yazhou Tian, and Haoran Liu. 2019. "Gecko-Effect Inspired Soft Gripper with High and Switchable Adhesion for Rough Surfaces." *Advanced Materials Interfaces* 6 (18): 1900875. https://doi.org/10.1002/admi.201900875.

[111] Tian, Ye, Zizhou Zhao, Gina Zaghi, Yongkwan Kim, Dongxing Zhang, and Roya Maboudian. 2015. "Tuning the Friction Characteristics of Gecko-Inspired Polydimethylsiloxane Micropillar Arrays by Embedding Fe3O4 and SiO2 Particles." *ACS Applied Materials & Interfaces* 7 (24): 13232–37. https://doi.org/10.1021/acsami.5b03301.

[112] Tricinci, Omar, Tercio Terencio, Barbara Mazzolai, Nicola M. Pugno, Francesco Greco, and Virgilio Mattoli. 2015. "3D Micropatterned Surface Inspired by Salvinia Molesta via Direct Laser Lithography." *ACS Applied Materials and Interfaces* 7 (46). https://doi.org/10.1021/acsami.5b07722.

[113] Tsai, Chen Yi, and Cheng Chung Chang. 2013. "Auto-Adhesive Transdermal Drug Delivery Patches Using Beetle Inspired Micropillar Structures." *Journal of Materials Chemistry B*. https://doi.org/10.1039/c3tb20735h.

[114] Varum, Felipe J.O., Francisco Veiga, João S. Sousa, and Abdul W. Basit. 2010. "An Investigation into the Role of Mucus Thickness on Mucoadhesion in the Gastrointestinal Tract of Pig." *European Journal of Pharmaceutical Sciences* 40 (4): 335–41. https://doi.org/10.1016/j.ejps.2010.04.007.

[115] Varum, Felipe J.O., Francisco Veiga, João S. Sousa, and Abdul W. Basit.Basit, Abdul W. 2012. "Mucus Thickness in the Gastrointestinal Tract of Laboratory Animals." *Journal of Pharmacy and Pharmacology*. https://doi.org/10.1111/j.2042-7158.2011.01399.x.

[116] Wang, Liu, Shutao Qiao, and Nanshu Lu. 2017. "Effects of Surface Tension on the Suction Forces Generated by Miniature Craters." *Extreme Mechanics Letters*.

[117] Wang, Yue, Hongmiao Tian, Jinyou Shao, Dan Sameoto, Xiangming Li, Li Wang, Hong Hu, Yucheng Ding, and Bingheng Lu. 2016. "Switchable Dry Adhesion with Step-like Micropillars and Controllable Interfacial Contact." *ACS Applied Materials and Interfaces*. https://doi.org/10.1021/acsami.6b01434.

[118] Wang, Yumo, and Joelle Frechette. 2018. "Morphology of Soft and Rough Contact: Via Fluid Drainage." *Soft Matter*.

[119] Wang, Zhengzhi. 2018. "Slanted Functional Gradient Micropillars for Optimal Bioinspired Dry Adhesion." *ACS Nano*. https://doi.org/10.1021/acsnano.7b07493.

[120] Wang, Zhongkui, Yuuki Torigoe, and Shinichi Hirai. 2017. "A Prestressed Soft Gripper: Design, Modeling, Fabrication, and Tests for Food Handling." *IEEE Robotics and*

Automation Letters 2 (4). https://doi.org/10.1109/LRA.2017.2714141.

[121] Wei, Lihua, Kristen E. Reiter, Thomas McElrath, Marianne Alleyne, and Alison C. Dunn. 2019. "Diffraction Gratings Alter the Surface Friction of Iridescent Beetle Cuticle against Fibrous Surfaces." *Biotribology* 20 (December): 100108. https://doi.org/10.1016/j.biotri.2019.100108.

[122] Xi, Yiwen, Hans J. Kaper, Chang Hwan Choi, and Prashant K. Sharma. 2020. "Tribological Properties of Microporous Polydimethylsiloxane (PDMS) Surfaces under Physiological Conditions." *Journal of Colloid and Interface Science* 561 (March): 220–30. https://doi.org/10.1016/j.jcis.2019.11.082.

[123] Xue, Longjian, Jagoba Iturri, Michael Kappl, Hans Jürgen Butt, and Aránzazu Del Campo. 2014. "Bioinspired Orientation-Dependent Friction." *Langmuir*. https://doi.org/10.1021/la502695d.

[124] Yamamoto, Hironori, Christian Ell, Hirito Kita, and Andrea May. 2014. "Double-Balloon Endoscopy." In *Video Capsule Endoscopy*, 113–18. Berlin, Heidelberg: Springer Berlin Heidelberg. https://doi.org/10.1007/978-3-662-44062-9_13.

[125] Yamamoto, Hironori, Hiroto Kita, Keijiro Sunada, Yoshikazu Hayashi, Hiroyuki Sato, Tomonori Yano, Michiko Iwamoto, et al. 2004. "Clinical Outcomes of Double-Balloon Endoscopy for the Diagnosis and Treatment of Small-Intestinal Diseases." *Clinical Gastroenterology and Hepatology*. https://doi.org/10.1016/s1542-3565(04)00453-7.

[126] Yi, Hoon, Insol Hwang, Jeong Hyeon Lee, Dael Lee, Haneol Lim, Dongha Tahk, Minho Sung, et al. 2014. "Continuous and Scalable Fabrication of Bioinspired Dry Adhesives via a Roll-to-Roll Process with Modulated Ultraviolet-Curable Resin." *ACS Applied Materials & Interfaces* 6 (16): 14590–99. https://doi.org/10.1021/am503901f.

[127] Zarins, Christopher K., Frank R. Arko, Tami Crabtree, Daniel A. Bloch, Kenneth Ouriel, Robert C. Allen, and Rodney A. White. 2004. "Explant Analysis of AneuRx Stent Grafts: Relationship between Structural Findings and Clinical Outcome." *Journal of Vascular Surgery* 40 (1). https://doi.org/10.1016/j.jvs.2004.03.008.

[128] Zhang, Hongyu, Yi Wang, Steven Vasilescu, Zhibin Gu, and Tao Sun. 2017. "Bio-Inspired Enhancement of Friction and Adhesion at the Polydimethylsiloxane-Intestine Interface and Biocompatibility Characterization." *Materials Science and Engineering C*. https://doi.org/10.1016/j.msec.2016.12.013.

[129] Zhang, Hongyu, Ying Yan, Zhibin Gu, Yi Wang, and Tao Sun. 2016. "Friction Enhancement between Microscopically Patterned Polydimethylsiloxane and Rabbit Small Intestinal Tract Based on Different Lubrication Mechanisms." *ACS Biomaterials Science & Engineering* 2 (6): 900–907. https://doi.org/10.1021/acsbiomaterials.5b00558.